Doctoral Thesis

A Study on Pre-Transition Corrosion Behavior of Zirconium Alloy in Simulated Primary Water Conditions of Nuclear Power Plant

Taeho Kim

Department of Nuclear Engineering

Graduate School of UNIST

2018

A Study on Pre-Transition Corrosion Behavior of Zirconium Alloy in Simulated Primary Water Conditions of Nuclear Power Plant

Taeho Kim

Department of Nuclear Engineering

Graduate School of UNIST

A Study on Pre-Transition Corrosion Behavior of Zirconium Alloy in Simulated Primary Water Conditions of Nuclear Power Plant

A thesis
submitted to the Graduate School of UNIST
in partial fulfillment of the
requirements for the degree of
Doctor of Philosophy

Taeho Kim

07. 07. 2018
Approved by

Advisor
Prof. Ji Hyun Kim

A Study on Pre-Transition Corrosion Behavior of Zirconium Alloy in Simulated Primary Water Conditions of Nuclear Power Plant

Taeho Kim

This certifies that the thesis of Taeho Kim is approved.

07. 07. 2018

Advisor: Ji Hyun Kim

Hyun-Gil Kim

Chi Bum Bahn

In Cheol Bang

Soon Yong Kwon

ABSTRACT

As fuel cladding materials of nuclear power plant, especially pressurized water reactors, Zr alloys have been used, because they have good mechanical properties, and low cross section for thermal neutron capture. Previous studies investigating about the corrosion behavior of zirconium alloy entail ex-situ experiments, however ex-situ methods could influence on the structure and phase stability of oxide film on zirconium alloy. Also, the current management band of DH content is near 2.5 mg/kg, and some discussions arise on the possibility to have it either lower or higher than currently, for mitigating the corrosion of structural materials of nuclear power plant. However, there is not enough data about the dissolved hydrogen (DH) effect on the oxidation and corrosion characteristic of Zr alloy at primary coolant water condition.

Therefore, in this thesis, in-situ investigation has been conducted for analyzing the corrosion characteristic of Zr alloy in simulated primary coolant water condition for pressurized water reactors. To observe the influence of the water chemistry on the corrosion characteristic of Zr alloy for 100 d, Raman spectroscopy is adopted. In-situ Raman spectroscopy and electrochemical impedance spectroscopy methods have been applied to characterize the phase transformation of zirconium oxide in simulated primary water conditions of pressurized water reactors, and the detail is like follows: 20 MPa pressure, 360 ^{o}C temperature by heaters and high-pressure pump, a dissolved oxygen (DO) concentration is lower than 5 ppb, and concentrations of lithium hydroxide (LiOH) and boric acid (H_3BO_3) are 2 and 1200 ppm, respectively.

The DH concentrations were set as 2.49 and 4.15 mg/kg at standard pressure and temperature for simulating the normal and high DH level. In-situ Raman spectra were collected for zirconium oxide and it represents the phase of zirconium oxide could be different due to the DH concentration. The DH concentration influences on the phase stability of zirconium oxide, and transmission electron microscopy results reveal that at the high DH level, the oxide growth rate is faster than the normal DH concentration due to the strengthened the tetragonal phase to monoclinic phase transformation of zirconium oxide Furthermore, zirconium oxide resistivity is measured, and the resistivity value is relatively low when the oxide is formed at high DH concentration.

To investigate the oxygen chemistry of the O/M interface of zirconium alloy after high temperature water corrosion with different DH levels, the scanning transmission X-ray microscopy and X-ray adsorption spectroscopy techniques were adopted. The oxygen chemistry of zirconium oxide at O/M interface was compared to that of the bulk oxide layer, and O K-edge X-ray adsorption spectra represent the sub-oxide structures are shown in the O/M interface.

Finally, for the fundamental study for the hydration process of zirconium oxide at high temperature water, high resolution X-ray reflectivity measurement experiment is adopted. The single crystal of YSZ (111) was prepared to characterize the atomistic structure of interface between yttria-stabilized zirconium oxide (YSZ) and water layer using X-ray reflectivity. With high resolution X-ray reflectivity, the hydration structures of YSZ (111) and water interface were measured as sub-Ångström resolution, at room temperature, and high temperature and pressure condition (340 ℃, 20 MPa). At high temperature water condition, the hydrophobic structure becomes strong, due to the increase of diffusion rate as well as decrease of oxygen vacancy at the YSZ (111) surface layer.

Several pressurized water reactors have been started to manage the water chemistry for mitigating the corrosion of structure material, especially Ni-based alloy and austenite stainless steel. However, the management of zirconium fuel cladding corrosion is also key issue to guarantee the safety of nuclear power plants. Therefore, the optimized DH concentration should be set after considering the corrosion issues not only structural materials but also zirconium fuel cladding materials. Hence, this Ph.D research investigated the fundamental mechanism of zirconium alloy corrosion from a microstructure point of view, the relationship between DH concentration and corrosion characteristic of zirconium alloy, and finally propose the optimal DH concentration for primary coolant water chemistry.

Table of Contents

List of Figures

List of Tables

1. Introduction

1.1. Background

As fuel cladding materials of nuclear power plant, especially pressurized water reactors, Zr alloys have been used, because they have good mechanical properties, and low cross section for thermal neutron capture. However, the importance of understanding of the zirconium alloys corrosion mechanism has been a key issue after the Fukushima accident, as they act as the primary shield from the radioactive materials. Figure 1-1 shows a schematic illustration of pressurized water reactors and the nuclear fuel assembly [1]. Also, the degradation behavior of the zirconium cladding affects the accidents of the nuclear reactors. Moreover, zirconium oxide is formed from the metal/water interface, and phase and structure of zirconium oxide influences on its mechanical and chemical properties [2–4]. Accordingly, the corrosion behavior and mechanism of zirconium alloy should be understood to assure the safety of the nuclear power plants.

The understanding of the transformation mechanism of zirconium oxide from tetragonal phase to monoclinic phase which is enhanced by the water becomes an unsolved issue [5]. Literature results presented the OH^- ions are formed by the water ionization, and they fill the vacancy sites of zirconium oxide by diffusing into lattice of zirconium oxide, lowering the concentration of oxygen vacancy and destabilizing the tetragonal phase zirconium oxide [6–8]. The phase transformation mechanism of zirconium oxide in high temperature water is the following; Water is chemically absorbed on the zirconium oxide surface and, by reacting with oxygen (O^{2-}) ions, forms OH^- ions on the oxide surface. Then, the OH^- ions penetrate the inner part by grain boundary diffusion and fill the oxygen vacancies within the grains. Finally, the tetragonal phase to monoclinic phase transformation occurs because the number of oxygen vacancy is reduced.

Currently, the dissolved hydrogen (DH) concentration is an issue in water chemistry, especially, in primary water chemistry of pressurized water reactors, as the change in the DH concentration can affect the corrosion mechanism of the nickel base alloy [9–12]. The effect of the DH concentration on the oxide formation has been investigated by previous studies [13,14]; however, there are few literatures investigating the effects of the DH level on zirconium oxide and oxide phase transformation in a primary water condition of pressurized water reactor.

Also, the water-metal interface is regarded as the rate-controlling site governing the rapid oxidation transition in high-burn-up fuels. During the corrosion, a tetragonal oxide layer formed on

the Zr alloy because of the stress accumulated in the O/M interface. This layer becomes unstable monoclinic oxide phase as the layer thickness increases, thus decreasing the stress [15–17]. Therefore, it is important to determine the types of oxides (i.e., the phases of the oxides) in the oxide layer formed on the zirconium alloy during the in-situ oxidation process. Because it does not require the removal of sample from the oxidation environment, which can influence on the structure and oxide phase of specimen.

Therefore, in this thesis, Raman spectroscopy and X-ray reflectivity (XRR) measurement methods were adopted for in-situ zirconium oxide analysis, which can be used at high pressure and high temperature water environment. From In-situ Raman spectroscopy, it is possible to characterize the oxide phase and oxide film on a metal surface, providing the oxidation mechanisms. From the X-ray reflectivity measurement results, the interfacial structure at oxide/water interface and the early stage corrosion behavior of zirconium alloy can be revealed. Subsequently, ex-situ investigation methods such as scanning transmission X-ray microscopy (STXM), transmission electron microscopy (TEM) were employed to further characterize the oxygen chemistry and the zirconium oxide structure after high temperature water corrosion.

1.2. Goal and approach

The main goal of this thesis is to understand the effect of DH on the corrosion behavior on zirconium alloy at high temperature water from Raman spectroscopy and X-ray synchrotron experimental observations. In-situ Raman spectroscopy has been applied to investigate the phase transformation of zirconium oxide in simulated primary water environments of pressurized water reactors (PWRs) with different DH concentrations. For supporting the phase distribution of zirconium oxide, TEM analysis was also conducted after high temperature water corrosion. The STXM and X-ray absorption spectroscopy were adopted for characterizing the oxygen chemistry of zirconium oxide at O/M interface. To investigate the atomistic structure of zirconium oxide and high temperature water interface, high resolution X-ray reflectivity technique using synchrotron X-ray source was also adopted. Figure 1-2 and 1-3 show a diagram which illustrates the goal and approaches to investigate the corrosion behavior of zirconium alloy at simulated primary coolant loop environment.

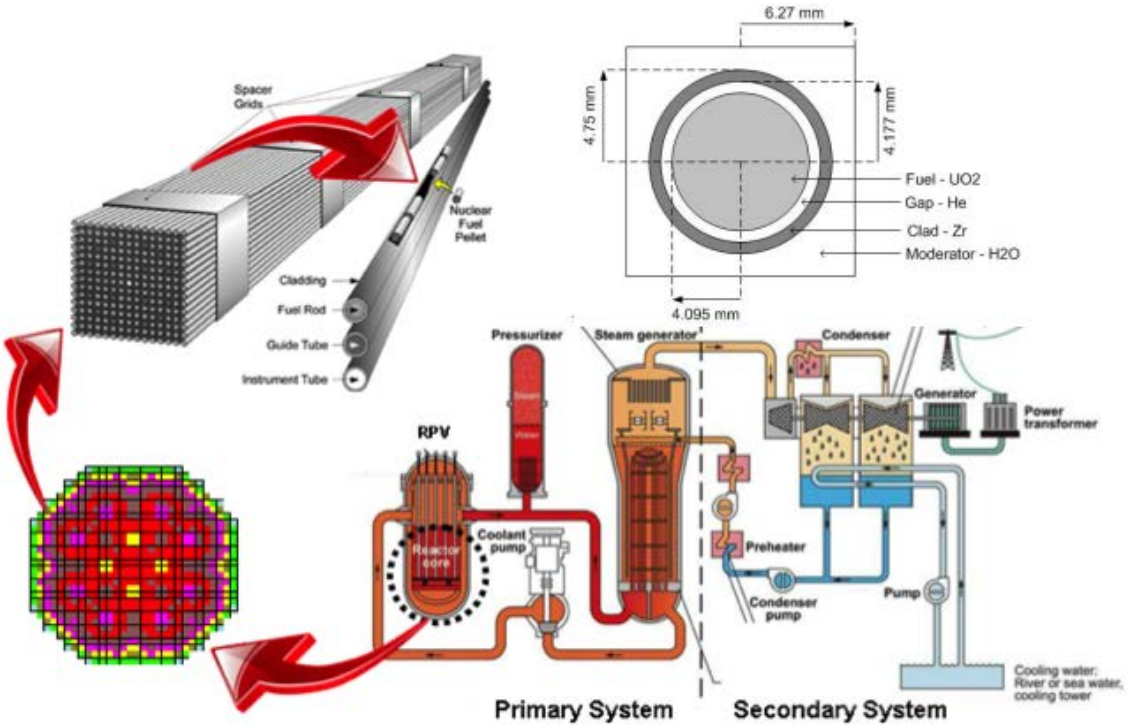

Figure 1-1 Schematic illustration of pressurized water reactors and nuclear fuel assembly [1]

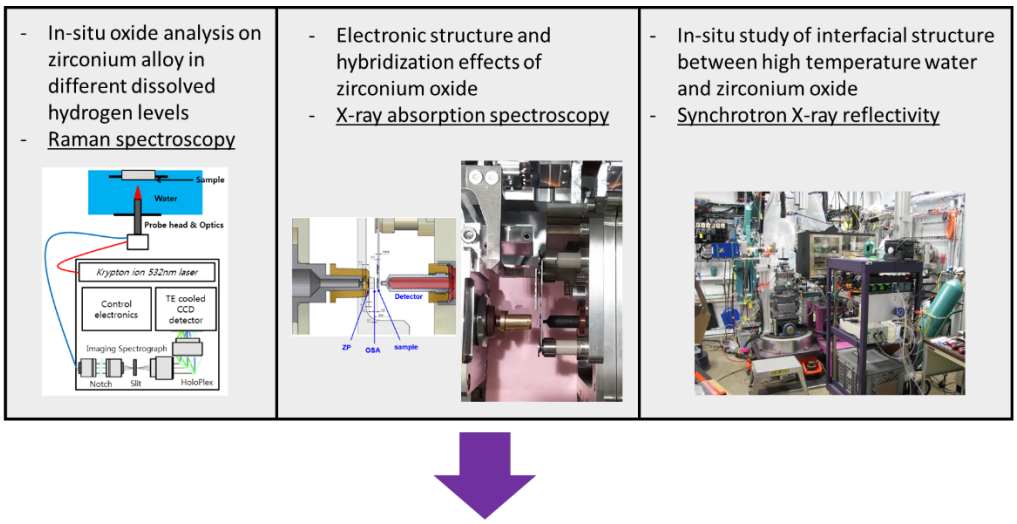

Figure 1-2 A diagram of goal of this thesis

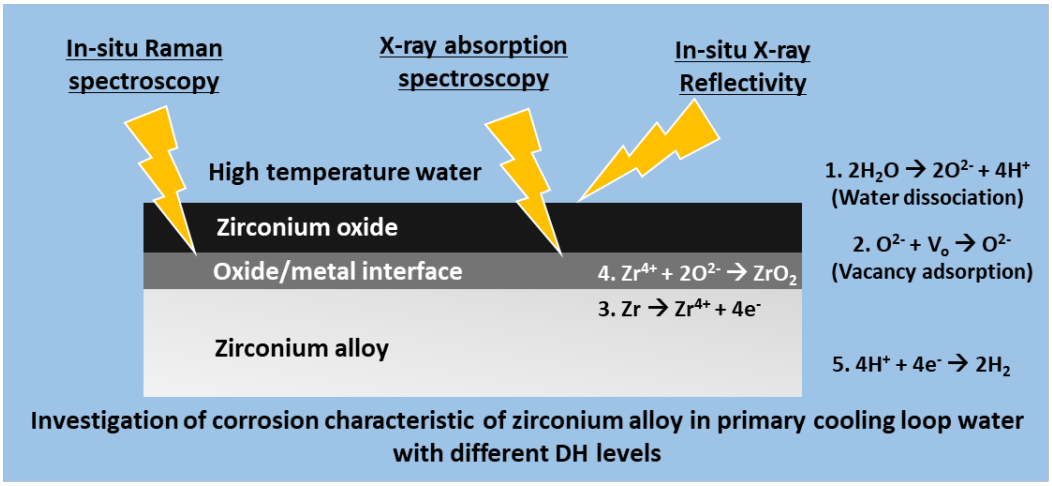

Figure 1-3 A diagram of approach of this thesis

2. Basic theory and literature study

2.1 Characteristic of zirconium alloys and zirconium oxide

2.1.1 Characteristic of zirconium alloys for nuclear industry

The PWRs utilize the zirconium alloys as fuel cladding materials, and the fuel rods are approximately 9.5 mm diameter and 4 m height. These fuel rods consist the fuel assemblies, and the bundle of fuel assemblies compose the core of nuclear power plant as illustrated in Fig. 1-1. There are various types of zirconium alloy with the different chemical composition of alloying elements. The Table 2-1 presents the chemical composition of the zirconium alloys which are used in the nuclear power plant [18]. Zircaloy-2 was used for the fuel cladding materials of boiling water reactors (BWRs), however due to the hydrogen absorption characteristic of Ni, it was not a suitable candidate for cladding materials of PWRs. Therefore, Zircaloy-4 had been developed, in which Fe was replaced the Ni. Zr-Nb alloy was developed with high Nb contents, however they showed poor behavior for the claddings of BWRs. Nevertheless, Zr-Nb alloys were used for the pressure tubes due to their low hydrogen pick-up characteristic, and they utilized in the Russian Vodo-Vodyanoi Energetichesky Reactor (VVER). Nowadays, M5 and ZIRLO are developed, with controlling Nb, Fe, and S for enhancing the corrosion resistance in the primary coolant environment in PWRs. Both alloys reveal the low corrosion rate and limited irradiation growth.

The alloying elements in zirconium alloy have a low thermal solubility in α-Zr, therefore they form precipitates in the zirconium matrix like second phase particles (SPP) and Laves phases. Previous study showed that the solute elements like Cu, Nb and Sn in Zr alloy can increase the corrosion resistance [19]. Especially, a high fraction of Nb can be a reason of the β-niobium precipitates in the Zr alloy. It has been reported that these β-niobium precipitates are adsorbed in zirconium oxide, and the oxidation rate of precipitates is much slower than oxidation rate of Zr matrix [20]. Also, the higher Sn concentration zirconium alloy normally leads the cracks in the oxide because of the delayed oxidation caused by the solute elements [21]. In Zr alloy, the Sn and Nb are dissolved and they could be segregated at the grain boundary of zirconium oxide. These Sn and Nb atoms are not oxidized until the value of oxygen potential are enough for oxidizing the Sn and Nb atoms. This can enhance the corrosion resistance of Zr alloy, and it could be one of the evidences of the difference corrosion resistance with the chemical composition of zirconium alloy. Furthermore, the tetragonal phase zirconium oxide can be stabilized by the precipitates from the oxide/metal (O/M) interface, and they could affect the characteristic of oxide conduction [22].

2.1.2 Corrosion kinetics of zirconium oxide

The zirconium oxide has 3 different phases: cubic, tetragonal, and monoclinic. The temperature for the phase transition of tetragonal to monoclinic is 1478 K, and it for tetragonal to cubic phase is 2650 K, as illustrated in Fig. 2-1 and Table 2-2. [23–25]. Therefore, the monoclinic and tetragonal oxide phases are only observed after the corrosion experiment, by transmission electron microscopy (TEM), and ex-situ Raman spectroscopy [17,26]. Near the O/M interface, the dominant phase is tetragonal, and the fraction of monoclinic zirconium oxide increases as the distance from the O/M interface increases [27]. Note that, the compressive stress of bulk zirconium oxide is much lower than compressive stress near the O/M interface. It has been reported that, the formation of monoclinic phase oxide is caused by the tetragonal zirconium oxide phase transformation, and it is highly connected to the corrosion resistance of Zr alloy in simulated primary water environment [7,16].

It also has been reported that oxygen ions diffuse inward direction from the oxide surface to the O/M interface during the oxidation [4]. At the beginning of oxidation, a dense and thin tetragonal zirconium oxide was firstly formed because of the compressive stress near the O/M interface, with small size equiaxed grains. The protective oxide film, acted as a barrier, was formed at the pre-transition period, and the tetragonal oxide becomes columnar shape to reduce the stress in the oxide [28]. The oxide layer thickness increases, as the corrosion time increases, however the compressive stress decreases as far from the O/M interface, as a result of the phase transformation of tetragonal to monoclinic oxide [15,29].

Table 2-2-1 Chemical composition of zirconium alloys for nuclear industry (concentration in wt. % or ppm) [18]

	Sn	Nb	Fe	Cr	Ni	O	S
Zircaloy-2	1.2 ~ 1.5		0.07 ~ 0.2	0.1	0.005	0.12	
Zircaloy-4	1.2 ~ 1.7		0.18 ~ 0.24	0.1		0.1 ~ 0.14	
M5		0.8 ~ 1.2	~ 500 ppm			0.11 ~ 0.16	10 ~ 35 ppm
Zr-2.5Nb	1	2.5 ~ 2.6	~ 650 ppm			0.12 ~ 0.15	
ZIRLO	1.2	1	0.1			0.09 ~ 0.12	

From previous studies, the kinetics of Zr alloy consists of pre-transition and post-transition stages, and the breakaway phenomena occurs during the transition period [30]. A pre-transition stage can be defined by cubic and parabolic growth kinetics and a post-transition stage can be defined by linear growth kinetics [3]. A cyclic oxide growth behavior is generally observed in the post-transition stage, and it can be illustrated by a break down and repair of zirconium oxide occurred after the transition period. From the Wagner's law for the oxidation kinetics, the oxidation rate of zirconium alloy can be described by an empirical law $w = Ct^n$, where w is the weight gain (units: mg/dm^2), t is the oxidation time, and C and n are the constants. Each different zirconium alloy has its own value of n. The oxidation rate in the pre-transition period is well matched with the empirical law of the oxidation [3,31]. Therefore, the weight gain of zirconium oxide during the corrosion can influence on the rate of oxidation, and it is correlated with the diffusion process across the zirconium oxide layer by the water species and oxygen ions [32,33]. Furthermore, the formation of the nano-sized cracks and the second phase precipitates near the O/M interface prior to the transition period also can influence on the diffusion rate of oxygen ion and corrosion resistance of zirconium alloys [34,35]. Hence, it is essential to investigate the characteristics of the zirconium oxide and O/M interface before the transition period, especially during the early stage oxidation.

The oxidation kinetics of zirconium alloys can be determined by measuring the weight gain or the oxide thickness of the sample as a function of oxidation time, as illustrated in Fig. 2-2 [31]. Also, the diffusion of hydroxyl and oxygen ions occurs in the O/M interface, it plays an important role in the zirconium corrosion mechanism. As mentioned above, the tetragonal phase is dominant in the O/M interface, and 4 different factors can stabilize the tetragonal phase, and they are oxygen vacancies, solute elements, compressive stress, and grain size. Therefore, it is important to control the above factors for enhancing the corrosion characteristic of zirconium alloy in the simulated primary coolant condition. The phase diagrams yield that the tetragonal zirconium oxide can be stable phase for temperatures over 1150 ℃. However, the tetragonal zirconium oxide can exist at low temperature in the presence of the high compressive stress.

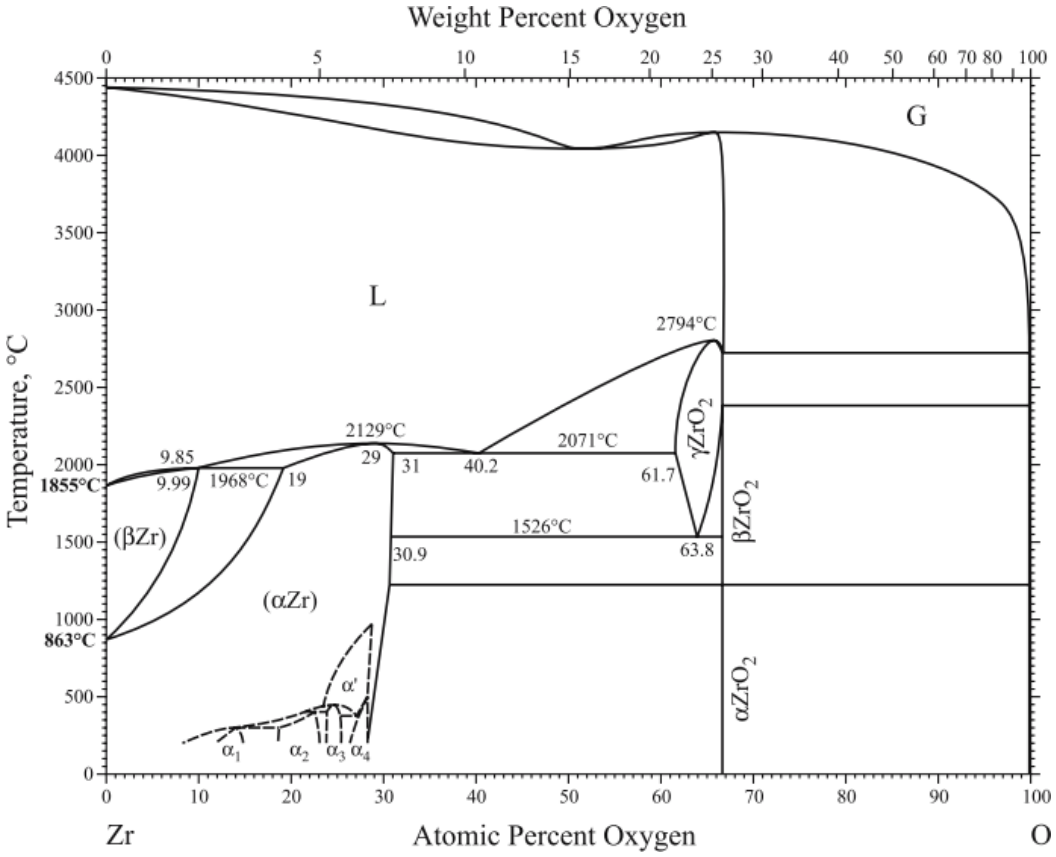

Figure 2-1 Zr-O phase diagram [23]

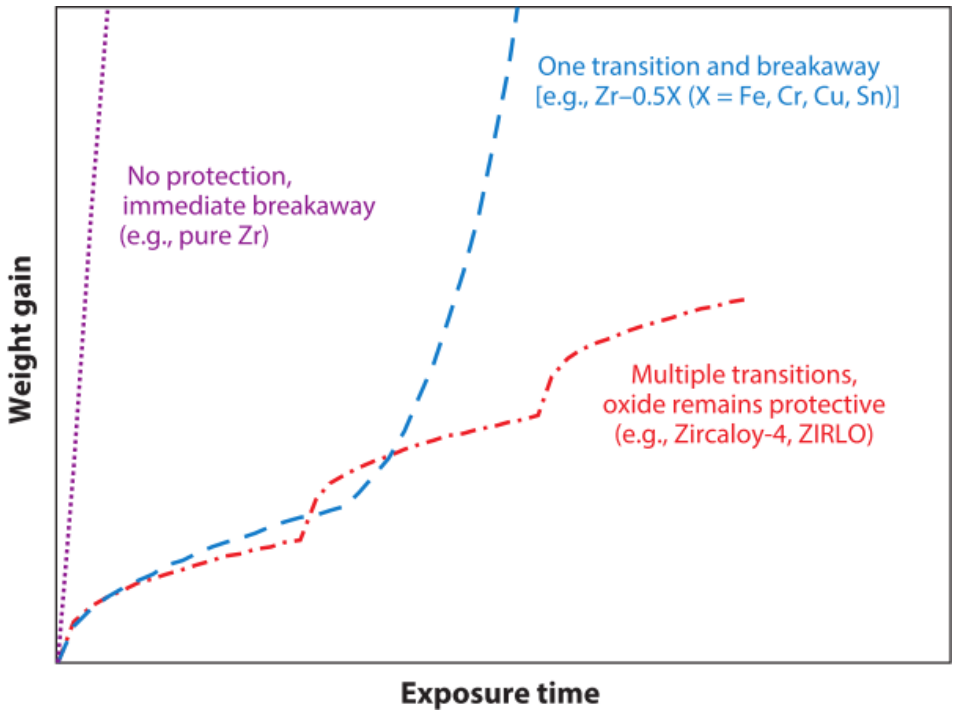

Figure 2-2 Schematic representation of corrosion of zirconium alloys [31]

Table 2-2-2 Characteristics of zirconium oxide with various phases [25]

	Monoclinic	Tetragonal	Cubic
Temperature range [℃]	~ 1170	1170 ~ 2370	2370 ~ 2680
Density [g/cm^3]	5.83	5.86	5.64
Cell parameter [Å]	a=5.147 b=5.206 c=5.313 α=γ=90° β=99.23° 123123	a=b=5.082 c=5.185 α= β =γ=90°	a=b=c=5.113 α= β =γ=90°

2.2 Primary water chemistry of pressurized water reactors

To transfer the heat from the fission reaction of nuclear fuel, the pressurized water reactors (PWRs) adopt the light water for the primary coolant for primary circuit. The PWRs consist of two main systems, primary and secondary circuit. The heated primary coolant flows to the secondary circuit where the steam is generated for rotating the turbines with generating the electric power. The primary coolant condition is maintained pH 6.9 to 7.4, because the operation below pH = 6.9 could lead to heavier corrosion products depositions on fuel cladding. To satisfy the pH condition of primary coolant, the boron concentration is 1200 ppm from boric acid (H_3BO_3), and the lithium concentration is 2 ppm from lithium hydroxide (LiOH). Boric acid is generally used for a neutron absorber for controlling the activity of the reactor core, but the acidic condition due to boric acid can enhance the corrosion rate of structure materials. Therefore, lithium is used to adjust pH value of primary coolant of PWR. In Table. 2-3, the detail guideline of PWR primary coolant condition has been described.

Also, minimization of dissolved oxygen concentration is one of the important issues of PWR chemistry control, because dissolved oxygen leads the stress corrosion cracking and general corrosion of structure materials of reactor coolant system. For minimizing the corrosion of primary circuit system, hydrogen is added in the primary coolant to maintain the reducing environment. The PWR water chemistry guidelines from EPRI stated that the range of 25 – 50 cm^3/kg of DH is recommended, however some have been experiencing primary water stress corrosion cracking degradation of nickel-based alloy [36]. Previous studies mentioned that the DH can influence on the stress corrosion cracking behavior of nickel-based alloy, especially the high DH can delay the crack initiation time and crack growth rate [10,37–39]. Therefore, to mitigate corrosion in structure materials like stainless steel, and Ni-based alloys used in pressurized water reactors, the primary water chemistry is strictly under controlled. But there is not enough data available about the effect of DH levels on corrosion characteristic of zirconium alloy, oxide, and its phase transformation.

Table 2-2-3 Guideline value of PWR primary coolant chemistry [36]

Parameter	**Guideline value**
Dissolved oxygen [ppb]	Below 5
DH [cm^3/kg, STP]	15 ~ 50
F [ppb]	Below 50
Cl [ppb]	Below 50
SiO_2 [ppb]	Below 100
SO_4 [ppb]	Below 50

2.3 Raman spectroscopy and electrochemical impedance spectroscopy

When the light is scattered into the materials, the scattered light has different frequency compared to the incident light, and this phenomenon was first discovered by C.V. Raman. The target molecule adsorbed the energy of the scattered light, and it leads the vibration motion of molecules and the frequency changes of light. To observe the Raman shift, the target molecule should be symmetric structure, and the Stokes Raman scattering is generated by relaxation of molecule from exited state to the first vibration energy state. Anti-Stokes Raman scattering occurs when the molecule is already in the elevated vibration energy state. Figure 2-3 illustrates the energy diagram of Raman scattering.

Previous research adopted Raman spectroscopy for analyzing the oxide characteristic in aqueous solution, especially high temperature condition [40,41]. Most of all, in-situ Raman spectroscopy was adopted to study the corrosion mechanism of metal alloys in high temperature aqueous solution. Also, the effects of water chemistry, including dissolved oxygen levels and boron concentration, were investigated from previous study, and surface enhanced Raman spectroscopy technique was also used for enhancing the signal-to-noise ratio with using noble metal [41,42]. Zirconium alloy was also analyzed with in-situ Raman spectroscopy in air-saturated water at a pressure of 15.5 MPa and temperatures ranging from room temperature to 400 ℃ in optical flow cell. Figures 2-4 and 2-5 represent the Raman spectroscopy results with comparing monoclinic zirconium oxide power, and different temperature. This reveals that the characteristic of zirconium oxide could be influenced by the water temperature.

However, there is not enough Raman analysis data for zirconium oxide formed at high temperature water condition, especially simulated primary water coolant loop environment of PWRs. Therefore, in-situ Raman spectroscopy was adopted to analyze zirconium oxide in primary coolant condition. Also, the DH levels were changed for investigating the effect of DH level on transformation of zirconium oxide phase during corrosion.

Electrochemical impedance spectroscopy (EIS) is a well-established analysis method for investigating the electrochemical reactions, with measuring the characteristic of oxides, coated materials, and electrodes. This EIS method can be applied for lots of research areas, including the corrosion research field. The Ohm's Law is a fundamental law for the electric field, and it states the current through a conductor between two spots is proportional to the voltage of two spots. It can be defined as $R=V/I$, where R is a resistance of circuit in ohms (Ω), V is the voltage in volts (V), and I is the resulting current flow of the circuit in amperes (A). In alternating current circuit, the impedance (Z) can be defined as a value of circuit tendency to impede the current flow. The Z can be expressed as $Z = V_{ac}/I_{ac}$ where V_{ac} is the potential applied the alternating current circuit and I_{ac} is the current output.

Figure 2-6 illustrates the circuit with the solution resistance R_e, and in series with a charge transfer resistance R_{ct} in parallel with a double layer capacitor of oxide C_{dl}. In this circuit, the impedance

can be calculated the summation of Z_{RE} and Z of parallel circuit of double layer capacitance and resistance. The impedance response is consisted of real part of impedance and imaginary part of impedance, $Z = Z_r + jZ_j$ where Z_r represents the real part of impedance, and Z_j is the imaginary part of impedance. ($j = \sqrt{-1}$). From the EIS measurement, the thickness of oxide can be calculated with using permittivity of oxide materials, and the capacitance of the oxide from Nyquist plot.

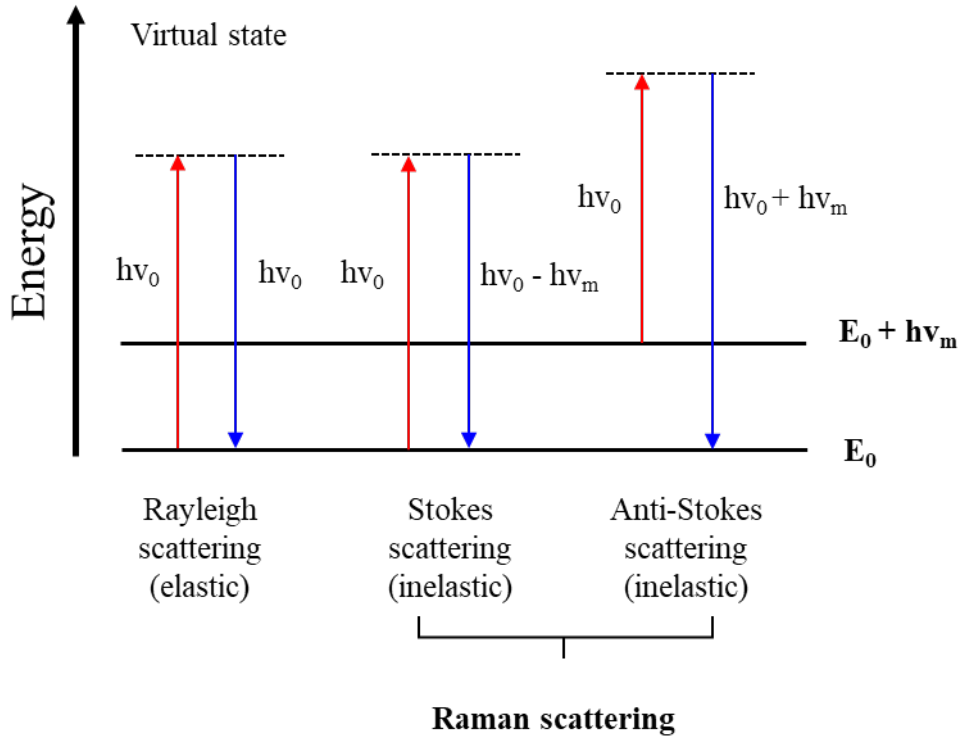

Figure 2-3 Schematic of energy diagram of Raman spectroscopy

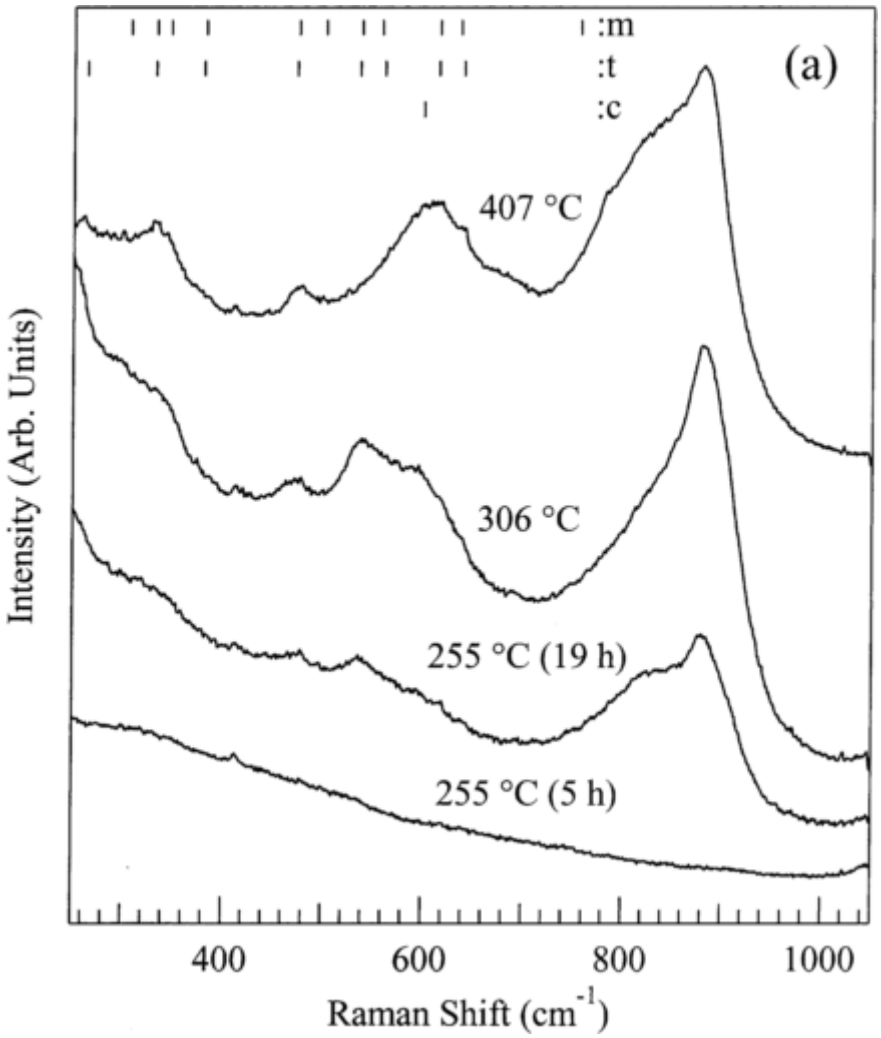

Figure 2-4 In-situ Raman spectra of zirconium alloy heated to 407 ℃ in aqueous solution [2]

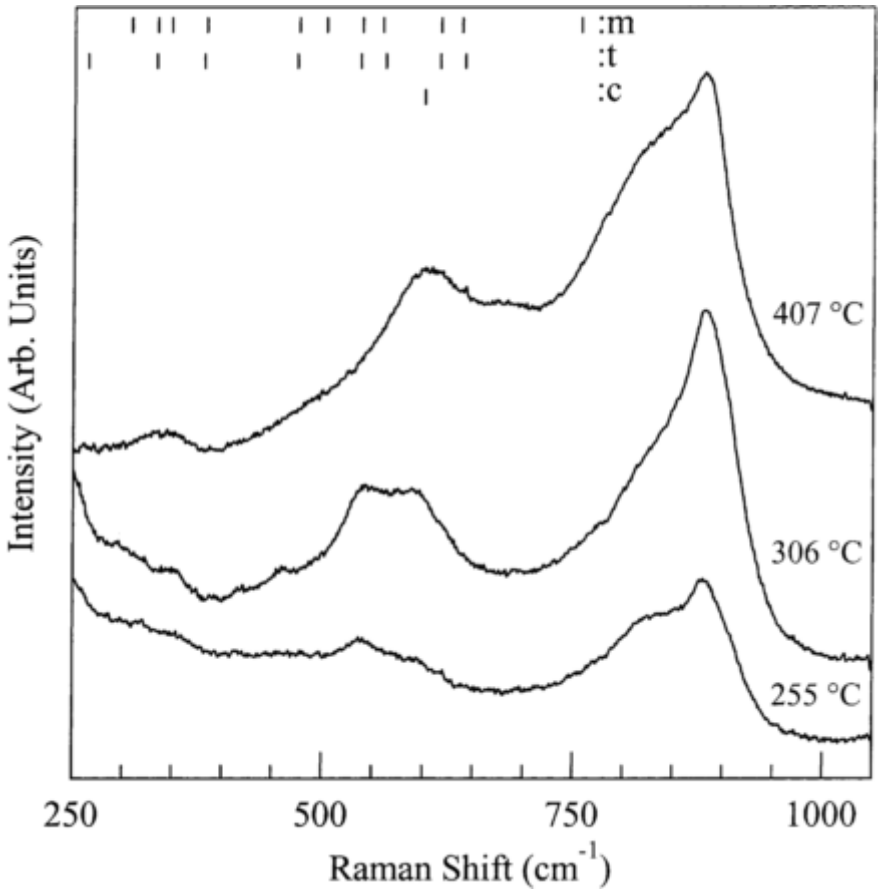

Figure 2-5 In-situ Raman spectra of zirconium oxide with different temperature [2]

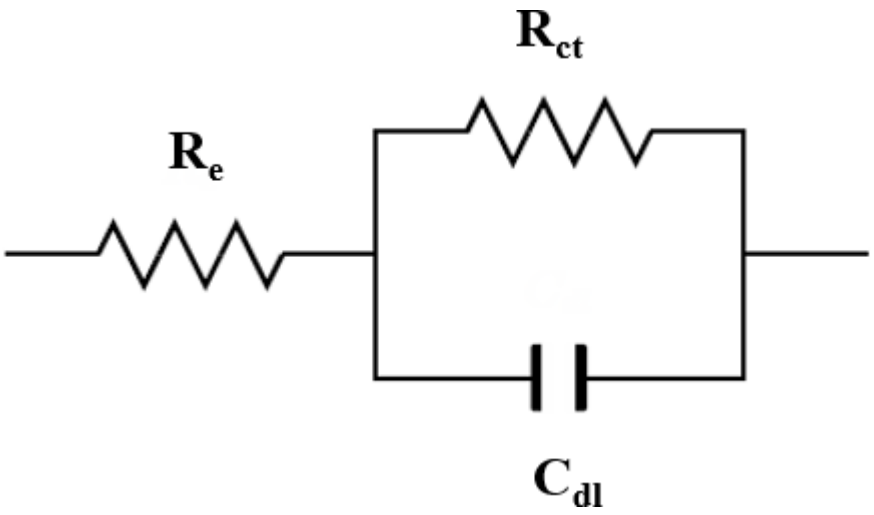

Figure 2-6 Electrical circuit with solution resistance, charge transfer resistance and double layer capacitor

2.4 Scanning transmission X-ray microscopy

Scanning transmission X-ray microscopy (STXM) is one method of X-ray microscopy, X-ray beam focuses onto a small spot of a sample. X-ray from zone plate passes the optical spectrum analyzer and it scans the sample on the sample holder. The intensity of transmitted X-ray is recorded with the position of the sample. The schematic of STXM is presented in Fig. 2-6. STXM analysis can give high spectral resolution about 20 ~ 30 nm, and the radiation damage on the sample from STXM analysis us two orders of magnitude lower than electron energy loss spectroscopy.

X-ray absorption spectroscopy (XAS) is also synchrotron X-ray based techniques, which can reveal the electronic and geometric structure of a sample. With using a crystalline monochromator, the photon energy can be tuned, and the core electrons could be excited from 100 eV to a few hundred keV. The excitation of a 1s electron occurs at K-edge, and it of 2s and 2p electrons occurs at L edge. In addition, the excitation of 3s, 3p, and 3d electrons occurs at M edge. One of the XAS analysis is X-ray absorption near edge structure (XANES), and the other is extended X-ray absorption fine structure (EXAFS). XANES uses photoelectron which has the energy range from 10 to 150 eV. EXAFS uses the relative high kinetic energy. Previous studies suggested that XAS are sensitive for analyzing the thin film structure, especially thin oxide on the metal during the corrosion [43,44]. In this thesis, STXM method is adopted for investigating the effects of DH on corrosion characteristic of zirconium alloy and phase distribution of zirconium oxide. The electronic structure of thin film oxide can be revealed by STXM analysis after sample preparation with focused ion beam (FIB) method. The structural properties could be examined by using synchrotron X-ray at soft X-ray Nanoscopy beamline (10 A beamline of Pohang Accelerator Laboratory (PAL), South Korea). Local electronic structure of the oxidized zirconium samples is investigated by using X-ray absorption fine structure spectroscopy at the O K-edge, and the energy range of O K-edge is set as 520 to 560 eV.

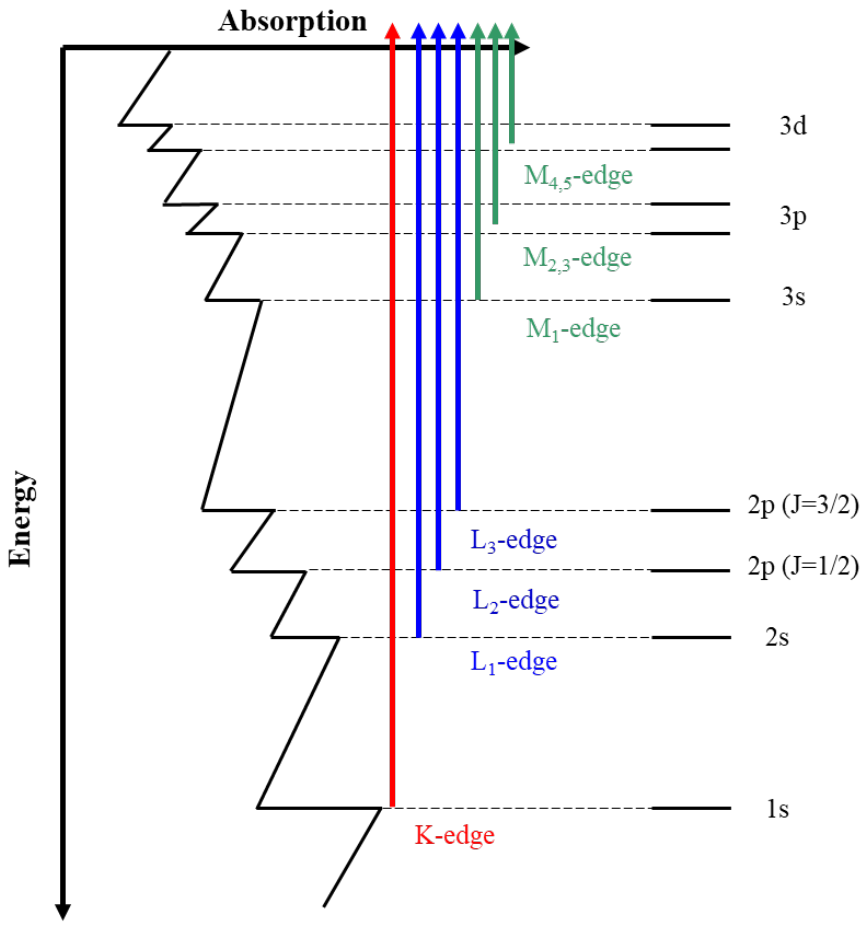

Figure 2-7 Schematic diagram of X-ray adsorption spectroscopy edges

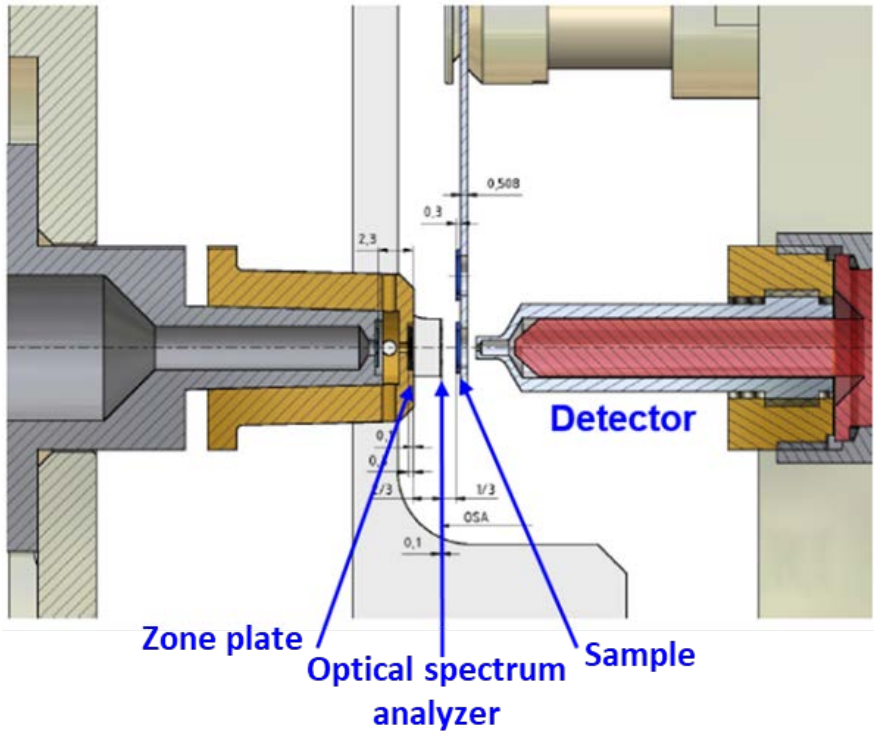

Figure 2-8 Schematic image of STXM analysis instrument in Pohang accelerator laboratory 10A beamline

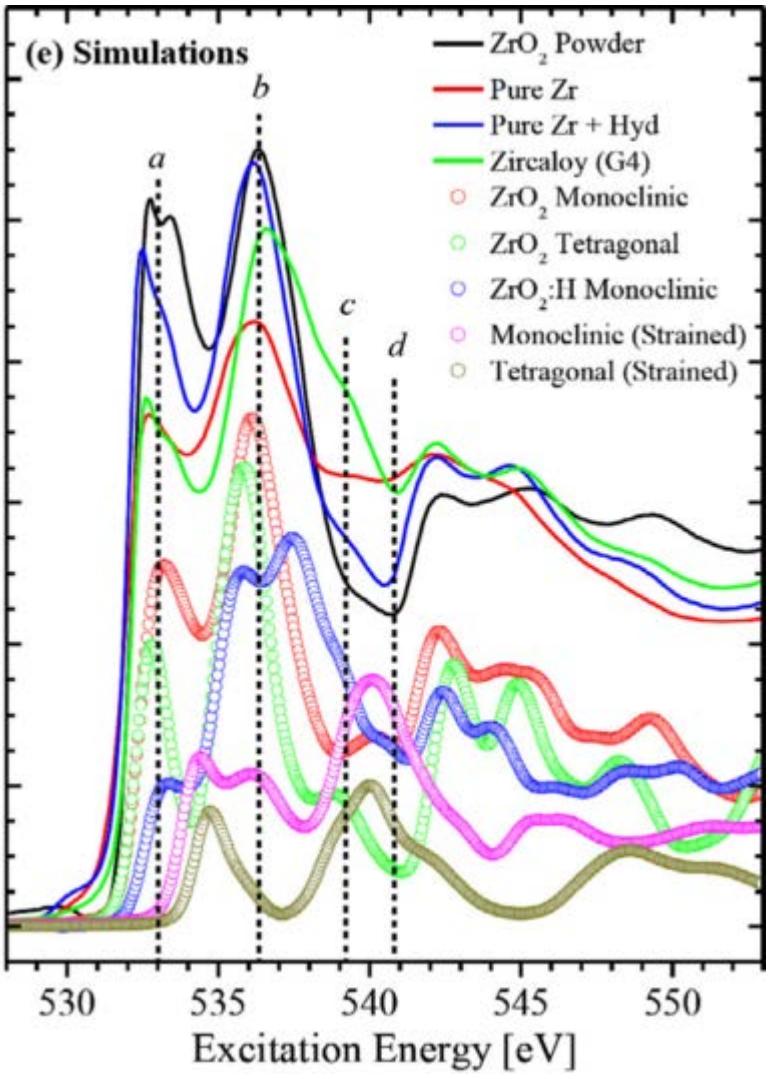

Figure 2-9 Example of oxygen K-edge X-ray adsorption spectra [45]

2.5 High resolution X-ray reflectivity

The mineral-water interface is one of the important issues of corrosion of metal, because the first step of corrosion reaction is occurred in water and metal interface. There are plenty of previous studies which treat the X-ray reflectivity measurement, and the basic theory of the X-ray reflectivity (XRR) has been summarized by P. Fenter [46,47]. The basic technology is to reflect direct X-ray beam to atomic flat surface and measure the intensity of reflected X-ray beam in the specular direction. If the interface is not flat layer, the interference of wave occurs, and destructive and constructive interferences can be observed. All waves have the interference characteristic and the reflectivity of X-ray follows the Bragg's law as shown in equation 2-1.

$$n\lambda = 2d\sin(\theta) \tag{2-1}$$

In equation 2-1, n is the diffraction order, λ is the wavelength, and d represents the d-spacing of Bragg plane, where θ is the incident angle of X-ray. Also, the interference condition could be described by reciprocal lattice with using momentum transfer vector, **Q**, which has both a direction and a magnitude. Figure 2-9 illustrates the Bragg's scattering geometry with angular term and momentum transfer terms. Equation 2-1 can be replaced by using momentum vector, and it is shown in equation 2-2.

$$\mathbf{Q} = \mathbf{K_f} - \boldsymbol{K_i} = k(\boldsymbol{u_f} - \boldsymbol{u_i}) \tag{2-2}$$

$$Q = |\boldsymbol{Q}| = \frac{4\pi}{\lambda}\sin(\theta) \tag{2-3}$$

In Equations 2-2 and 2-3, $\boldsymbol{u_f}$ and $\boldsymbol{u_i}$ are the unit vector of reflected and incident beam, respectively with having a wave vector $\boldsymbol{K} = 2\pi/\lambda$. $\boldsymbol{Q}$ has the unit of inverse Ångstroms ($Å^{-1}$). The reflected beam intensity depends on the distribution of atomic positions along the surface normal direction.

The intensity of scattered X-ray is calculated by summing the amplitudes of scattered beam, ϵ_j, for each atom *j*. Then, the reflected beam intensity should be proportional to the structure factor of surface material, *F*, and the sum of scattered X-ray intensity is proportional of square of *F*. In equation 2-4, the relationship between intensity and structure factor is illustrated.

$$I \propto \left|\sum \epsilon_j\right|^2 = |F|^2 \tag{2-4}$$

In real case, the incident X-ray is scattered at every single atomic layer of target material, and it can be defined that the number of atomic layer is *N*. Then, the structure factor for N-silt layer is defined in equation 2-5, where *c* is regular separation of atomic layer and f_0 is the scattering strength of the layer.

$$F = f_o[(1 + \exp(-iQc) + \exp(-i2Qc) + \cdots + \exp[-i(N-1)Qc)] \tag{2-5}$$

$$= f_0 \exp\left(-\frac{i(N-1)Qc}{2}\right)\left[\frac{\sin\left(\frac{NQc}{2}\right)}{\sin\left(\frac{Qc}{2}\right)}\right]$$

Figure 2-10 illustrates the calculated scattered X-ray intensity as different number of atomic layer, *N*. Then, the scattering intensity can be presented as equation 2-6.

$$I \propto |F|^2 = f_0^2\left[\frac{\sin^2\left(\frac{NQc}{2}\right)}{\sin^2\left(\frac{Qc}{2}\right)}\right] \tag{2-6}$$

The intensity of scattered X-ray is flat for $N = 1$, which indicating that the interference is not occurred because one single layer does not have something to interfere. As *N* value increases, the scattered intensity increases to Bragg peak position, and intensity and sharpness of Bragg peaks develop as N becomes large [47].

For Semi-infinite lattice, it does not show high frequency oscillations between the Bragg peaks. This is because X-ray that scatters from the top interface has nothing with which to interfere. The linear attenuation of X-rays over a distance, x, follows the form $\exp\left(-\frac{x}{\Lambda}\right)$, where Λ is the linear attenuation length, and η is the typical per-layer attenuation factor.

$$\begin{aligned} F_{ctr} &= f_o[(1 + \eta\exp(-iQc) + \eta^2\exp(-i2Qc) + \cdots \\ &\quad + \eta^{N-1}\exp[-i(N-1)Qc)] \\ &= f_0\frac{\eta^N\exp(-iNQc) - 1}{\eta\exp(-iQc) - 1} = f_0\frac{1}{1 - e^{-iQc}} \end{aligned} \tag{2-7}$$

The equation 2-7 can be derived with assuming that the value of N becomes very large, and $\eta < 1$, $\eta^N \approx 0$. Therefore, equation 2-8 can be derived from equation 2-7.

$$I_{ctr} \propto |F|^2 = \frac{|f_0|^2}{4\sin^2\left(\frac{Qc}{2}\right)} \tag{2-8}$$

Figure 2-11 illustrates the crystal truncation rod (CTR) structure factor with different regular separation and outmost layer occupancy. The intensity of scattered X-ray is influenced by the distance of each atomic layer and the electron density of the target layer, which is the occupancy of the atom. It leads that the shape of CTR structure factor is very sensitive to the termination structure of the target material structure. Consequently, the quantity of the CTR structure factor can be divided into two parts, the F_{surf} from the modified surface layer, and F_{sub} from the semi-infinite substrate of the target crystal structure.

Previous studies introduced the XRR measurement technique for investigating the water interaction with metal surfaces like corrosion, hydration, and electrochemistry reaction [48,49]. The sub-Ångström scale structure of water/oxide interface can be investigated with XRR measurement; however, it should be conducted with data analysis because the obtained data from XRR measurement is the intensity of scattered light, and the goal of XRR experiment is the electron density of the particular atom. The effective electron density of each atom $\rho_{\text{eff}}(z)$ can be written as a Gaussian function in

equation 2-9.

$$\rho_{\mathrm{eff}}(z) = \frac{Z}{(2\pi)^{\frac{1}{2}} u_{eff}} \exp[-\frac{1}{2}\left(\frac{z - z_0}{u_{eff}}\right)^2] \quad (2\text{-}9)$$

where z_0 can be determined by the position of material, u_{eff} is determined by electron distribution, and Z is the atomic number of the element. Therefore, the resolution of XRR measurement can be derived like following equation 2-10, where Q_{max} is the maximum value of scattering data.

$$\mathrm{L_{res}} = 2\pi / Q_{max} \quad (2\text{-}10)$$

From XRR measurement, the single crystal yttria-stabilized zirconium oxide (YSZ) (111) substrates were used for investigating the hydration structure of water/oxide interface. 15.000 keV incident X-ray was used, and the focused beam size was 0.1 mm (vertical) × 0.7 mm (horizontal) with the flux of $\sim 1.1 \times 10^{11}$ photons/s.

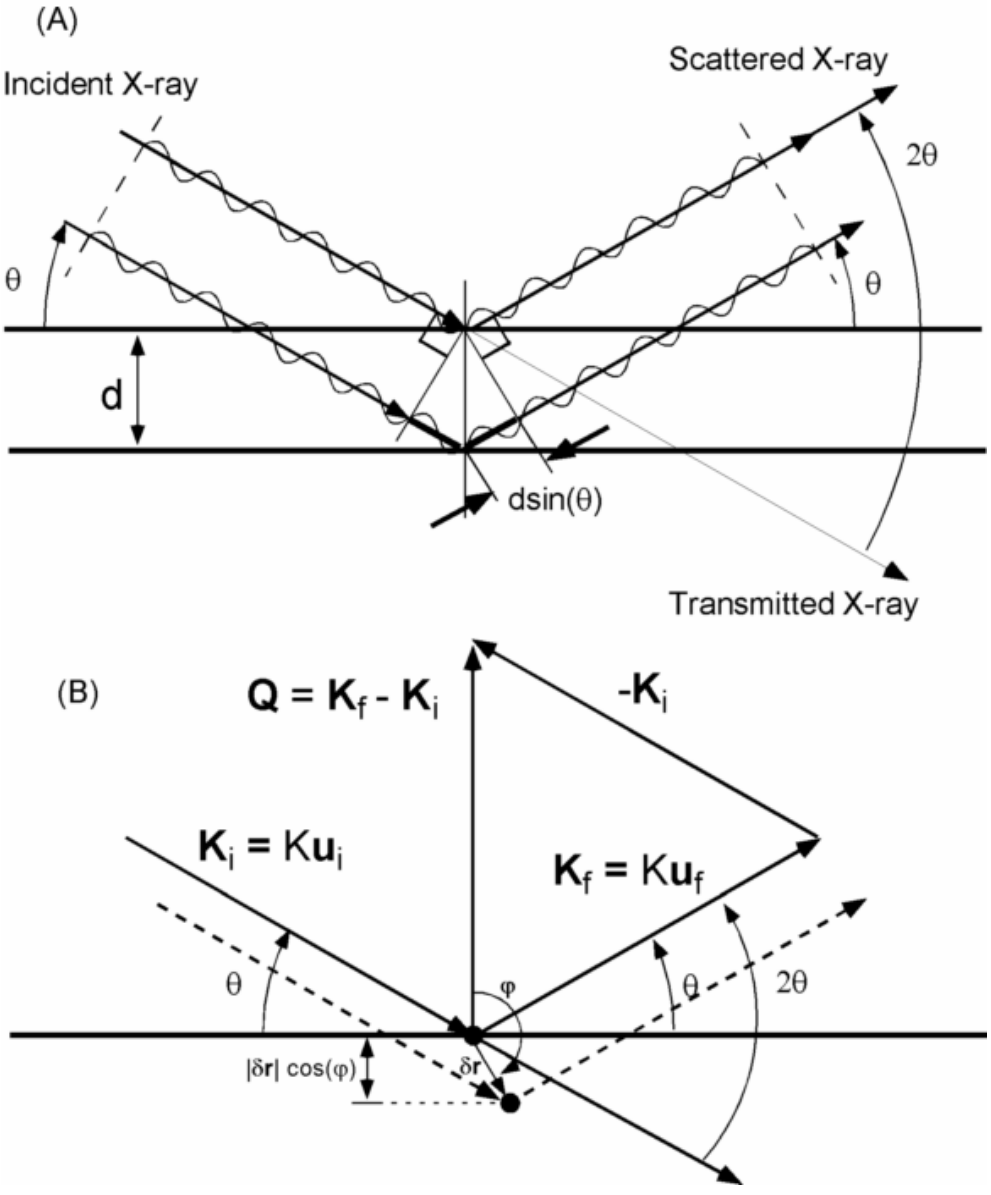

Figure 2-10 The Bragg scattering geometry (A) X-ray path length for two parralel layers, (B) described by momentum transfer vector, **Q** [47]

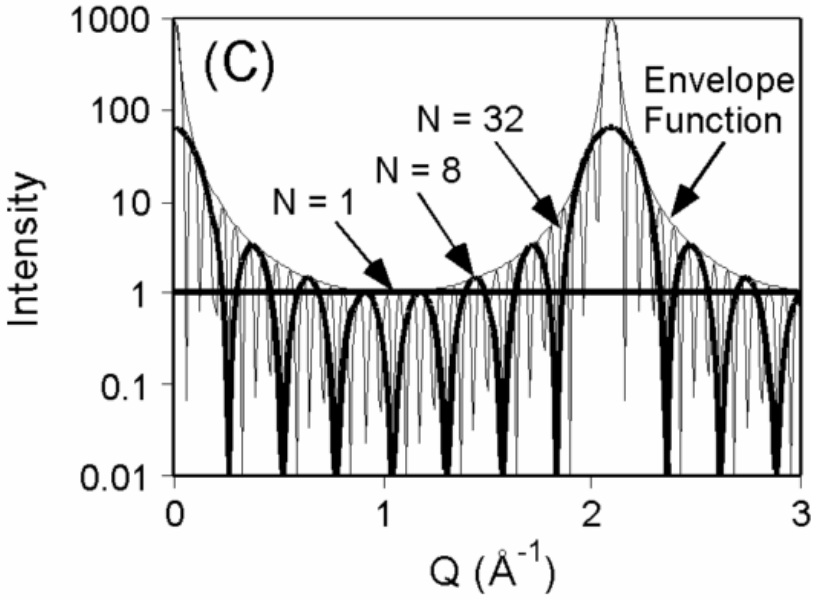

Figure 2-11 Scattered X-ray intensity as different number of atomic layer, *N* [47]

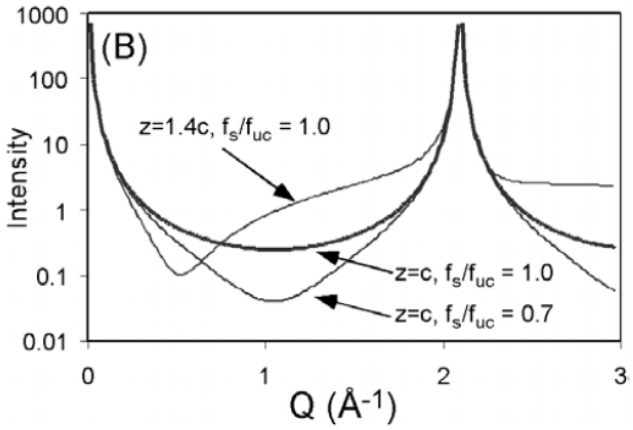

Figure 2-12 The CTR structure factor with different regular separation and outmost layer occupancy [47]

3. Methods

3.1 In-situ oxide investigation of zirconium alloy using Raman spectroscopy and EIS

3.1.1 Introduction

As mentioned in section 2.1, there are three different phases of zirconium oxide, monoclinic, tetragonal, and cubic. TEM analysis can be found the tetragonal and monoclinic zirconium oxide, however previous reported work on zirconium oxide are limited, because ex-situ analysis methods were only adopted [34,50–52]. The corrosion environment can influence on the structure and phase of the zirconium oxide formed on the specimen. Therefore, in this thesis, in-situ Raman spectroscopy was used for in-situ investigations, as the experimental system can be used at the high pressure and temperature water environment. In-situ Raman spectroscopy can be used for investigating the phase and characteristic of oxide film on metal surface. Then, in-situ EIS can measure the capacitance value of oxide layer during the oxidation, and the resistivity value of zirconium oxide can be calculated.

3.1.2 Materials

A plate of Zr-Nb-Sn alloy was used for corrosion experiment at the simulated primary coolant water condition. In Table. 3-1, the chemical composition of Zr-Nb-Sn alloy is illustrated. The plate of Zr–Nb–Sn alloy sample was ground from 400 to 800 grits with SiC papers and polished up to 1 μm with diamond pastes. Lastly, a colloidal alumina paste (0.05 μm) was used to polish the Zr-Nb-Sn alloy for minimizing the deformation of specimen.

3.1.3 Experimental

For simulating the high pressure and temperature conditions of PWRs, a system including water chemistry controlling loop and autoclave was constructed. The schematics of the system used for the corrosion experiment, in-situ Raman analysis, and EIS analysis are illustrated in Figs 3-1 and 3-2. Using those instruments, the temperature was set as 360 ℃ and the pressure was set as 20 MPa for simulating the primary water of PWRs, with using the high-pressure pump, pre-heater, and band heaters. Distilled water (18 MΩ·cm) was used for producing primary circuit condition, which contained 1200 ppm boron ion from H_3BO_3 and 2 ppm lithium ion from LiOH. Also, the dissolved oxygen level can be controlled below 6 ppb, and the pH is controlled from 6.9 to 7.4. In addition, back pressure regulator was instrumented for adjusting the DH level from 2.49 to 4.15 mg/kg.

In Fig 3-3, the equivalent circuit for EIS analysis is represented. The zirconium oxide has two layers, one is a barrier layer and the other one is an outer layer. The barrier layer thickness is tens of

nanometers, however the outer layer have a greater oxide thickness (maximum 100 μm) [53]. The zirconium oxide is divided into two layers and each layer has its own resistivity and capacitance. Using equivalent circuit, the capacitance can be calculated using Z-view simulation and the oxide thickness of each layer is obtained. The R_e is a solution resistance, R_{in} is inner layer resistance, R_{out} is an outer layer resistance, C_{out} is an outer layer capacitance, C_{in} is inner layer capacitance, and W_o is Warburg element of the circuit. After consummating the corrosion experiment system, the shakedown process had been started for preventing the unexpected effect on zirconium oxidation from the oxide from autoclave. The passivation of autoclave was conducted at the same condition of zirconium corrosion experiment, 360 ℃ and 20 MPa with bubbling with nitrogen and oxygen for making fully oxidized autoclave surface. In Fig. 3-4, the conductivity and temperature data during the passivation procedure is represented. At the final step of passivation, the outlet conductivity was below 0.25 μS/cm.

In this study, in situ Raman spectroscopy measurements were performed using a RamanRXN™, manufactured by Kaiser Optical Systems, Inc., which uses a 532-nm-wavelength krypton ion laser with a maximum power of 100 mW, and the irradiation area in the specimen was 100 μm^2. For preventing the beam radiation damage to the zirconium alloy specimen, the power density at the specimen surface was held below 10 mW/cm^2. The detail descriptions of the in situ Raman system are presented in the authors' previous studies [9,50].

In situ Raman spectroscopic measurements with the corrosion tests were performed for Zr-Nb-Sn alloy in a primary water of pressurized water reactors with using an autoclave system, which is specially constructed for the present study. The water chemistry data including exposure temperature, pressure, conductivity, dissolved oxygen, and dissolved hydrogen concentration were measured and strictly controlled.

The Zr-Nb-Sn specimens were exposed until 100 d for two different dissolved hydrogen levels, 2.49 and 4.15 mg/kg. And, the in-situ Raman spectra were measured for 30, 50, 80, 100 d from start-up. The measured Raman spectra were compared for investigating the effects of dissolved hydrogen on the corrosion characteristic of zirconium alloy. For each measurement, in situ Raman spectra was collected for 30 m and repeated 2 times for increasing the signal-to-noise ratio. Prior to analyzing Raman peaks analysis, the baseline correction and Svizy-Golay methods were performed for the smoothening process. After each in situ Raman spectroscopy measurement, the Zr–Nb–Sn alloy specimen was removed from the autoclave for ex situ measurements.

The ex situ investigation was performed to characterize the oxide layer of the specimen using JEOL JEM-2100F TEM in coincidence with energy dispersive X-ray spectroscopy. The focused Ga-ion beam milling method was employed using a Quanta 3D Dual-Beam SEM to prepare the TEM samples. Prior to focused ion beam milling process, the specimen surface was coated using carbon sputtering to prevent ion beam damage and surface contamination. The acceleration voltage, and the lattice resolution

were 200 kV, and 0.102 nm, respectively. In situ Raman spectroscopy and the TEM analysis results were compared for a comprehensive understanding of the effects of dissolved hydrogen on the zirconium oxide characteristics.

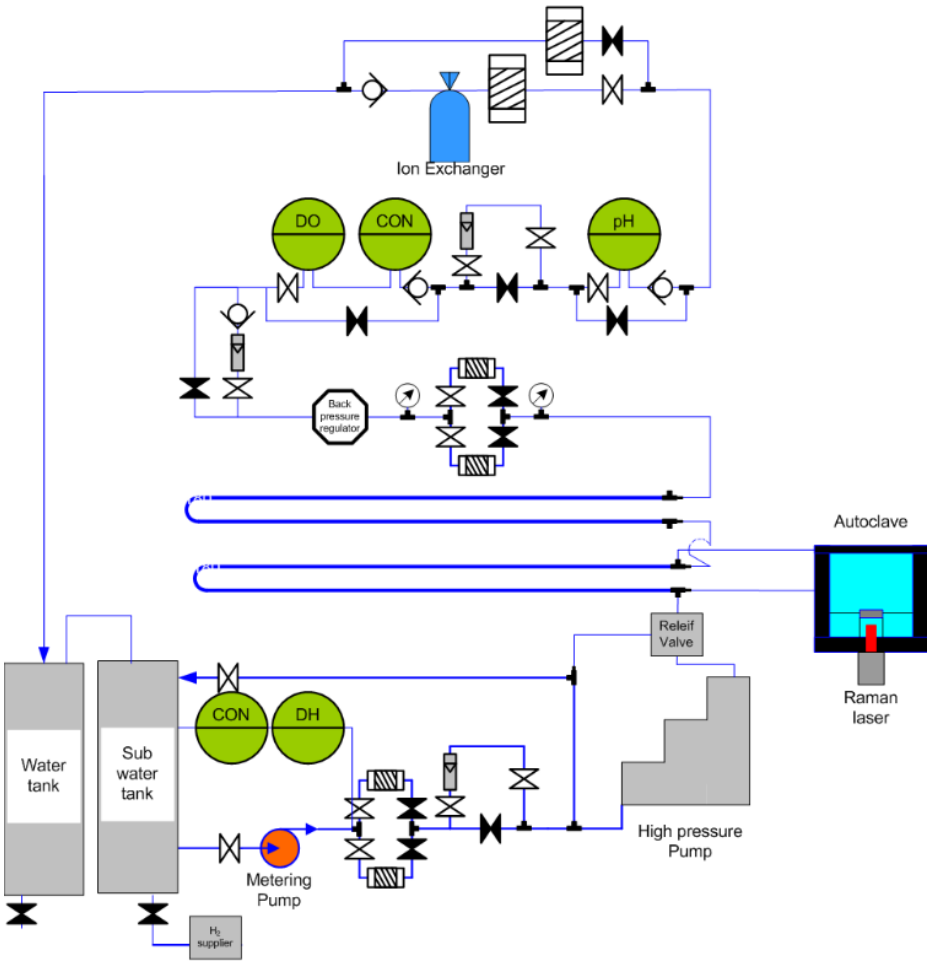

Figure 3-1 Schematic of in-situ Raman spectroscopic and corrosion experiment for Zr-Nb-Sn alloy

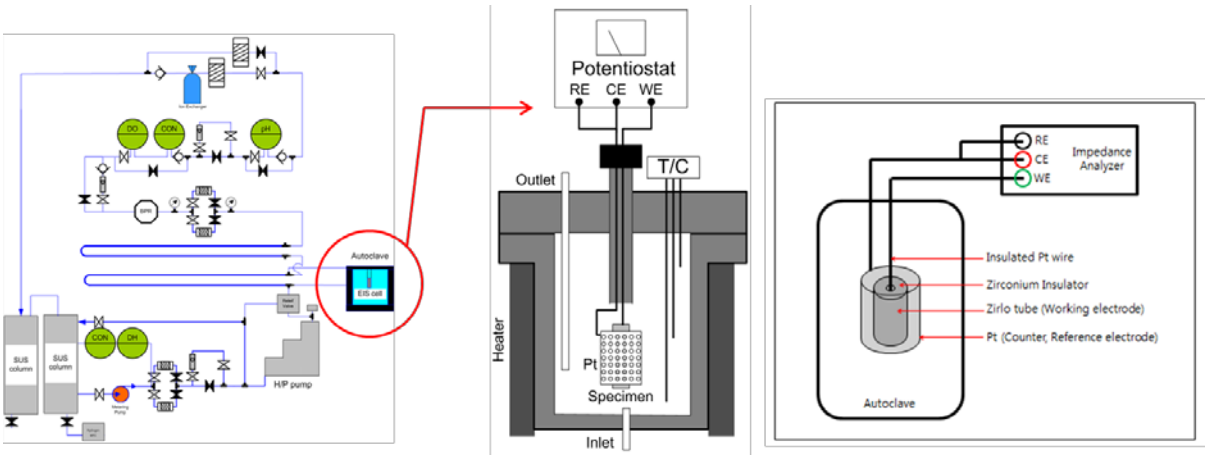

Figure 3-2 Schematic diagram of oxidation loop and autoclave inside for in situ EIS spectroscopy

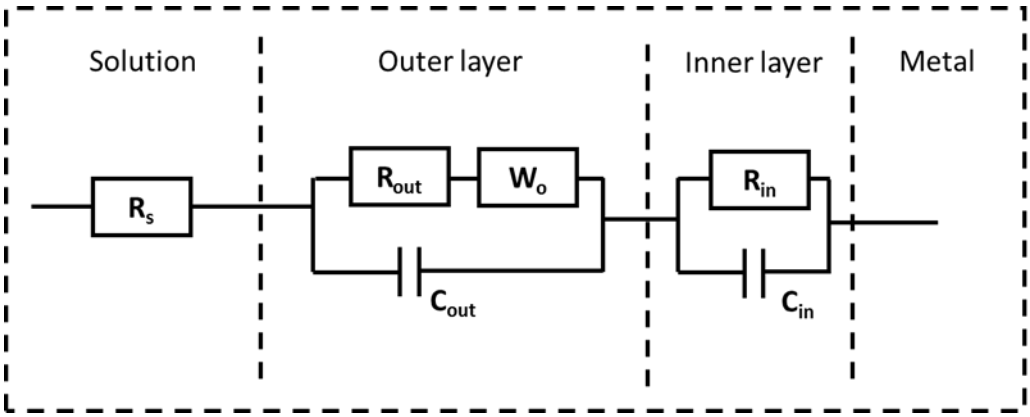

Figure 3-3 Equivalent circuit for EIS analysis

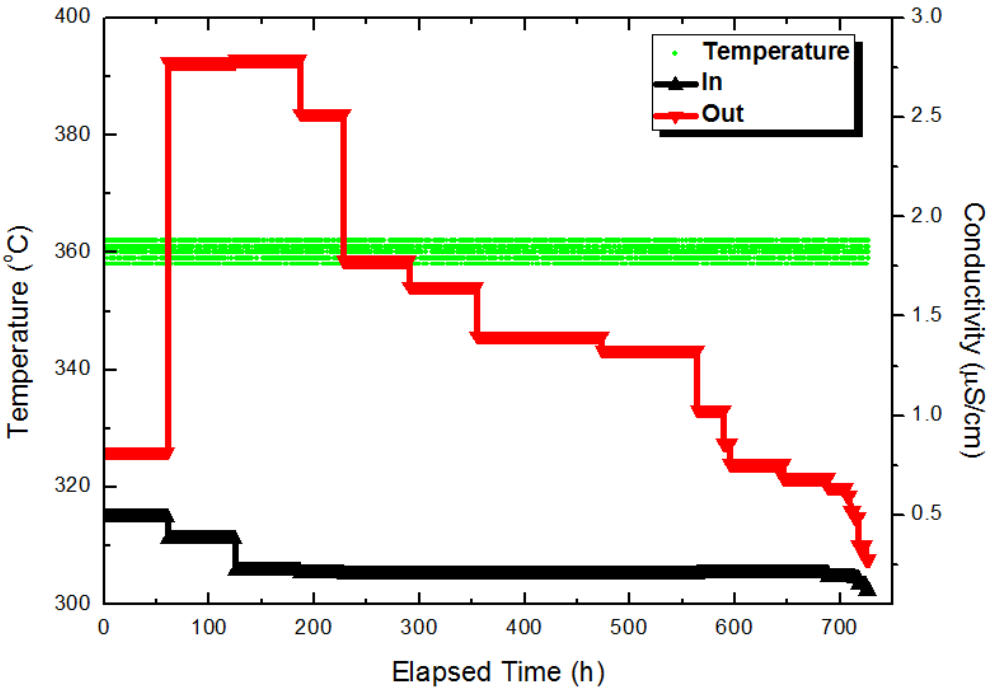

Figure 3-4 The data of conductivity and temperature during passivation procedure

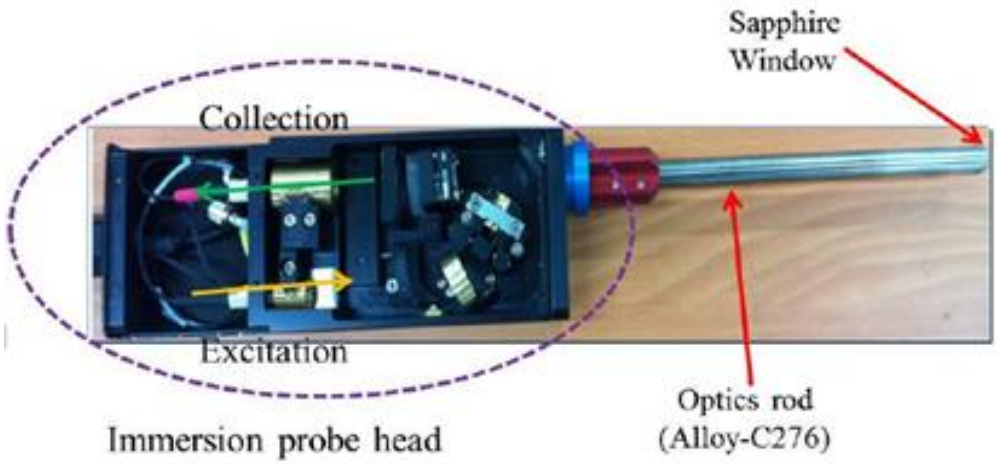

Figure 3-5 Image of in-situ Raman spectroscopy instrument [54,55]

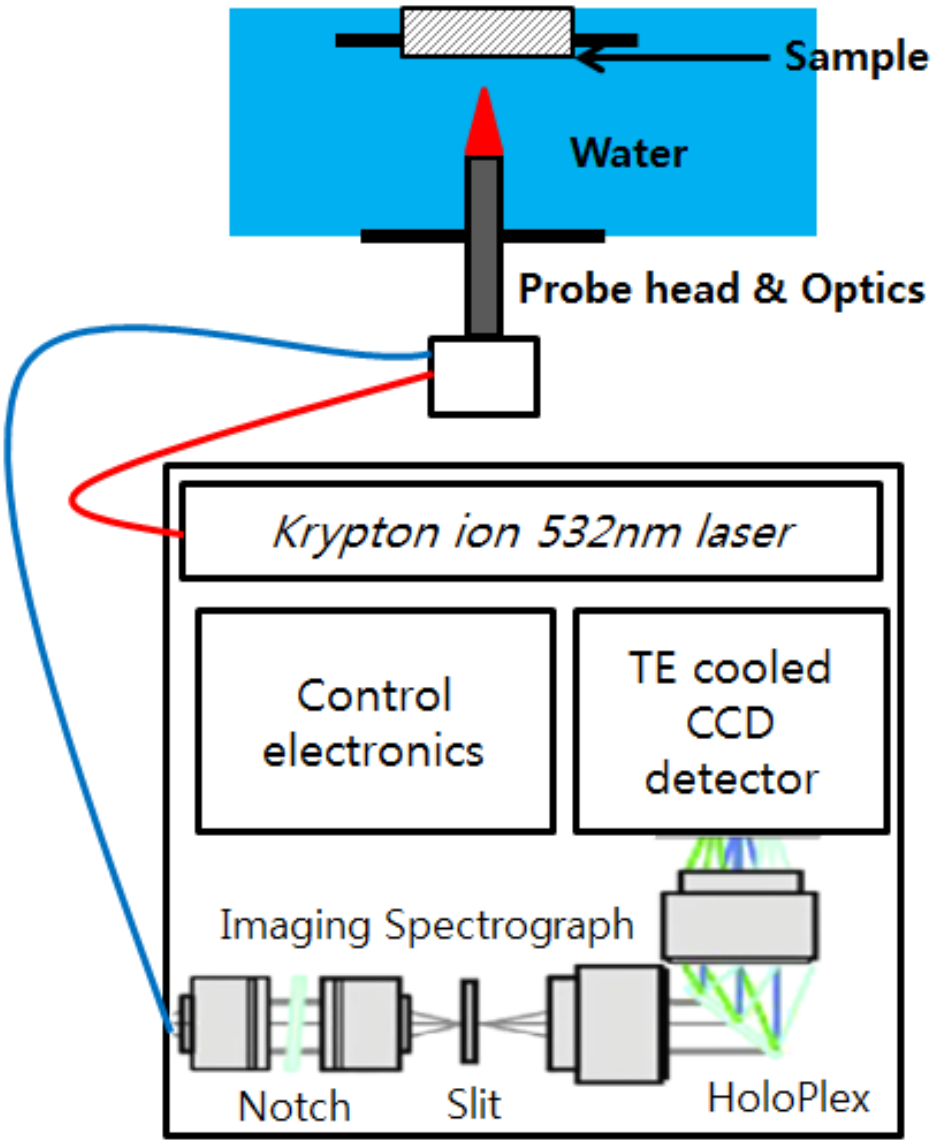

Figure 3-6 Schematic of in-situ Raman spectroscopic system with the autoclave and sample

Table 3-1 Chemical composition of the zirconium alloy (main alloying elements in wt.%)

Element	Nb	Sn	Fe	Hf	C	N	O	Zr
Composition	0.96	0.76	0.18	0.002	0.1	0.03	0.62	Balance

3.2 Investigation of electronic structure of zirconium oxide with scanning transmission X-ray microscopy

3.2.1 Introduction

Investigation based diffraction studies has shown that due to the compressive stresses, tetragonal phase fraction is the highest near the O/M interface, where the compressive stress is relatively higher than the middle of the zirconium oxide. As oxidation time increases, the proportion of monoclinic zirconium oxide increases while that of tetragonal oxide decreases [17,56]. Detailed characterization of the oxide structure and the tetragonal phase fraction using high-energy synchrotron X-ray diffraction on zirconium alloys and metastable tetragonal phase fraction is previously reviewed: The previous study has shown that X-ray absorption spectra are sensitive to the thin film structure [43]. However, the corrosion of zirconium alloy is quite complex, and the corrosion of zirconium alloy starts by a protective oxide film, with following a parabolic oxidation rate [57]. To identify structure of the zirconium oxide, and the O/M interface, EELS (electron energy loss spectroscopy), and APT (atom probe tomography) have adopted a layer zirconium oxide before the first abrupt transition [4]. In this thesis, a Zr-Nb-Sn alloy is used for investigating with scanning transmission X-ray microscopy (STXM) for 100 d oxidation, which is close to the first transition time of the zirconium alloy oxidation.

3.2.2 Materials

For STXM analysis, the Zr–Nb–Sn specimens were oxidized for 100 d at 2.49 and 4.15 mg/kg DH conditions, and the oxidized samples were obtained after 30, 50, 80, and 100 d from the beginning of the experiment condition. The detail explanation about the corrosion experiment is illustrated in section 3.1.3.

3.2.3 Experimental

For STXM experiment, the focused ion beam method is adopted for sample preparation. For preventing the surface contamination from beam damage and impurities during the process, the surface was coated with sputtered carbon before gallium ion milling. The detail process of FIB process is presented in section 3.1.3.

The structural properties were examined by using the synchrotron X-ray at soft X-ray

Nanoscopy beamline (10 A beamline of Pohang Light Source, Republic of Korea). Local electronic structure of the oxidized zirconium samples was investigated by using X-ray absorption fine structure spectroscopy at the O K-edge, and the energy range of O K-edge is set as 520 to 560 eV. The monochromatic X-ray from beamline passes through the exit silt, and the size of it is from 10 to 30 μm. After exit slit, the X-ray penetrates the zone plate, and the zone plate acts as the focusing lenses if X-ray. Then, the optical spectrum analyzer adjusts the energy range of the incident X-ray. The sample is scanned by the incident X-ray, and the change of intensity of penetrated X-ray is detected at photon counter (detector). The resolution of STXM analysis is about 20 nm, and the X-ray scanning is conducted at the 100 kPa helium condition and the temperature is room temperature. The detail image of STXM experiment faculty is presented in Fig. 3-7, and the sample which is attached on the sample holder is presented in Fig. 3-8.

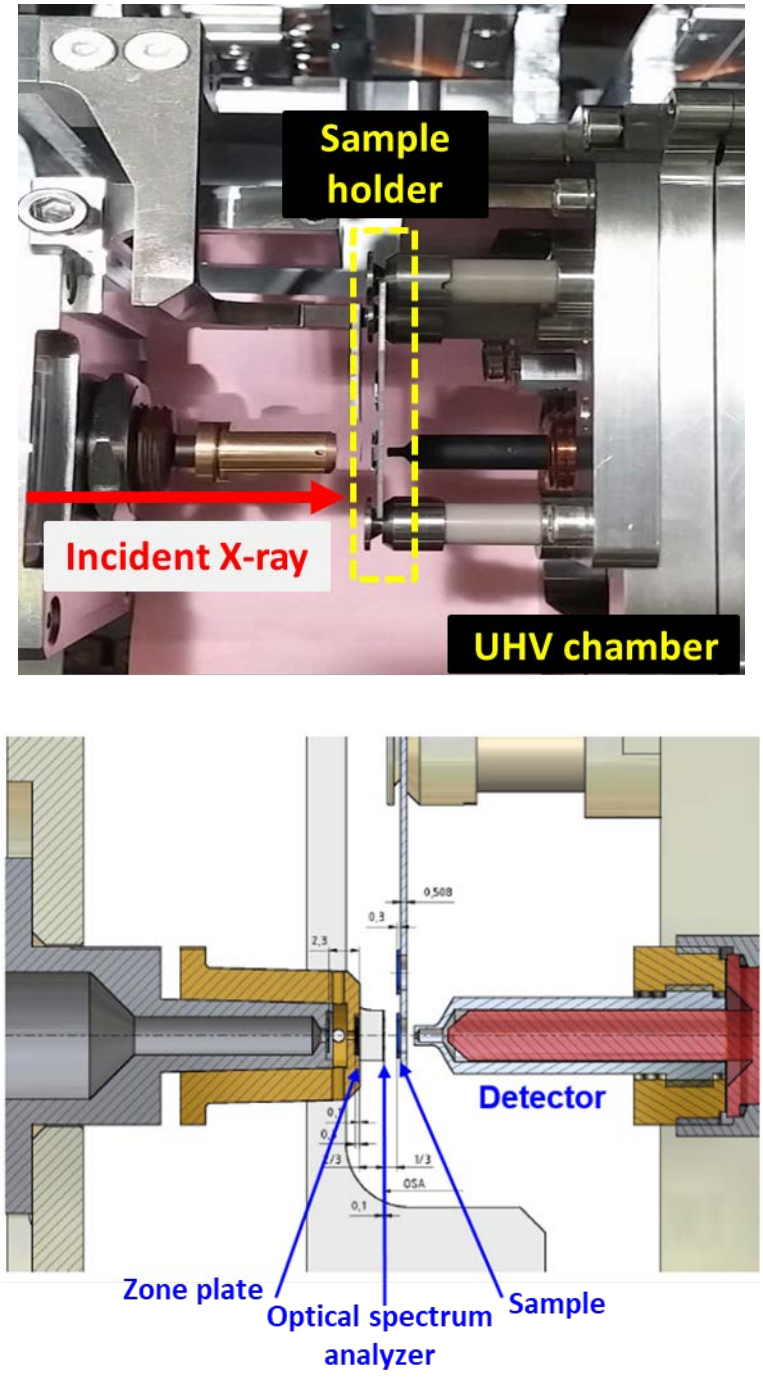

Figure 3-7 STXM experiment instruments in Pohang accelerator laboratory (PAL) 10 A beamline

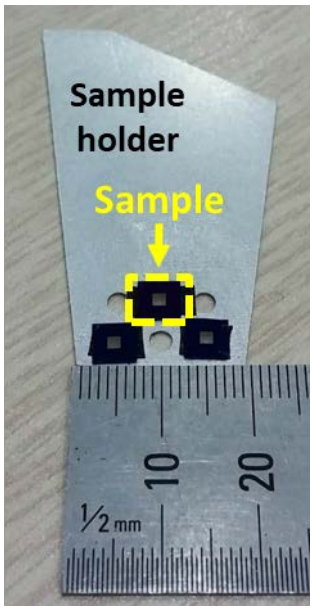

Figure 3-8 Sample and sample holder for STXM analysis

3.3 In-situ X-ray reflectivity study of interfacial structure between high temperature water and zirconium oxide

3.3.1 Introduction

In aqueous environment, the metal is oxidized due to the water species and the metal interaction, and also, water interaction with the metal surface is an important process such as corrosion electrochemistry [48]. Especially, the oxygen ions diffuse inward direction from the oxide surface to the O/M interface during the corrosion process, and the water species including oxygen ions and hydroxyl ions are formed in the water/solid interface. Therefore, it is highly required to investigate the interfacial structure of the water and the top layer of the alloy surface. The structural characteristic influences on the ion exchange between water and the metal, and it also effects on the corrosion characteristic of metal.

The reactions occurred at the metal oxide and water interface play an important role to determine the conditions of oxide degradation and corrosion propagation on meatal surface. Synchrotron based in-situ X-ray reflectivity technique has been applied for investigating various solid-water interfaces and addressed the fundamental questions by directly revealing the atomic or molecular scale structure at the interface. Its application to zirconium oxide and water interface is expected to reveal the detailed hydration and chemical processes at the interface, which is expected to contribute to solving the engineering problems in nuclear power plants.

3.3.2 Materials and sample preparation for thin film cell measurement

The YSZ single crystal (8 mol% Y_2O_3) were purchased from MTI Corporation in the dimensions of 10 × 10 × 1.0 mm^3 for (111) surfaces. The lattice constant, a_0, is 5.140 ± 0.008 Å. Along the surface normal direction of [111], the new unit cell structure is hexagonal packing and the lattice constants reduce to $a = a_0/\sqrt{2}$, and $c = a_0/\sqrt{3}$, resulting in d_{111} = 2.968 Å. The unit cell consists of one and one-half O atoms at the z = 0 plane, three Zr atoms at the z = ¼-d_{111} plane, three O atoms at the z = ¾-d_{111} plane, and one and one-half O atoms at the z = d_{111} plane. Along the surface normal direction, the stacking of unit cells results in periodic translations of three O, three Zr, and three O layers. The detail structure of YSZ (111) substrates is illustrated in Fig. 3-9. As shown in Fig. 3-9, All the termination atoms for the YSZ (111) substrates are oxygen, and it has a periodic plane arrangement of O-Zr-O-O-Zr-O.

The single crystal was washed in acetone, methanol, and distilled water with sonication for about 10 minutes at each step. This procedure was conducted a few times to remove the impurities on the substrate. The sample was kept in distilled water just after cleaning, until the sample was mounted to the cell for in-situ XRR analysis. The MTI Corporation (the brand name of the YSZ single crystal vendor) specified the miscut angle is less than 0.5°, which is far bigger than a typically acceptable tolerance level, 0.1°, but the polishing quality and the sample dimension precision was impressively high. The quantitative analysis is planned to obtain a deep insight into the hydration and chemistry of the ZrO_2/water interface.

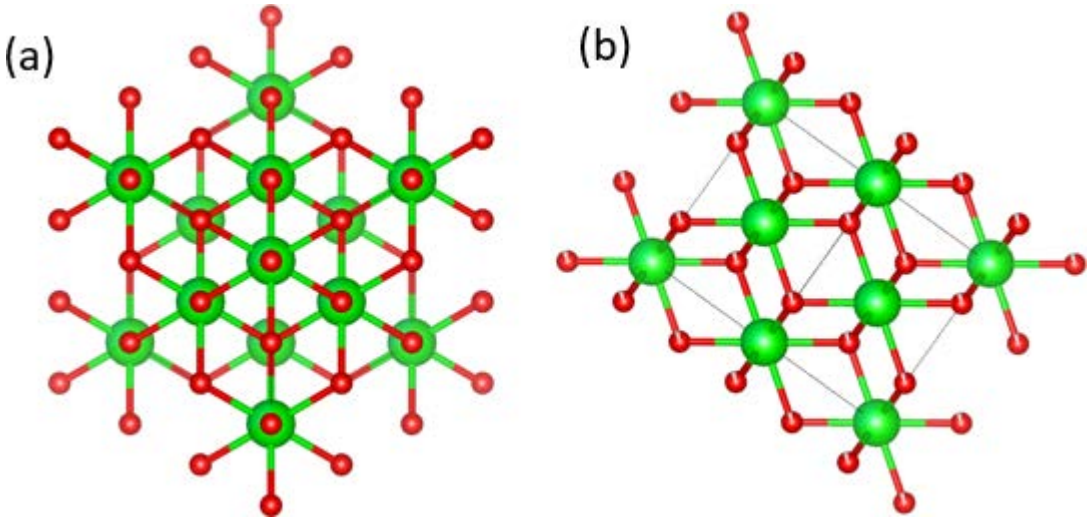

Figure 3-9 (a) A top view and (b) side view schematic of YSZ (111) substrates

3.3.3 Experimental procedure

The X-ray reflectivity measurement was performed at beamline Argonne Photon Source (APS) 33BM-C and at 9C beamline of the Pohang Light Source (PLS) at the Pohang Accelerator Laboratory (PAL) for (111) substrates. At 33BM-C beamline from Advanced photon source (APS), the full beam size at the sample was 0.1 mm (for the low 2θ angles to prevent beam spill-off) and 0.5 mm in vertical, and 0.8 mm in horizontal direction. The monochromatic beam (21 keV, $\Delta E/E \approx 10^{-4}$) was chosen by a Si (111) double crystal monochromator. The incident photon flux was ~10^{10}-10^{11} photons/sec. The beamline is equipped with a four-circle [47] diffractometer for surface diffraction experiment and a Pilatus 100K area detector is used as a default detector for the X-ray reflectivity measurement. An area detector, Pilatus 200K, was used for collecting the reflected intensities, which was mounted on the 2θ arm 930 mm away from the center of sample. The area of scattering on a detector is defined by a set of slits in front of the detector with a size of 8 mm (vertical) × 8 mm (horizontal) for data points mostly collected [48]. The use of area detector for the XRR measurement is described in the reference [47]. The sample was mounted in a thin film cell geometry on the goniometer center of the four-circle diffractometer as shown in Fig. 3-10. The sample was covered with 8 μm thin Kapton film, which holds the thin water film (~ 10-30 μm thick) on the single crystal substrate surface by the capillary force and serves as the X-ray transparent window. Deionized water is used for cleaning the cell and sample before assembled together and injected to the assembled cell to form a pristine YSZ-water interface system.

Also, for investigating the hydrothermal process of zirconium oxide in high pressure and temperature condition which is simulating the operation condition of PWRs, the hydrothermal cell for the measurement of high resolution X-ray reflectivity was used. The cell body is made of Inconel 625 alloys, and the X-ray and optical window is CVD polycrystalline diamond and the picture and schematic displays of component is in Fig. 3-11. This cell has been tested at 16-ID-D beamline of APS and 9C beamline of PAL for the YSZ (111) substrate in contact with the water described above.

The in-situ XRR measurements are conducted in deionized water system, at 2 different temperature conditions, the room temperature and 340 ℃, 20 MPa (2900 psi) condition. After measuring XRR data, the 1-D peak integration results of X-ray measurements was calculated with Python-based program, and the integrated data was analyzed by the interfacial atomic structure modeling.

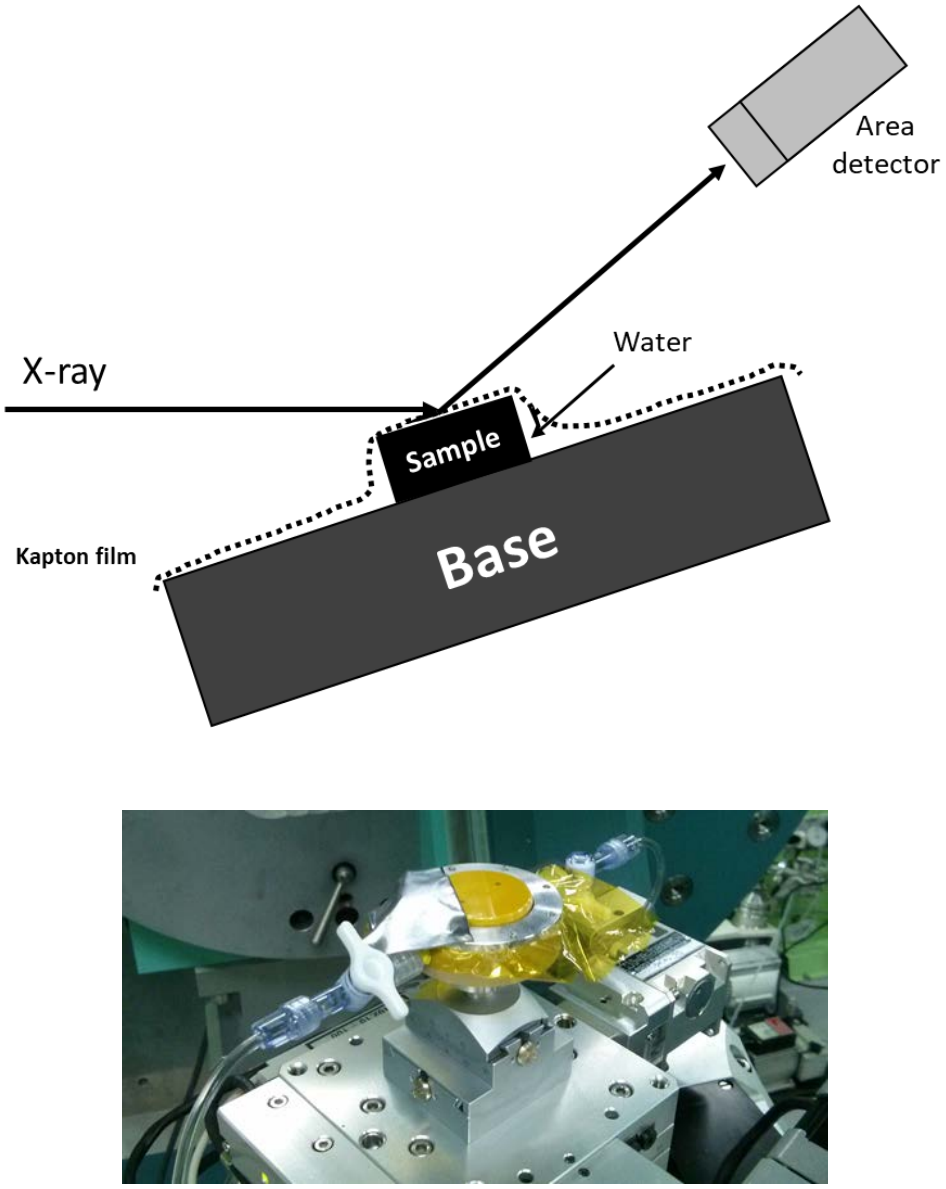

Figure 3-10 Schematic image and photo of the thin film cell and the experimental geometry for X-ray reflectivity measurement

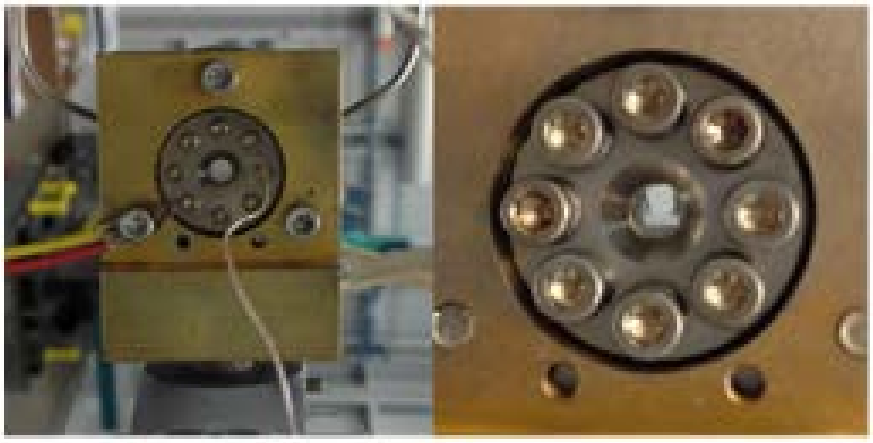

Figure 3-11 Pictures of the hydrothermal cell

4. Results

4.1 In-situ Raman spectroscopy and EIS results

4.1.1 In-situ Raman spectroscopy results at normal DH condition

Figure 4-1 presents the evolution of the in-situ Raman spectra of Zr-Nb-Sn specimen with a DH concentration of 2.49 mg/kg after 30, 50, 80, 100 d of oxidation. The Raman peaks at the 860 – 870 cm^{-1} range related to the borated ion from the dissolved H_3BO_3 in the primary water [54,58]. The strong intensity peaks, related to the sapphire window of the Raman laser tip, are marked as vertical bars in Fig. 4-1. The position of sapphire peaks are 414, 430, 575, and 747 cm^{-1} [59]. The spectrum in black is the Raman spectrum of the Zr-Nb-Sn alloy specimen oxidized for 30 d; the spectrum in red is the Raman spectrum of 50 d; the spectrum in blue is the Raman spectrum of 80 d; the spectrum in purple is the Raman spectrum of 100 d in 2.49 mg/kg DH.

After 30 d corrosion experiment, both monoclinic ant tetragonal zirconium oxide peaks are shown in Raman spectrum. The arrowed marks with ‘M’ mean the peak positions of monoclinic zirconium oxide, and the marks with ‘T’ mean the peak positions of tetragonal zirconium oxide, and they are illustrated in Table. 4-1. The tetragonal zirconium oxide peaks appear at 332 and 380 cm^{-1}, and these peaks are well matched with the previous studies [2,60]. When the oxidation time increases to 50 d, the tetragonal zirconium oxide peak at 332 cm^{-1} is merged with the monoclinic zirconium oxide, and only sharp peak at 333 cm^{-1} remains after 50, 80, and 100 d oxidation. Also, the tetragonal zirconium oxide peak which is positioned about 380 cm^{-1} became weak. The monoclinic zirconium oxide peaks about 616 and 640 cm^{-1} are shown in 30 d; however, it is not distinct, compared to 50, 80, and 100 d Raman spectra. Also, the peaks can be related to the monoclinic phase oxide are shown in 475 and 538 cm^{-1} [2]. As exposure time increases, monoclinic zirconium oxide Raman peaks becomes obvious, and this stands for the development of monoclinic zirconium oxide during the oxidation process. This can be also illustrated by phase transformation of zirconium oxide is occurred, tetragonal to monoclinic phase during the oxidation in primary coolant environment.

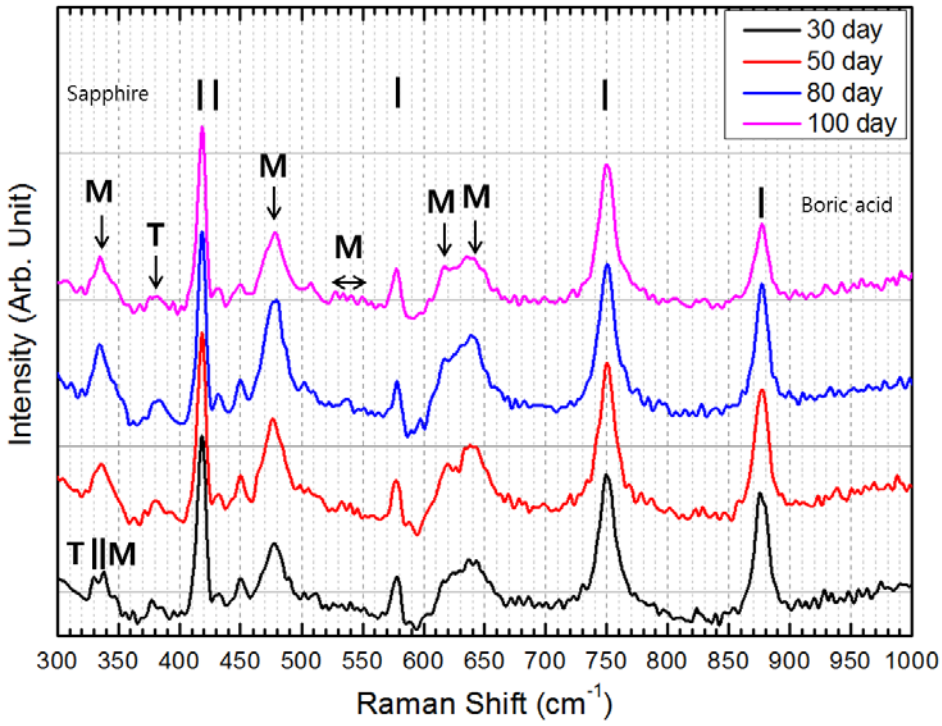

Figure 4-1 In situ Raman spectroscopy results of oxidized Zr-Nb-Sn alloy after different oxidation time at 2.49 mg/kg DH [61]

Table 4-1 Raman wavenumber of oxidized Zr-Nb-Sn at 2.49 mg/kg DH

Raman wavenumber (cm^{-1}) (Present study)	**Reference** [2,62]
330 (Tetragonal)	332 (Zr-Zr mode)
335 (Monoclinic)	334 (Zr-Zr mode)
336 (Monoclinic)	334 (Zr-Zr mode)
380 (Tetragonal)	380 (Zr-O mode)
476 (Monoclinic)	476 (O-O mode)
530 - 561 (Broad range)	(O-O mode)
617 (Monoclinic)	616 (O-O mode)
638 (monoclinic)	637 (O-O mode)

4.1.2 In-situ Raman spectroscopy results at high DH condition

In Fig. 4-2, the in-situ Raman spectra of Zr-Nb-Sn alloy specimen with 4.15 mg/kg DH concentration after 30, 50, 80, and 100 d of oxidation. The borate ion peaks from boric acid, and the sapphire peaks are also marked as vertical bar in Fig. 4-2. Unlike to previous case, tetragonal peak at 332 cm^{-1} is not well observed, and only monoclinic Raman peaks appear in the region of 330 – 340 cm^{-1} at 30 d. Also, the monoclinic peaks appear at 475, 538, 616, and 640 cm^{-1} and these peaks are well matched with the previous studies [2,50,63]. The tetragonal zirconium oxide peak is found at 380 cm^{-1}, however the intensity of it is much weaker than the 2.49 mg/kg case. As exposure time increases, the peaks at 616 and 640 cm^{-1} are related to the monoclinic zirconium oxide phase become distinct, and the tetragonal zirconium oxide peak remains only at 380 cm^{-1}. Also, the peak positions of zirconium oxide at 4.15 mg/kg DH are illustrated in Table 4-2.

The in-situ Raman spectroscopy result represents that the DH concentration can influence on the zirconium oxide phase in primary coolant condition. At a normal primary cooling loop water condition of nuclear power reactor, 2.49 mg/kg, the monoclinic and tetragonal phases of zirconium oxide appear at the beginning of corrosion, 30 d after start-up, and the peaks are separated, as represented in Fig. 4-1. This phenomenon demonstrates that tetragonal and monoclinic phase could be stable at 2.49 mg/kg DH level. At 4.15mg/kg case, the dominant peak is monoclinic phase, and this result supports the transformation of zirconium oxide phase is accelerated by the DH concentration in high temperature water.

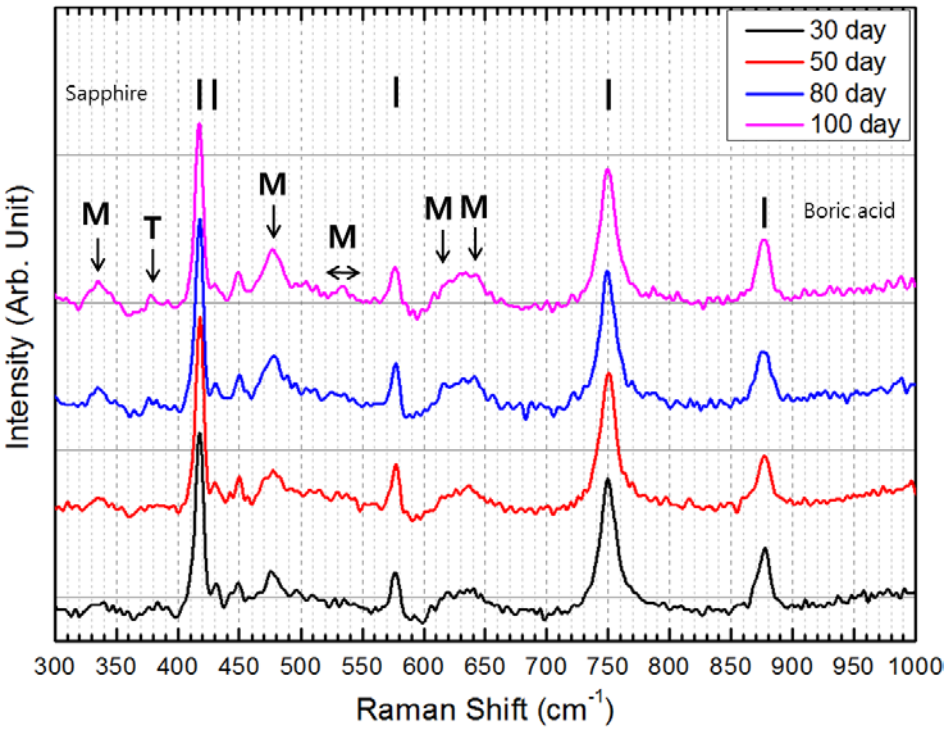

Figure 4-2 In situ Raman spectroscopy results of oxidized Zr-Nb-Sn after different exposure time at 4.15 mg/kg DH [61]

Table 4-2 Raman wavenumber of oxidized Zr-Nb-Sn at 4.15 mg/kg DH

Raman wavenumber (cm^{-1}) (Present study)	**Reference** [2]
334 (Monoclinic)	334 (Zr-Zr mode)
379 (Tetragonal)	380 (Zr-O mode)
476 (Monoclinic)	476 (O-O mode)
530 - 561 (Broad range)	(O-O mode)
617 (Monoclinic)	616 (O-O mode)
638 (monoclinic)	637 (O-O mode)
334 (Monoclinic)	334 (Zr-Zr mode)
379 (Tetragonal)	380 (Zr-O mode)

4.1.3 In-situ EIS measurement results at two different DH conditions

In Fig. 4-3, the Nyquist plots and fitted plots of in situ EIS for oxidized Zr-Nb-Sn specimen 2.49 mg/kg condition is presented. With using Z-view program, the parameters values after optimization on the experimental impedance data for zirconium oxide can be derived as shown in Table. 4-3. Nyquist plots show that there are two circles in results, the small one means inner oxide and the larger one means outer oxide. As oxidation time increases, the capacitance value of inner oxide and outer oxide are both decreases, then it leads the oxide thickness increases. The further SEM or TEM analysis is required for confirming the EIS results.

In Fig. 4-4, the Nyquist plots and fitted plots of in situ EIS for oxidized Zr-Nb-Sn specimen 4.15 mg/kg condition is also presented, and the parameter values after optimization on the experimental impedance data for zirconium oxide of 4.15 mg/kg condition are shown in Table. 4-4. The inner layer oxide thickness is calculated around 20 nm at 2.49 mg/kg case, and 50 to 110 nm at 4.15 mg/kg case. In both case, the outer layer oxide thickness increases as the oxidation time increases. Also, in high DH concentration, the oxide thickness is slightly thick compared to the normal condition for 40 d oxidation experiment.

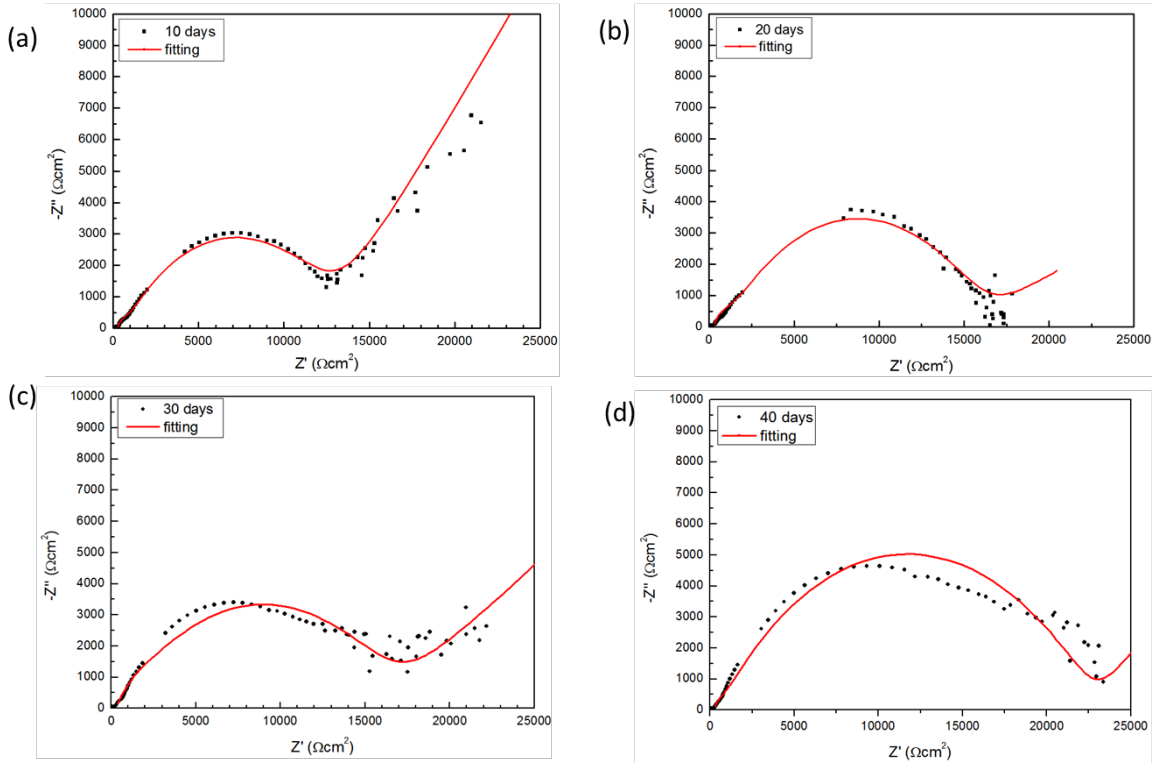

Figure 4-3 Nyquist plots and fitted plots of in situ EIS for oxidized Zr-Nb-Sn specimen for (a) 10, (b) 20, (c) 30, and (d) 40 days at 2.49 mg/kg DH condition

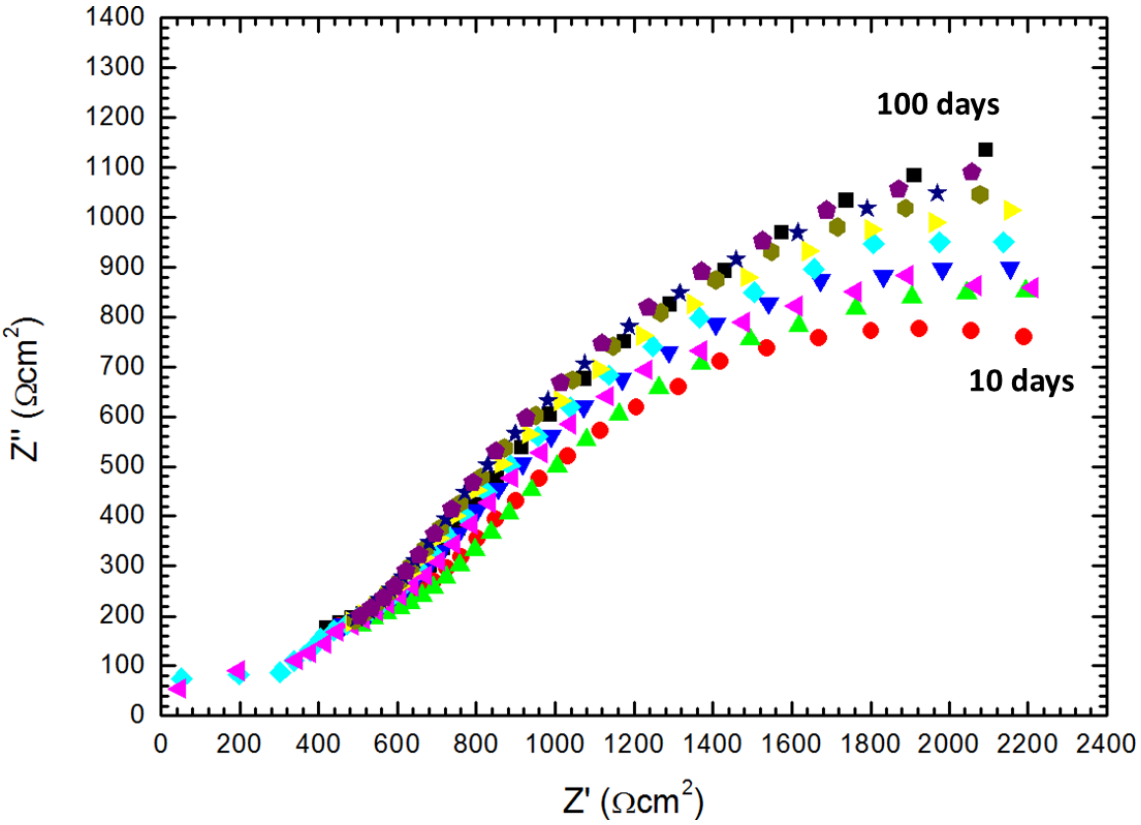

Figure 4-4 Nyquist plots of in situ EIS for oxidized Zr-Nb-Sn specimen for 100 days at 4.15 mg/kg DH condition

Table 4-3 Parameter values after optimization on the experimental impedance data for zirconium oxide at 2.49 mg/kg DH condition

	C_{in} (F/cm^2)	C_{out} (F/cm^2)	$R_{solution}$ (Ω)	R_{out} (Ω)	R_{in} (Ω)	**Inner oxide thickness**	**Outer oxide thickness**
10 d	$6X10^{-6}$	$1.7X10^{-7}$	250	375	11500	**19.5 nm**	**687 nm**
20 d	$5.8X10^{-6}$	$1.5X10^{-7}$		375	14000	**20.0 nm**	**753 nm**
30 d	$5.5X10^{-6}$	$1.2X10^{-7}$		380	15000	**21.2 nm**	**958 nm**
40 d	$5.5X10^{-6}$	$1.1X10^{-7}$		385	22000	**21.2 nm**	**1062 nm**

Table 4-4 Parameter values after optimization on the experimental impedance data for zirconium oxide at 4.15 mg/kg DH concentration

	C_{in} (F/cm^2)	C_{out} (F/cm^2)	$R_{solution}$ (Ω)	R_{out} (Ω)	R_{in} (Ω)	**Inner oxide thickness**	**Outer oxide thickness**
10 d	2.1X10^{-6}	1.3X10^{-7}	325	600	9000	**55.6 nm**	**898 nm**
20 d	2.0X10^{-6}	1.4X10^{-7}		450	7500	**58.4 nm**	**834 nm**
30 d	2.0X10^{-6}	1.1X10^{-7}		470	7400	**58.4 nm**	**1062 nm**
40 d	2.0X10^{-6}	1.1X10^{-7}		500	7400	**58.4 nm**	**1062 nm**
50 d	1.9X10^{-6}	8.0X10^{-8}		800	7500	**61.5 nm**	**1460 nm**
60 d	1.9X10^{-6}	8.0X10^{-8}		780	8700	**61.5 nm**	**1460 nm**
70 d	1.9X10^{-6}	7.8X10^{-8}		1500	7600	**61.5 nm**	**1498 nm**
80 d	1.4X10^{-6}	6.1X10^{-8}		1600	7700	**83.4 nm**	**1915 nm**
90 d	1.2X10^{-6}	5.9X10^{-8}		1600	7700	**97.4 nm**	**1980 nm**
100 d	1.0X10^{-6}	5.5X10^{-8}		1600	7700	**116.8 nm**	**2124 nm**

4.1.4 Ex-situ characteristic of zirconium oxide after high temperature water corrosion

The microstructural characterization of the zirconium oxide layer was conducted via TEM, EDS, and Fast Fourier transform (FFT) analysis after removing oxidized Zr-Nb-Sn alloy from the autoclave. Before TEM analysis, the zirconium oxide layer was covered by platinum layer, for preventing impurities. Figure. 4-5 demonstrates the cross section TEM images of the oxidized Zr-Nb-Sn alloy at 2.49 mg/kg DH concentration, and Figs. 4-5(a), (b), (c), and (d) represent the oxide layer of 30, 50, 80, and 100 d oxidations after start-up, respectively. The arrow marks to the right of each figure indicate the oxide growth direction, which indicate the inward direction. Also, the zirconium oxide and the second phase particles' chemical compositions are investigated via EDS. The point 1 in Fig. 4-5(a) comprised 15.8 wt. % O, 49.6 wt. % Zr, and 34.7 wt. % Nb. Alternatively, point 2 and 3, located within the zirconium oxide, comprised 22.5 wt. % O, 76.9 wt. % Zr, 0.6 wt. % Nb, and 0.1 wt. % Sn. The detail illustration about the chemical composition of different points are shown in Table. 4-5. Therefore, it can be concluded that Nb-enriched precipitates were formed in the oxide. Previous studies showed similar results, the fine β-niobium precipitate was found in niobium-containing Zr alloy after oxidation in aqueous solution [20,64].

The TEM images were analyzed to calculate the oxide layer thickness for different oxidation times. The oxide thickness was measured for 10 times for each image, and the average values are used for the oxide layer thickness. The oxide thickness after 30, 50, 80, and 100 d from start-up are presented in Table. 4-6. After 30 d oxidation at 2.49 mg/kg DH, the oxide thickness is 0.86 μm, and it increases to 1.46, 1.83, and 2.04 μm, as exposure time increases to 100 d

Also, the FFT analysis was conducted in several regions of zirconium oxide after 30 and 100 d, including various position of oxide layers and O/M interface. In Fig. 4-6(a) and (b), diffraction patterns were obtained at positions A, B, and C marked as red boxes, which represent the top, middle, and O/M interface, respectively. The d-spacings of positions A, B and C were determined using JCPDS diffraction reference data (37-1484, 42-1164, 50-1087; zirconium oxide). In both 30 and 100 d oxidation cases, the O/M region shows the tetragonal phase, and the top and middle oxide layers reveal the monoclinic zirconium oxide. This result is similar to the previous studies, the tetragonal zirconium oxide is dominant at O/M interface, however the monoclinic zirconium oxide becomes dominant as far from the O/M interface [17,65]. These results are well matched with the in-situ Raman spectroscopy results, which reveal that the phase of zirconium oxide can differ due to the position of the phase in the oxide layer.

Figure 4-7 demonstrates the TEM images of the oxidized Zr-Nb-Sn alloy at high DH, and Fig.

4-7(a), (b), (c), and (d) represent the oxide of 30 d to 100 d oxidations after start-up, respectively. Like normal DH case, the precipitates are found near the O/M interface, and the cracks are also found near the O/M interface. Table. 4-6 illustrates the oxide thickness at high DH. After 30 d oxidation, the oxide thickness is 1.12 μm, and it increases to 1.62, 1.97, and 2.15 μm, as exposure time increases to 100 d. In all time scales, the oxide thickness is thicker at 4.15 mg/kg than 2.49 mg/kg DH. Therefore, it revealed that the corrosion rate is faster than high DH level than the normal DH. The difference of oxidation rate is due to the DH, and the detail discussion is treated discussion section.

Fast Fourier Transform (FFT) analysis was also conducted in TEM images after 30 and 100 d oxidation at high DH, including various positions of zirconium oxide. In Fig. 4-8(a) and (b), the red boxes as ‘A’, ‘B’, and ‘C’ are investigated via FFT analysis. The results also indicate that the O/M interface presents the tetragonal dominant, and as far from the O/M interface, the monoclinic phase appears, and it becomes dominant.

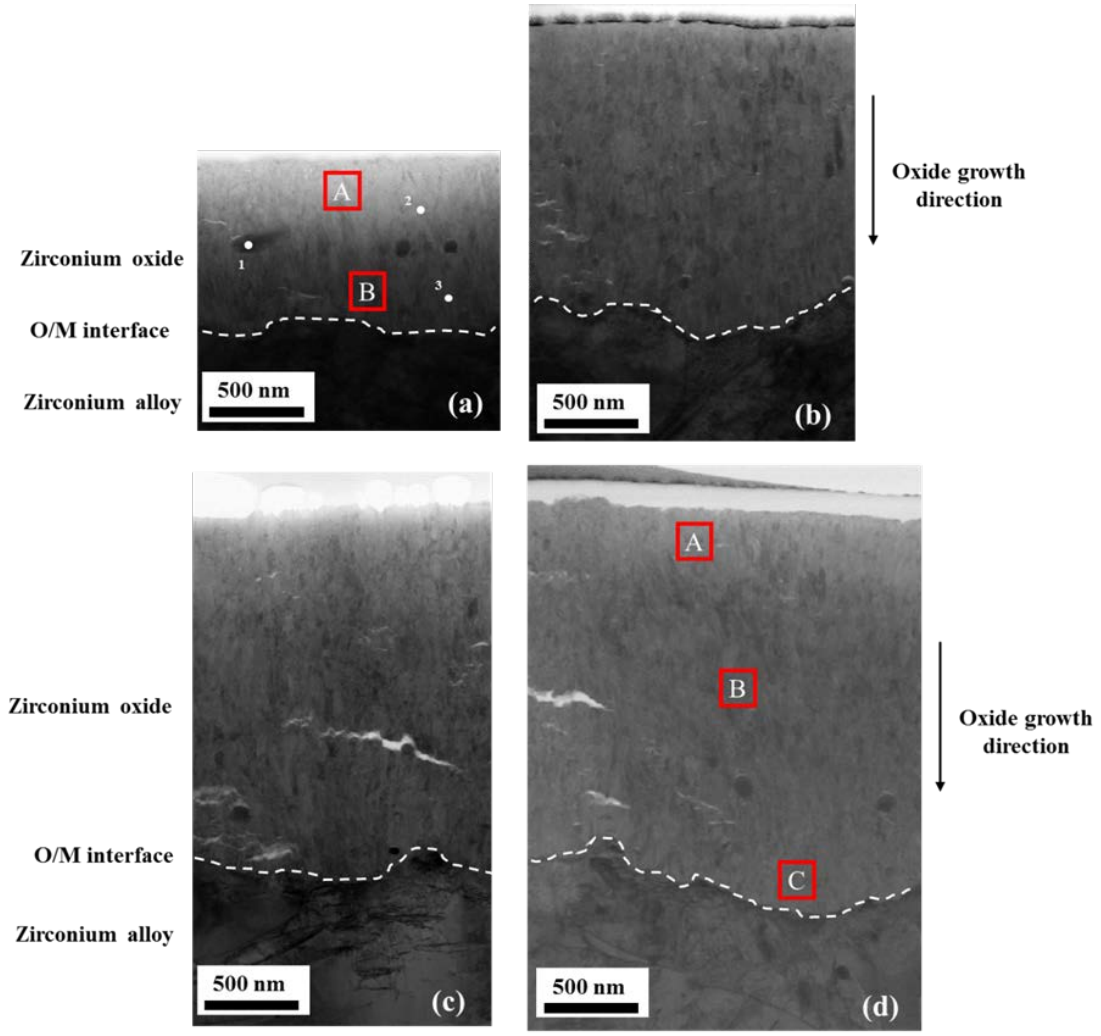

Figure 4-5 TEM images the oxide film on the Zr–Nb–Sn specimen after (a) 30 d, (b) 50 d, (c) 80 d, and (d) 100 d at 2.49 mg/kg of DH. The red boxes “A”, “B”, and “C” were used for Fast Fourier Transform analysis.[61]

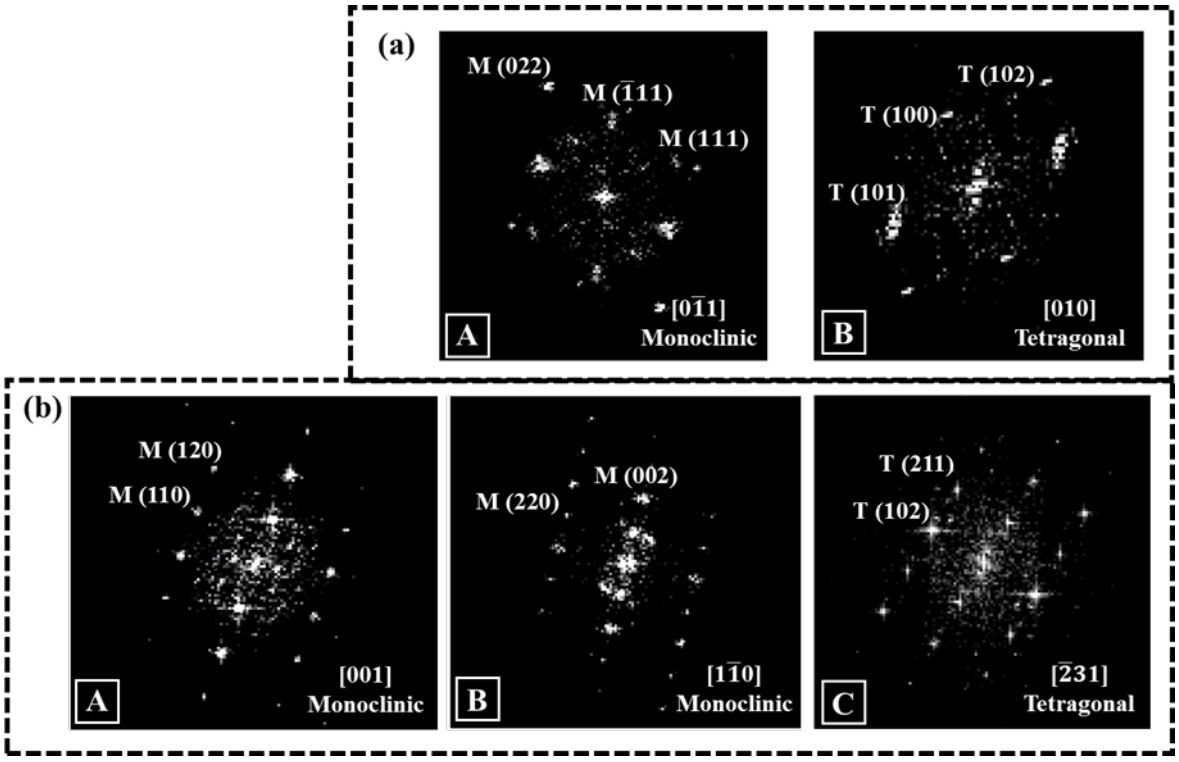

Figure 4-6 Fast Fourier Transform analysis images of the oxidized Zr–Nb–Sn alloy after (a) 30 d, and (b) 100 d at 2.49 g/kg DH [61]

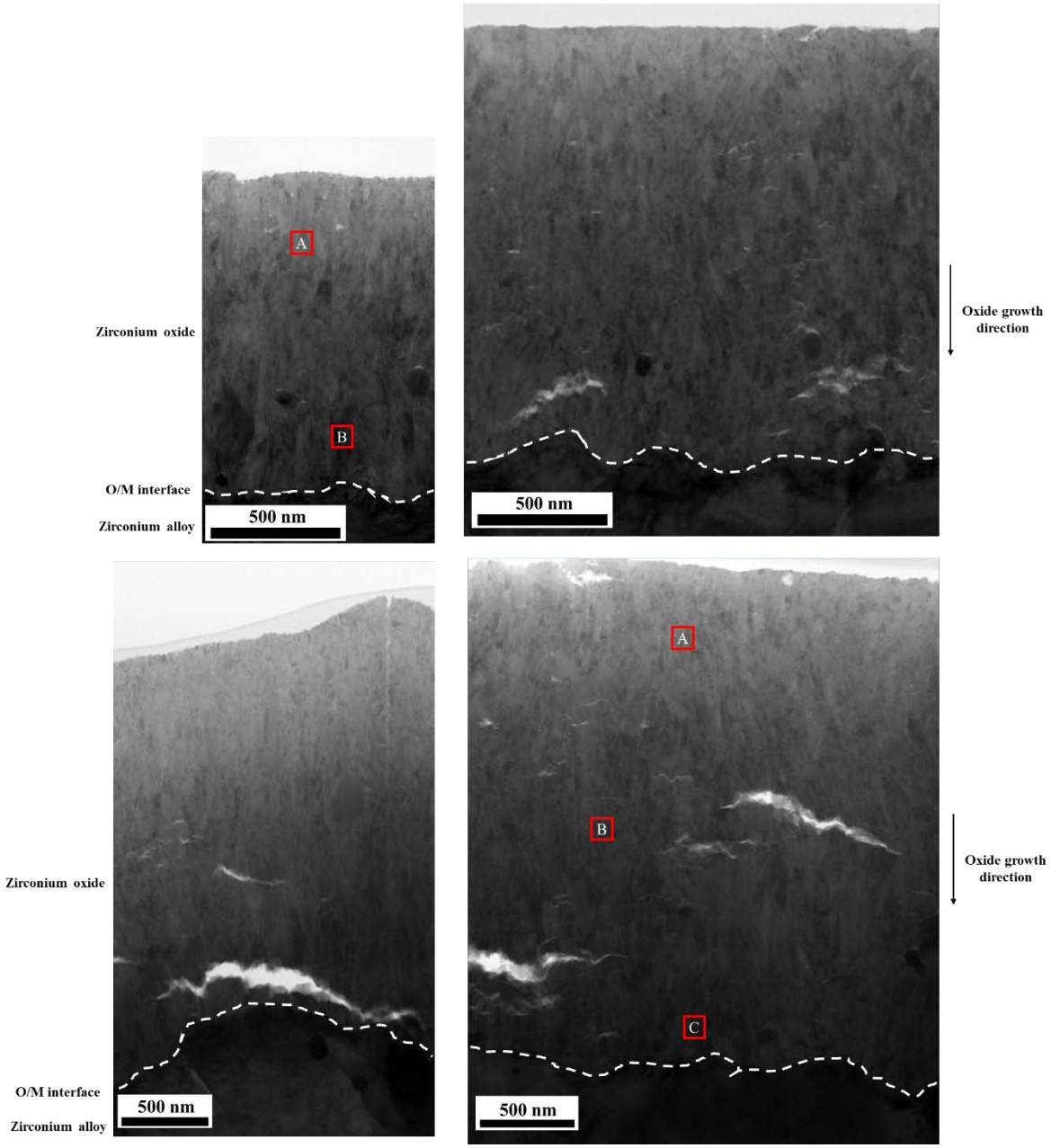

Figure 4-7 TEM images the oxide film on the Zr–Nb–Sn specimen after (a) 30 d, (b) 50 d, (c) 80 d, and (d) 100 d at 4.15 mg/kg of DH. The red boxes “A”, “B”, and “C” were used for Fast Fourier Transform analysis. [61]

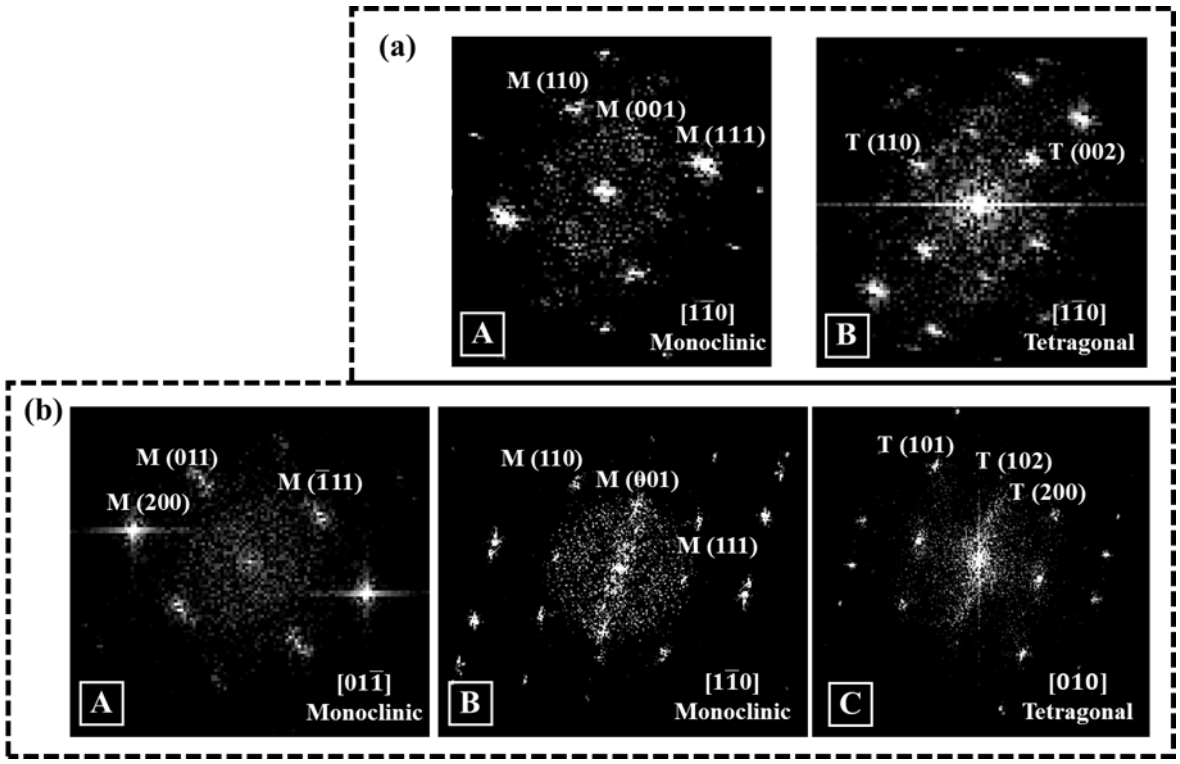

Figure 4-8 Fast Fourier Transform analysis images of the oxidized Zr–Nb–Sn alloy after (a) 30 d, and (b) 100 d at 4.15 mg/kg DH. [61]

Table 4-5 Chemical composition of 3 different points in Fig. 4-5 (a).

Weight percent (wt. %)	O	Zr	Nb	Sn
Point 1	15.75	49.55	34.70	-
Point 2	22.52	76.87	0.55	0.06
Point 3	24.44	74.62	0.86	0.08

Table 4-6 The average values of zirconium oxide thickness with standard deviations of 30, 50, 80, and 100 d from start-up at different DH concentrations

Oxidation time	2.49 mg/kg DH	4.15 mg/kg DH
30 d	0.862 ± 0.011 μm	1.124 ± 0.017 μm
50 d	1.466 ± 0.019 μm	1.620 ± 0.010 μm
80 d	1.834 ± 0.017 μm	1.972 ± 0.037 μm
100 d	2.047 ± 0.057 μm	2.152 ± 0.021 μm

4.2 Scanning transmission X-ray microscopy results

4.2.1 Scanning transmission X-ray microscopy results at normal DH condition

The STXM results of oxidized zirconium alloy with different oxidation time are illustrated in Fig. 4-9. Figure 4-9 shows the STXM images of oxidized zirconium alloy cross-section from FIB sampling after different oxidation time at 2.49 mg/kg condition, respectively. All STXM images show the dark-contrast region which existed just above the oxide/metal (O/M) interface. For investigating the characteristic of dark-contrast region, the X-ray absorption spectroscopy of O K-edge energy region was conducted.

When obtaining the O K-edge XAS spectra in Figs. 4-10, 4-11, 4-12, and 4-13, the O/M interface is assumed just above the metal layer, and the interface is dark area in the 534 eV image in Fig. 4-9. From the all STXM image, the O/M interface layer (sub-oxide layer) thickness is below 100 nm. The obvious twin peaks are observed in the XAS spectrum of zirconium oxide. The twin-peak structure of the O K-edge means the t_{2g} and e_g orbital of the oxygen are shown in the XAS image. In the electronic structure of ZrO_2 the lowest unoccupied molecular orbitals will be associated with the empty 4d orbitals of the Zr atoms. Because of electron-electron interactions, the latter pair, labeled e_g, are lowered in energy while the former group, labeled t_{2g}, are raised in energy. The e_g orbital points toward the interstitial sites of zirconium oxide between the two oxygen atoms, hence is “nonbonding,” while t_{2g} orbital is “bonding” [66]. The 1st peak (～532 eV) related to the excitation from the O 1s state to the hybridized O 2p− Zr 3d state, and the 2nd (～536 eV) and 3rd peaks (～541 eV) are related to the excitations of O 1s to O 2p−Zr 5d, and O 2p−Zr 4sp, respectively.

All STXM images show the dark-contrast region just above the O/M interface, and thickness of that region is around 50 to 100 nm. This indicates that the oxygen chemistry is different compared to the bulk zirconium oxide. The sharp e_g and t_{2g} orbitals peaks related to the Zr 4d and O 2p hybridization disappear in the sub-oxide region. The peak separation between two peaks e_g and t_{2g} decreases from the sub-oxide region to the bulk zirconium oxide.

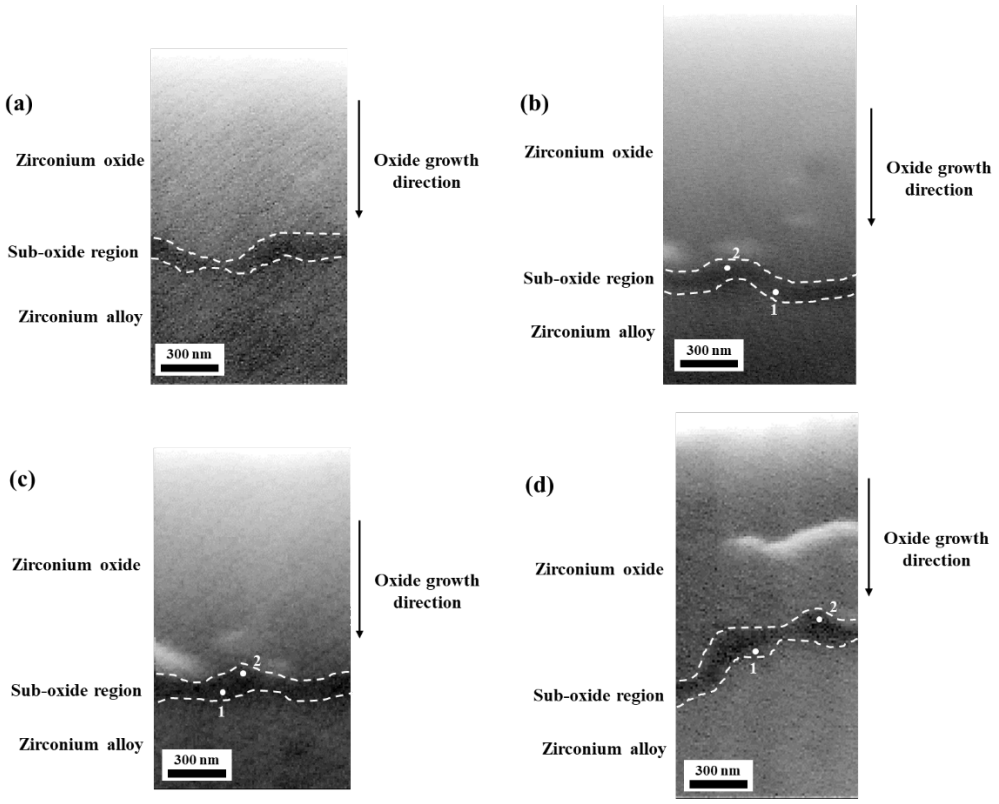

Figure 4-9 STXM images of oxidized zirconium alloy for (a) 30 d, (b) 50 d, (c) 80 d, and (d) 100 d at 2.49 mg/kg DH

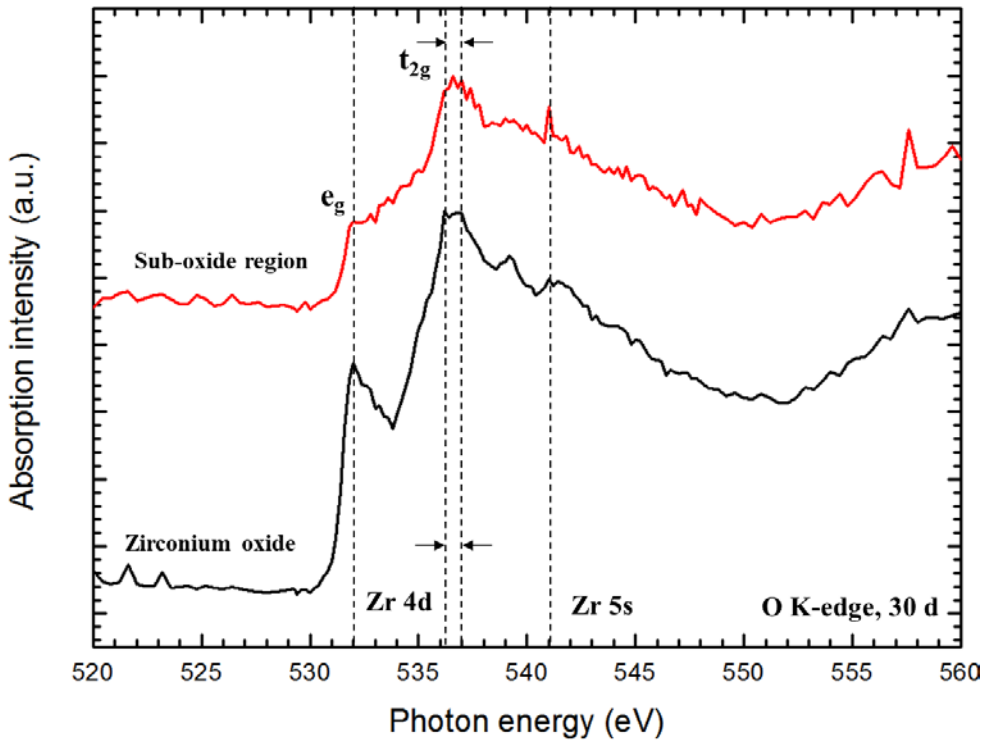

Figure 4-10 O K-edge XAS image of oxidized zirconium alloy for 30 d at 2.49 mg/kg DH

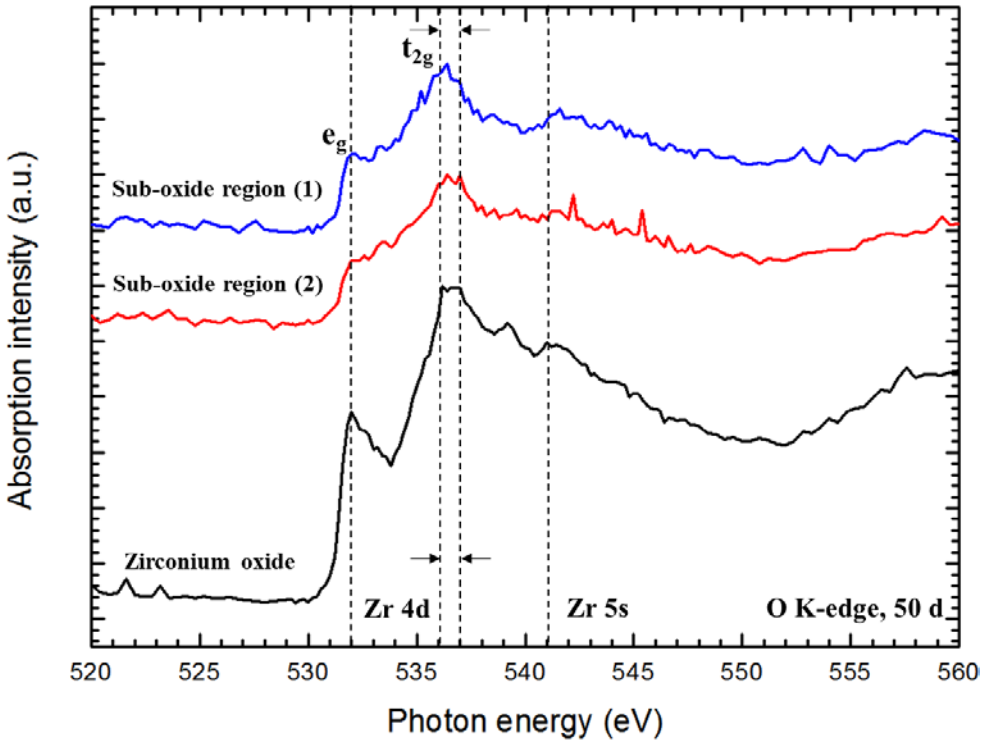

Figure 4-11 O K-edge XAS image of oxidized zirconium alloy for 50 d at 2.49 mg/kg DH

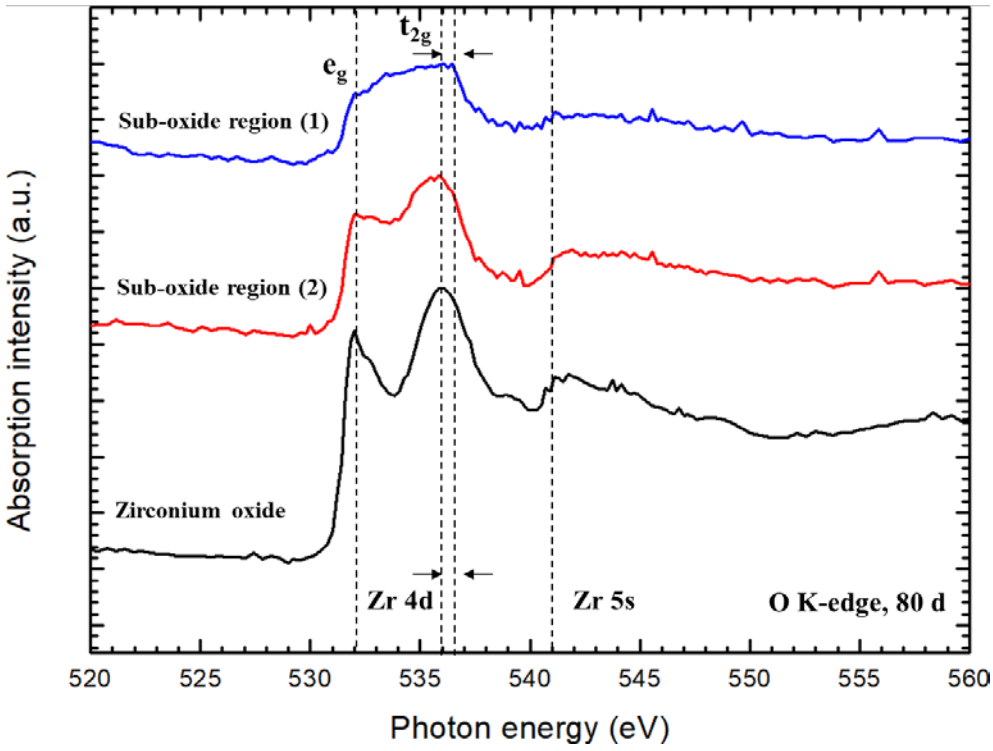

Figure 4-12 O K-edge XAS image of oxidized zirconium alloy for 80 d at 2.49 mg/kg DH

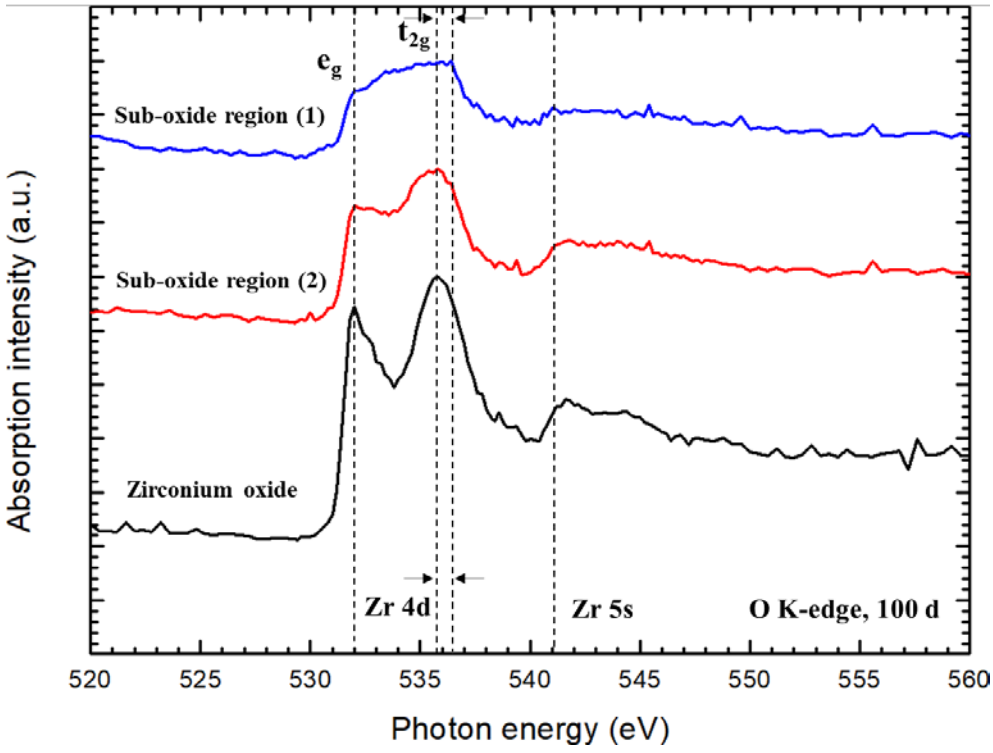

Figure 4-13 O K-edge XAS image of oxidized zirconium alloy for 100 d at 2.49 mg/kg DH

4.2.2 Scanning transmission X-ray microscopy results at high DH condition

The STXM results of oxidized zirconium alloy with different oxidation time are illustrated in Fig. 4-14. Figure 4-14 shows the STXM images of oxidized zirconium alloy cross-section from FIB sampling after different oxidation time at 4.15 mg/kg condition, respectively. As similar as the previous case, all STXM images show the dark-contrast region which existed just above the O/M interface. For investigating the characteristic of dark-contrast region, the X-ray absorption spectroscopy of O K-edge energy region was also conducted.

As shown in Fig. 4-14, the sub-oxide layer is observed just above the zirconium matrix layer, and the sub-oxide layer is dark area in the 534 eV image. From Figs. 4-15, 4-16, 4-17, and 4-18, the O K-edge XAS spectra was obtained, and the electronic structure was investigated with analyzing the peak separation of e_g and t_{2g} peaks. Similar to the previous case, all STXM images show that the sub-oxide layer thickness is below 100 nm, and the obvious twin peaks are observed in the XAS spectrum of zirconium oxide. The twin-peak structure of the O K-edge means the t_{2g} and e_g orbital of the oxygen are shown in the XAS images. In the bulk zirconium oxide region, the peak position of e_g is 532 eV, and it of t_{2g} is around 535.5 eV. In the sub-oxide region, the peak position of e_g is same with the bulk zirconium oxide region, 532 eV, however, the t_{2g} peak position is changed to 536.2 eV. These results indicate that the peak separation between two peaks e_g and t_{2g} decreases from the sub-oxide region to the bulk zirconium oxide.

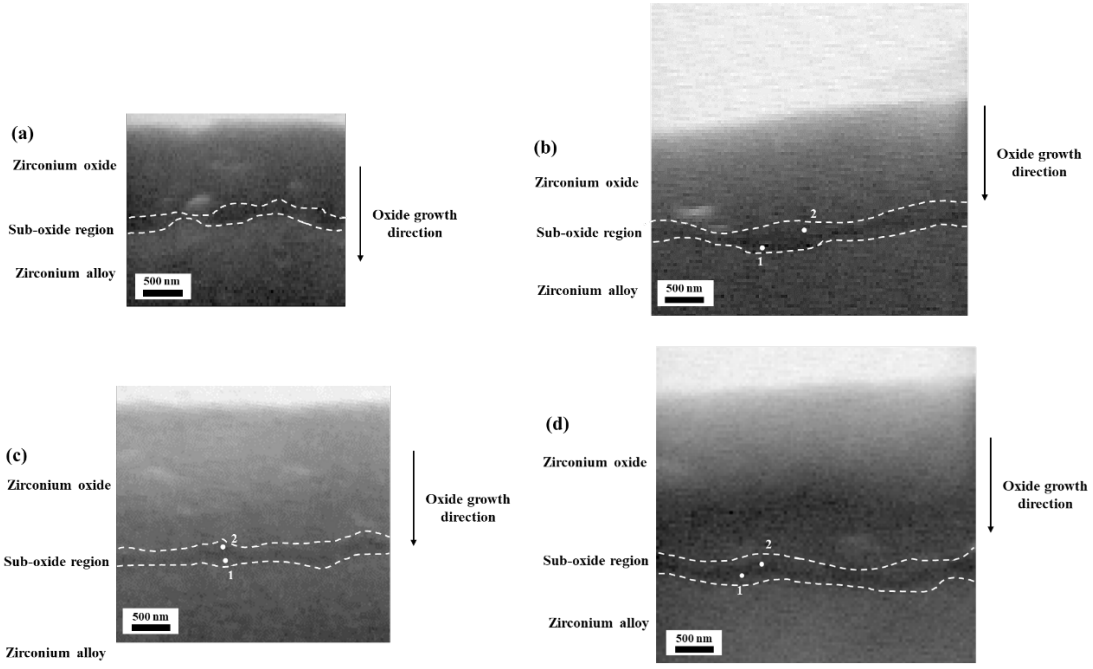

Figure 4-14 STXM images of oxidized zirconium alloy for (a) 30 d, (b) 50 d, (c) 80 d, and (d) 100 d at 4.15 mg/kg DH

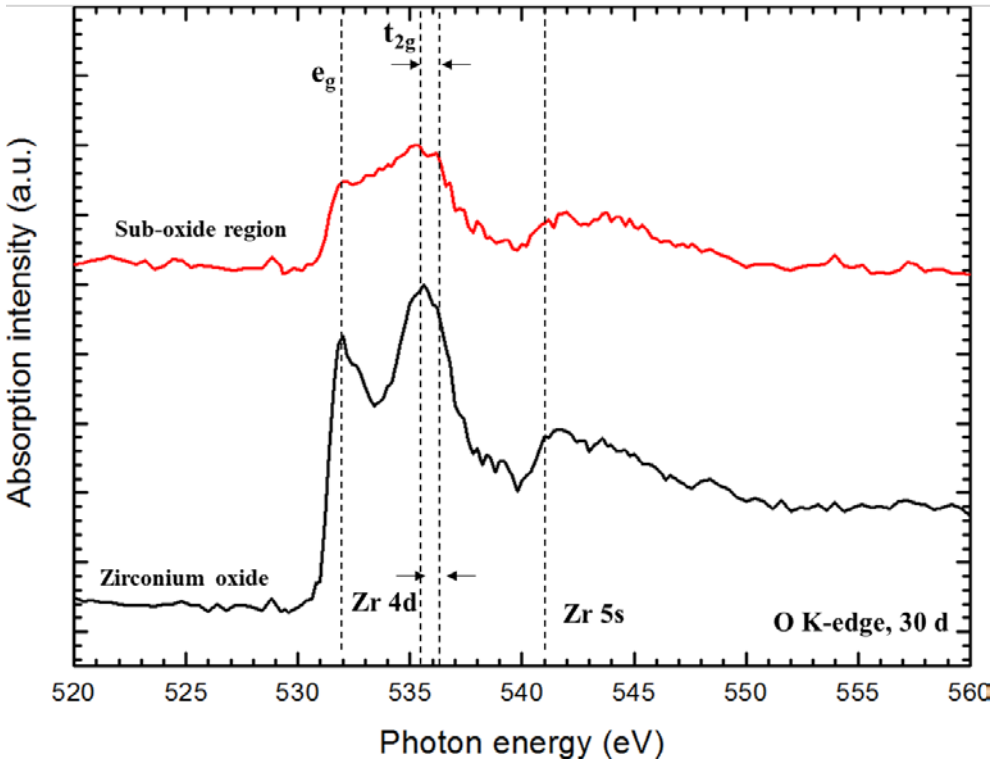

Figure 4-15 O K-edge XAS image of oxidized zirconium alloy for 30 d at 4.15 mg/kg DH

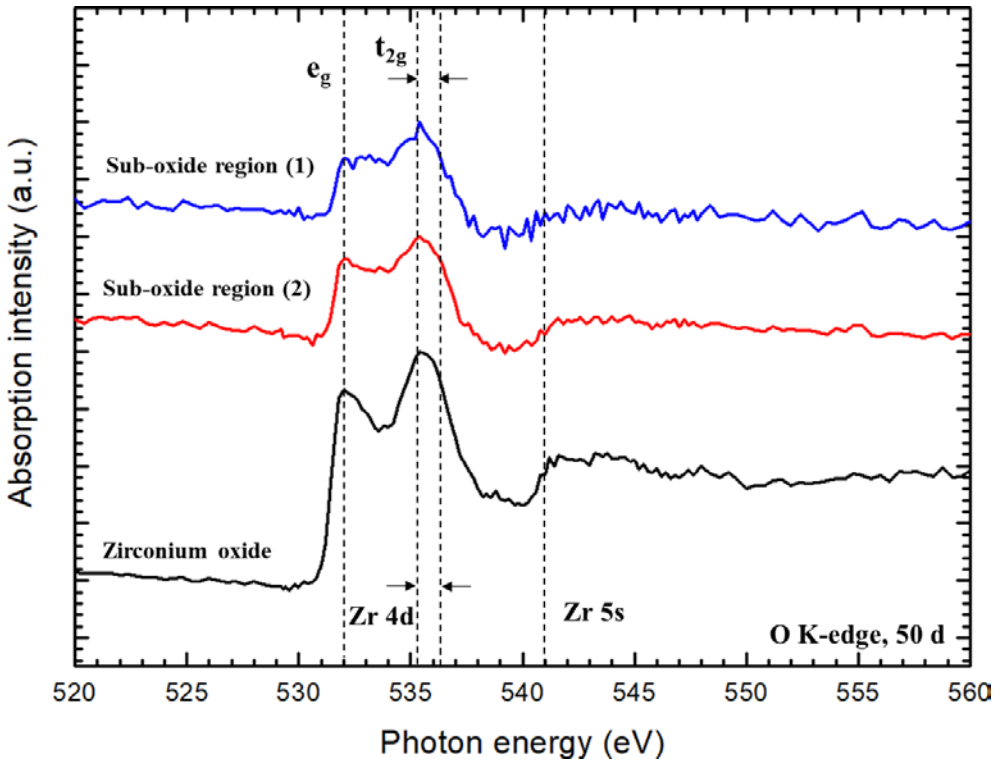

Figure 4-16 O K-edge XAS image of oxidized zirconium alloy for 50 d at 4.15 mg/kg DH

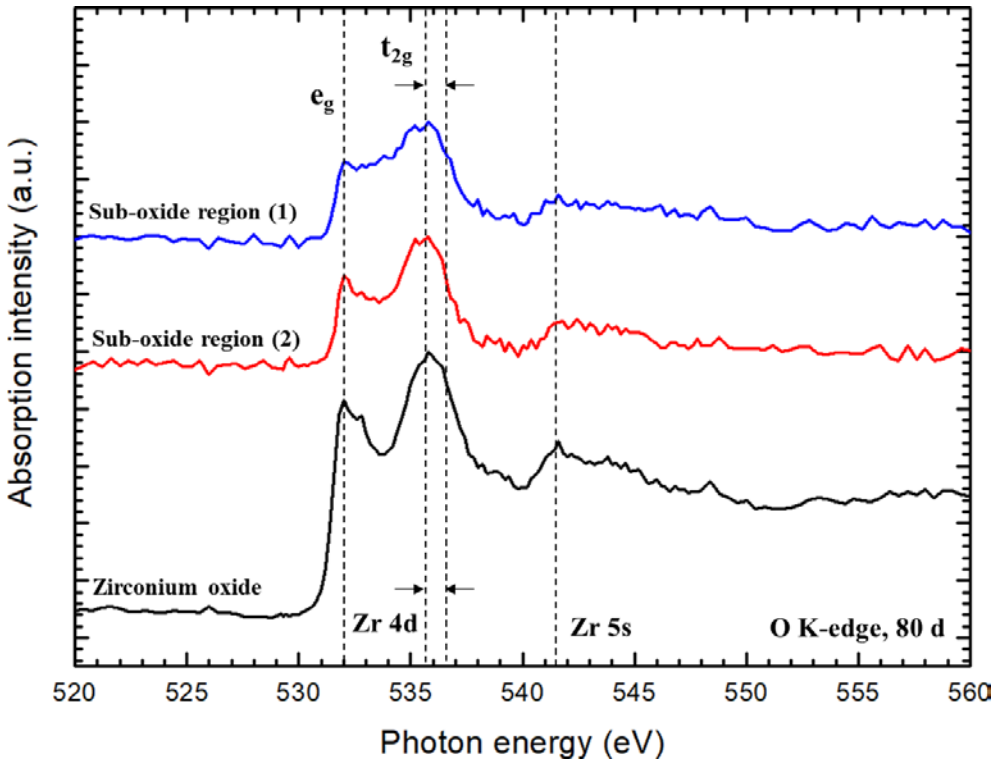

Figure 4-17 O K-edge XAS image of oxidized zirconium alloy for 80 d at 4.15 mg/kg DH

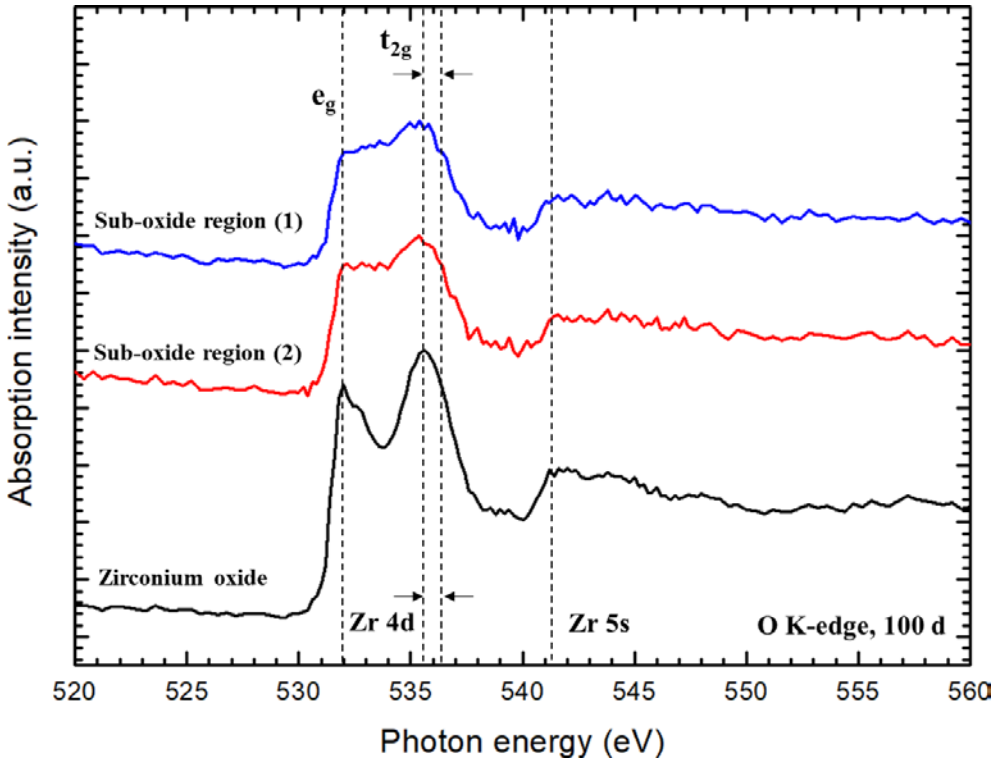

Figure 4-18 O K-edge XAS image of oxidized zirconium alloy for 100 d at 4.15 mg/kg DH

4.3 X-ray reflectivity results

4.3.1 X-ray reflectivity results at ambient condition (room temperature, atmospheric pressure)

The measured XRR intensity data was 1-D integrated for increasing signal-to-noise ratio and the decreasing background effect. Figure 4-19 shows the captured image of the 1-D XRR intensity peak analysis program developed in high pressure collaborative access team, geophysical laboratory of Carnegie Institution of Washington. The yellow box in the image indicates that the region of interest of XRR measurement. Also, the green box in the image means the region of background noise extraction. Therefore, the intensity-Q curves can be obtained from the obtained XRR data.

Figure 4-20 shows the XRR integrated intensity as a function of momentum transfer, Q for YSZ (111) at room temperature, where Q is illustrated in equation 2-3.

$$\mathrm{Q} = |\boldsymbol{Q}| = \frac{4\pi}{\lambda}\sin(\theta) \tag{2-3}$$

For investigating the electron density profile of YSZ (111) at two different conditions, the fitting process should be followed for calculating the parameters including the electron occupancy, atom position, distribution width, etc. The measured reflectivity data could be re-analyzed with using structure factor model, which is the summation of F value of unit cell CTR, relaxed layer, adsorbed layer, and water layer. Equation 4-1 and Fig. 4-21 present the structure factor model of YSZ (111) in this thesis.

$$\begin{aligned} \mathrm{F}_{total} = F_{uc} * F_{ctr} + F_{relax1} + F_{relax2} + F_{relax3} + F_{relax4} \\ + F_{adsorbed1} + F_{adsorbed2} + F_{water} \end{aligned} \tag{4-1}$$

$$\mathrm{I}_{\mathrm{total}} \propto |F_{total}|^2 \tag{4-2}$$

In equation 4-1, $F_{uc} * F_{ctr}$ is related to the semi-infinite single crystal structure factor, and F_{relax} is related to the relaxation layers of top layers of the YSZ (111) substrates. And, the $F_{adsorbed}$ corresponds to the adsorbed ions layer on the YSZ substrates, and the F_{water} is related to the bulk water with semi-infinite structure.

To obtain the profiles of electron density along the surface normal direction, the nonlinear least squares fitting analysis should be conducted for deriving the atomic scale structures of YSZ (111) and water interface. Non-linear least square is the form of least squares analysis used to fit a set of ‘m’ numbers observations with a model that is non-linear in ‘n’ numbers unknown parameters (m > n). Consider a set of m data points, (x_1, y_1), … (x_m, y_m), a curve model function y = f(x, v), and a set of

parameters for variable x depends on parameters. $\mathbf{v} = (v_1, v_2, \ldots, v_n)$. The sum of squares S is shown in the equation 4-3 [67].

$$S = \sum_{i=1}^{m} r_i^2 \tag{4-3}$$

For minimizing the sum of squares, there is some methods in previous study, and in this thesis, the Levenberg-Marquardt method is adopted.

In the fitting model, total 19 parameters with including electron occupancy, atom position, distribution width are used. In Fig. 4-21, the top layer of the model consists of bulk water layer, and the parameters for bulk water layer is the position and displacement. The next layer consists of two adsorbed layers, and the parameters for these layers are electron occupancy, distribution width, and the atomic position. Then, the relaxed layer is following, and the top layer termination oxygen atom position is set as zero. The four layers for the top layers of YSZ (111) are set as the relaxed layers in this fitting model. Finally, the semi-infinite unit cell of YSZ (111) is used for the substrate layer, with specific unit cell lattice constant.

The best fitted results for the XRR data is presented in Fig. 4-22, and this fitted results (red-line) represent the measured data very well. The reduced χ^2 value for the non-linear square fitting is 1.430 with 19 variables and 77 data points. Based on the best fitted parameters, the electron density profiles along the surface normal direction are calculated and they are shown in Fig. 4-23. The fitting parameters and their values from the fitting model are presented in Table. 4-7. The depletion of metal at top surface of YSZ (111) is 43.5 % and it reduces to 8 and 2.1 % at 2nd and 3rd unit cell layers. On the other hand, the lattice constant variations of the unit cells under the top unit cell are negligible. The variation of lattice constant is less than 0.02 Å.

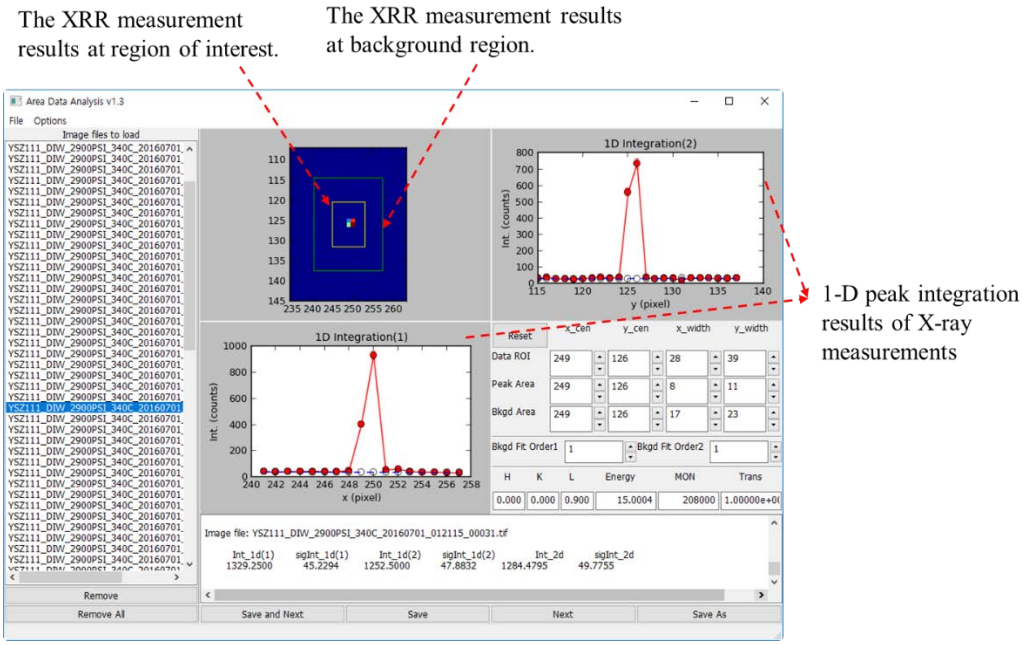

Figure 4-19 Captured image of peak integration program for XRR data analysis

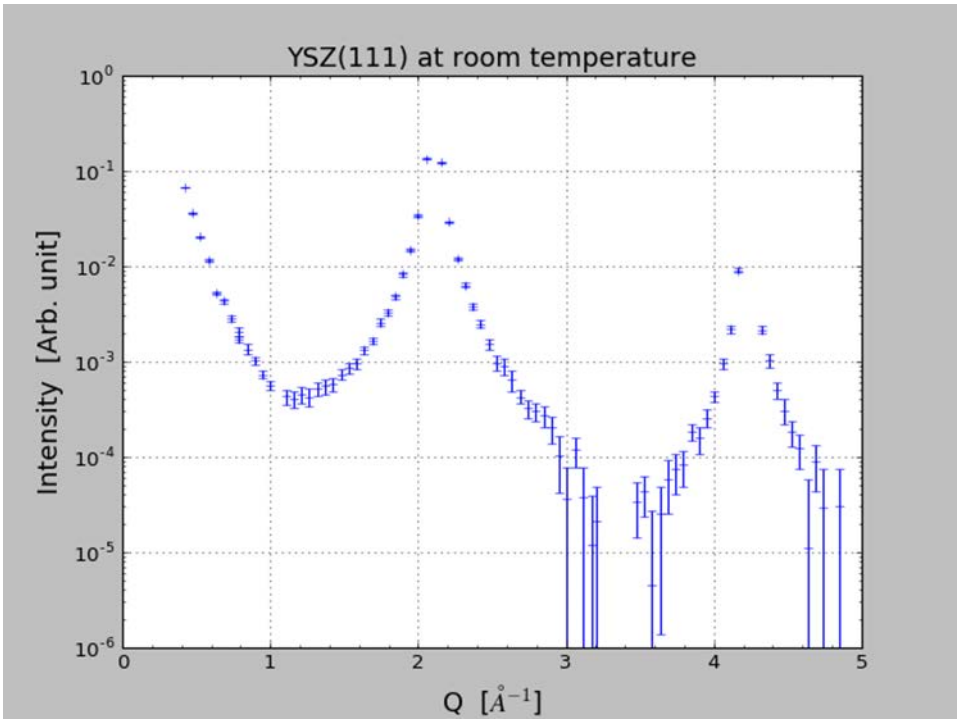

Figure 4-20 Measured X-ray reflectivity data (with error bars) for YSZ (111) and water interface as a function of Q at room temperature

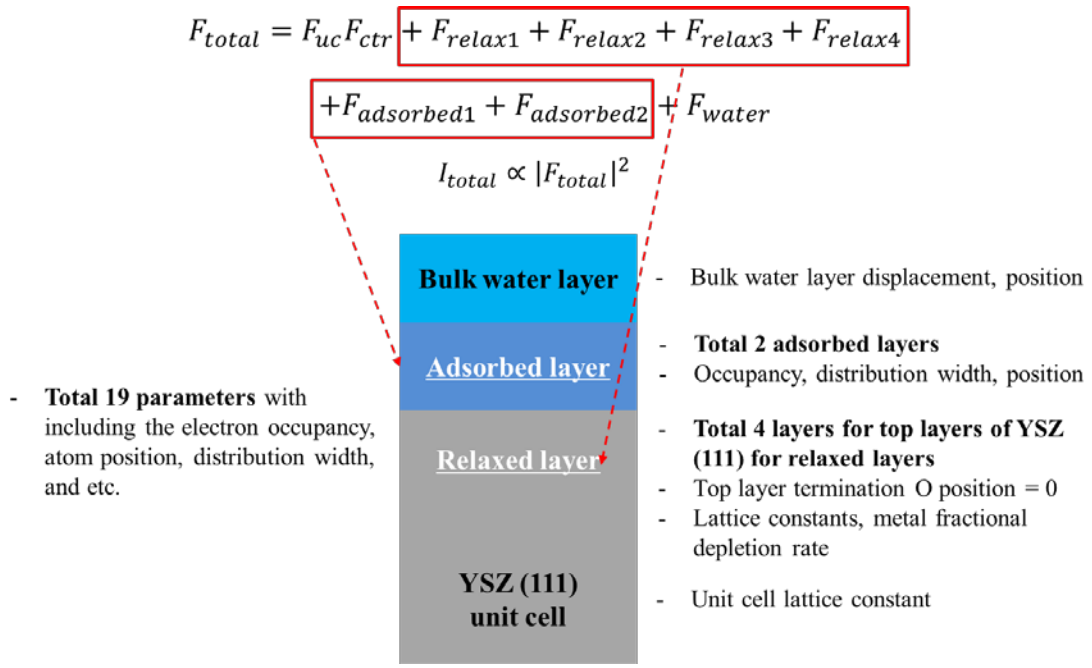

Figure 4-21 A schematic of fitting model for YSZ (111) and water interface

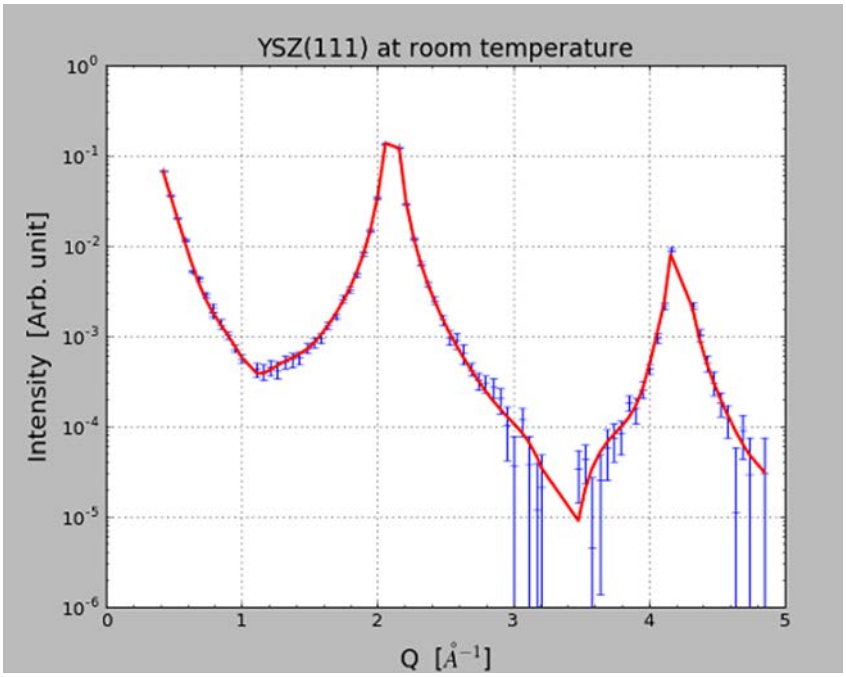

Figure 4-22 Measured XRR data (blue line + error bars) and the fitting results (red line) for YSZ (111) and water interface at room temperature as a function of Q

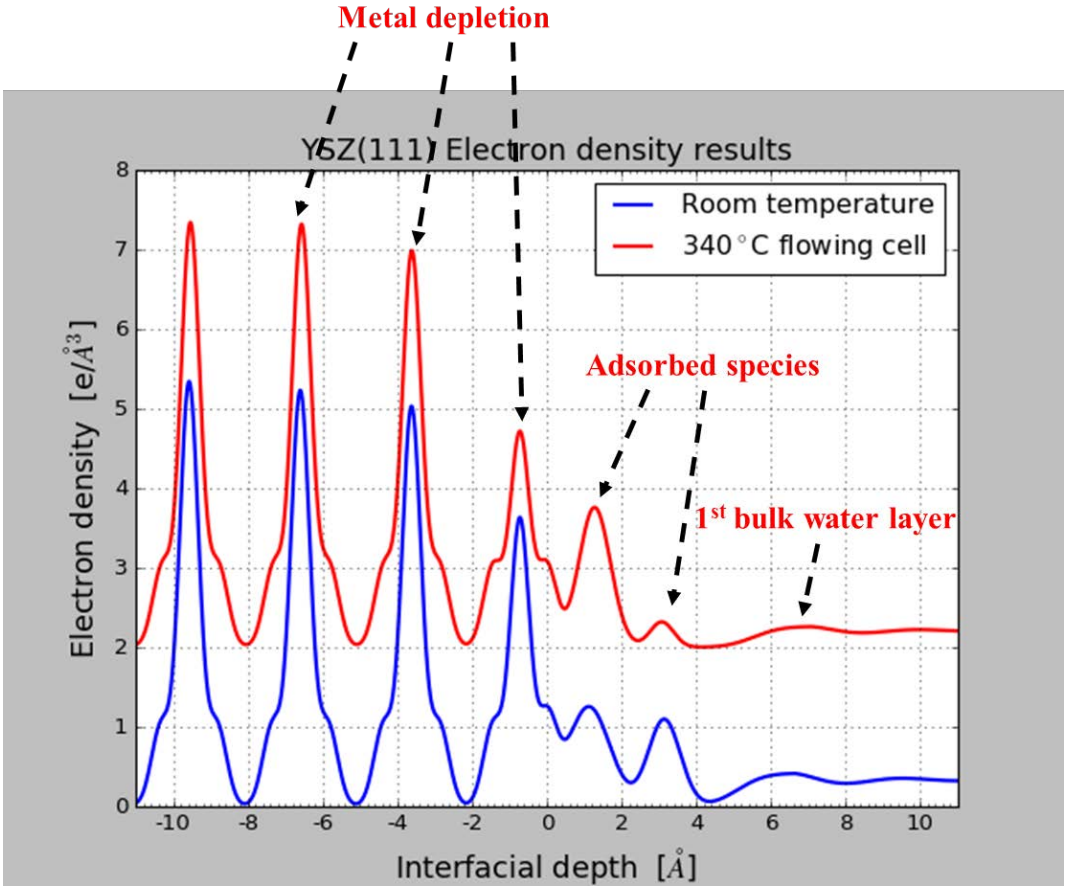

Figure 4-23 Electron density profiles from the fitting results of the XRR data for YSZ (111) and water interface (blue line) room temperature (red line) 340 ℃ flowing cell condition

Table 4-7 Best-Fitted parameters from the YSZ (111) and water interface fitting model for room temperature

Parameters (unit)	Best-fit results with errors
1st adsorbed layer occupancy	1.825 ± 0.049
1st adsorbed layer position distribution width (Å)	0.348 ± 0.02
1st adsorbed layer position (Å)	1.279 ± 0.034
2nd adsorbed layer occupancy	1.416 ± 0.262
2nd adsorbed layer position distribution width (Å)	0.2 ± 0.017
2nd adsorbed layer position (Å)	3.076 ± 0.183
Top unit cell metal fractional depletion	0.662 ± 0.017
2nd unit cell metal fractional depletion	0.092 ± 0.013
3rd unit cell metal fractional depletion	0.004 ± 0.008
4th unit cell metal fractional depletion	Negligible
Top unit cell lattice constant (Å)	2.982 ± 0.007
2nd unit cell lattice constant (Å)	2.975 ± 0.006
3rd unit cell lattice constant (Å)	2.99 ± 0.004
4th unit cell lattice constant (Å)	2.968 ± 0.003
1st bulk water position (Å)	7.046 ± 0.038
1st bulk water layer displacement (Å)	0.2 ± 0.026
1st bulk water layer vibrational amplitude (Å)	0.251 ± 0.028
Surface roughness factor	0.142 ± 0.013
Scale factor	11514 ± 315

4.3.2 X-ray reflectivity results at high temperature water condition

Figure 4-24 shows the XRR integrated intensity as a function of momentum transfer, Q for YSZ (111) at 340 ℃ and 20 MPa flowing cell condition, where Q is illustrated in equation 2-3. Also, the parameters for fitting are calculated from the fitting model for YSZ (111) and water interface at 340 ℃ condition with the same model in previous case. Figure 4-25 illustrates the results of fitting for the measured XRR data. This results well reproduce the experimental data, and the reduced $\chi 2$ value for the non-linear square fitting is 1.883 with 19 variables and 77 data points. Based on the parameters from fitting, the electron density profiles along the surface normal direction are calculated and also shown in the red line in Fig. 4-23. The results show that the depletion of metal at top surface of YSZ (111) is 66.5 % and it reduces to 9.2 and 0.4 % at 2^{nd} and 3^{rd} unit cell layers. On the other hand, the lattice constant variations of the unit cells under the top unit cell are also negligible. The variations of lattice constant are less than 0.03 Å. The atomic structure change of YSZ (111) due to the high temperature water is discussed in the next chapter.

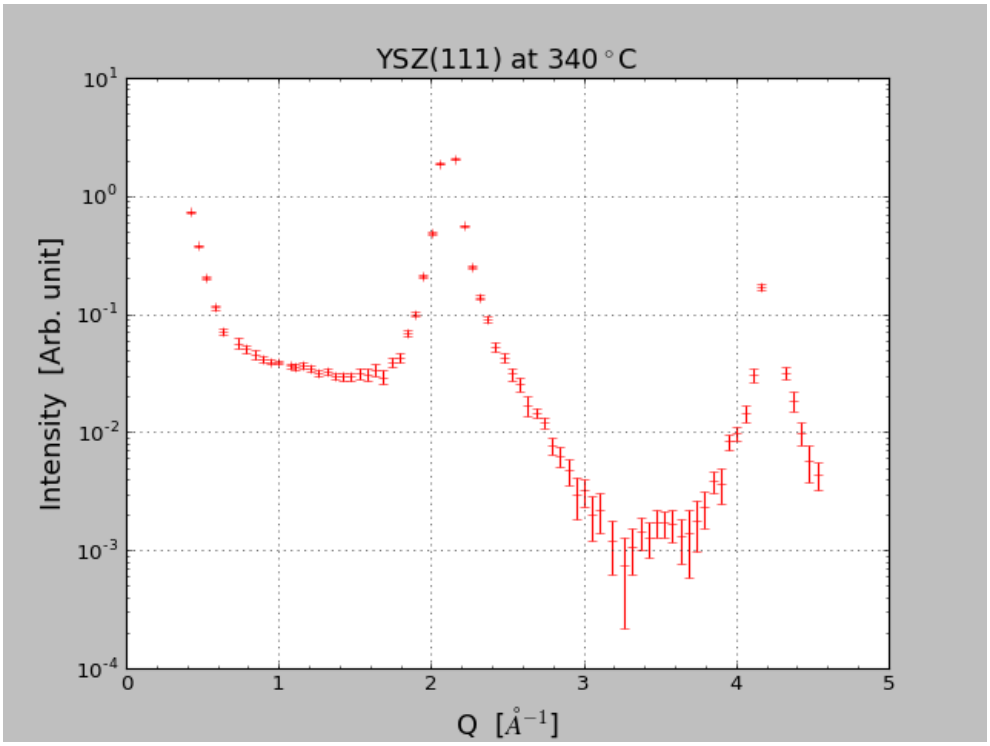

Figure 4-24 Measured XRR data (with error bars) for YSZ (111) and water interface as a function of Q at 340 ℃ water

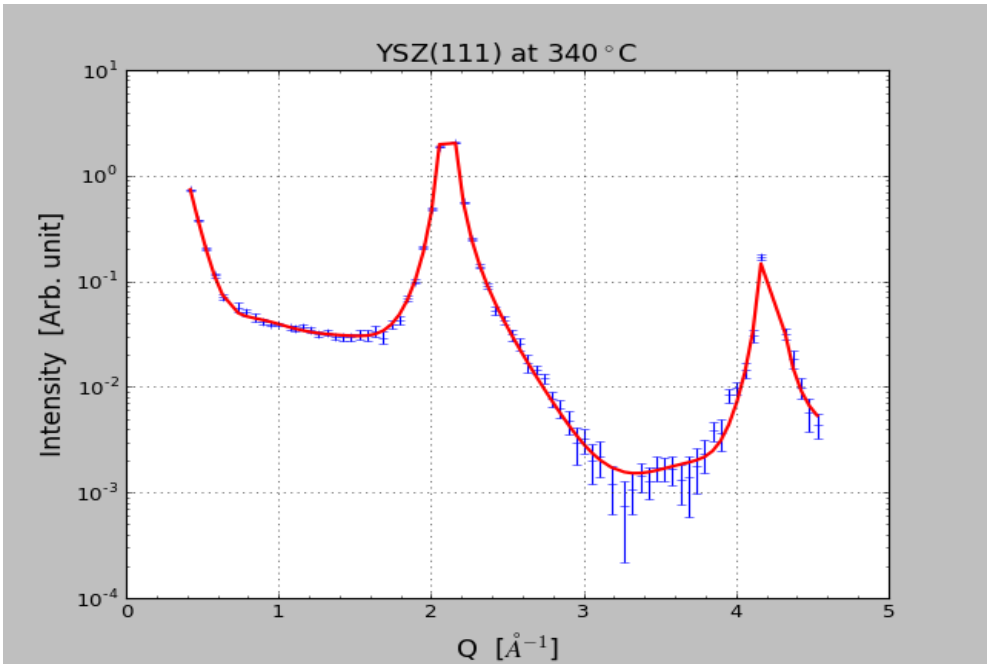

Figure 4-25 XRR data (blue line + error bars) and the fitting result (solid line) for YSZ (111) and water interface at 340 ℃ water as a function of Q

Table 4-8 Best-fitted parameters derived from the fitting model for YSZ (111) and water interface for 340 ℃

Parameters (unit)	Best-fit results with errors
1st adsorbed layer occupancy	1.825 ± 0.049
1st adsorbed layer position distribution width (Å)	0.348 ± 0.02
1st adsorbed layer position (Å)	1.279 ± 0.034
2nd adsorbed layer occupancy	1.416 ± 0.262
2nd adsorbed layer position distribution width (Å)	0.2 ± 0.017
2nd adsorbed layer position (Å)	3.076 ± 0.183
Top unit cell metal fractional depletion	0.662 ± 0.017
2nd unit cell metal fractional depletion	0.092 ± 0.013
3rd unit cell metal fractional depletion	0.004 ± 0.008
4th unit cell metal fractional depletion	Negligible
Top unit cell lattice constant (Å)	2.982 ± 0.007
2nd unit cell lattice constant (Å)	2.975 ± 0.006
3rd unit cell lattice constant (Å)	2.99 ± 0.004
4th unit cell lattice constant (Å)	2.968 ± 0.003
1st bulk water position (Å)	7.046 ± 0.038
1st bulk water layer displacement (Å)	0.2 ± 0.026
1st bulk water layer vibrational amplitude (Å)	0.251 ± 0.028
Surface roughness factor	0.142 ± 0.013
Scale factor	11514 ± 315

5. Discussion

5.1 Characteristic of O/M interface and phase transformation of zirconium oxide

In Figs. 4-5 and 4-7, the microstructures of zirconium oxide with different oxidation time and condition are presented. For investigating the corrosion rate difference between two different DH concentrations, the zirconium oxide thickness is compared in the Fig. 5-1. The oxide growth rate is faster in 4.15 mg/kg than it of 2.49 mg/kg. In high DH level, oxide thickness is thicker than 200 – 300 nm in all time scales than normal DH level. This means that the corrosion resistance of zirconium alloy in high DH is inferior. The previous studies reveal that the phase of zirconium oxide is highly related to the corrosion characteristic of zirconium alloy in high temperature water environment [68,69]. The volume fraction of tetragonal phase oxide decreased with an increasing exposure time in high temperature water, and this trend could be also confirmed via in situ Raman spectroscopy in this thesis. Fig. 5-2 represents the phase difference of zirconium oxide in 30 d with different DH concentration. In the black upper line which shows the in-situ Raman spectrum of normal DH concentration, and red line for high DH concentration. For peak identification, the region from 320 to 340 cm^{-1} is zoomed in, and these results show that the tetragonal zirconium oxide peaks at 332 cm^{-1} shows much stronger in normal DH concentration. Therefore, it can be concluded that the tetragonal zirconium oxide becomes unstable in high DH level, and the tetragonal phase to monoclinic oxide phase transformation is more activated in high DH condition.

From the STXM analysis, the dark-contrast region just above the O/M interface, and thickness of that region is around 50 to 100 nm. This indicates that the oxygen chemistry is different compared to the bulk zirconium oxide. The sharp e_g and t_{2g} orbitals peaks related to the Zr 4d and O 2p hybridization disappear in the sub-oxide region. Also, the peak separation between two peaks e_g and t_{2g} decreases from the sub-oxide region to the bulk zirconium oxide. In Table. 5-1, the values of peak position and separation at 2.49 mg/kg DH level are presented. It shows that the peak position of t_{2g} is different as the position of zirconium oxide. Previous study suggested the possible ZrO structure for the sub-oxide region, as shown in Fig. 5-3 [70]. After comparing the peak positions, the hexagonal structure is well matched with the sub-oxide oxygen K-edge spectrum. Also, only the stable zirconium oxide with contact in water reveals a clearly split peak consisting a weaker peak at the front and a stronger peak a few eV higher in energy. In contrast to this, both oxygen saturated zirconium oxide, ZrO and $Zr(O)_{sat}$ show a single peak midway between the two peaks positions for ZrO_2. ZrO reveals a chemical shift, compared to ZrO_2 with the edge energy about 1 eV later, which could reveal a reduction in the oxidation state and a reduced amount of charge transfer to the oxygen in this sub-oxide phase, as shown in Fig. 5-4 [71].

A. Yilmazbayhan et al explained that the sub-oxide layer is a metastable ordered solution of O in Zr, although no sub-oxide diffraction peaks could be clearly indexed in TEM [72]. However, small crystallites which can be related to the tetragonal zirconium oxide appear in the rectangular grains in the sub-oxide region, and this could explain the tetragonal oxide is found just near the O/M interface, which is included in the sub-oxide region. This phenomenon was confirmed in another previous study, that he tetragonal-rich phase can be distinguished from the monoclinic phase as a brighter one, which suggest the higher oxygen concentration in the monoclinic-rich zone, as shown in Fig. 5-5. It suggested that the phases of zirconium oxide are characterized by different contents of oxygen [73,74]. The sub oxides are generally of variable thicknesses and do not form continuous layer, however, it influences on the phase of the zirconium oxide, and finally it does the corrosion characteristic of zirconium alloy.

In general, the corrosion rate in the oxidation kinetics in pre-transition zirconium alloy can be described by an empirical law of the form

$$w = At^n \tag{5-1}$$

where w is the weight gain [mg/dm^2], t is the exposure time, and A and n are the constants [31]. The n is a characteristic of each alloy. During the pre-transition oxidation, the corrosion rate of zirconium alloys decreases as the oxide grows. It has been generally considered that the electron and oxygen vacancies are diffused due to the concentration gradient, and the diffusion of charged species influences on the corrosion mechanism [31].

In the case of zirconium oxidation, the n value in equation 5-1 is normally under 0.5, and the kinetics of corrosion rate show the sub-parabolic. The exponent n value can be obtained from the power law between weight gain (oxide thickness) and oxidation time. In Fig. 5-1, the weight gain – oxidation time graphs are presented, and the n value of high dissolved condition is 0.442, and it is higher than the n value of normal DH condition, 0.396. It reveals that the corrosion kinetics of zirconium oxide are influenced by the DH level.

Previous studies revealed that the tetragonal oxide near the O/M interface is important for zirconium alloy corrosion characteristic, and the main reason of transformation is generally known as the stress in the tetragonal zirconium oxide [26,27,50]. The tetragonal phase to monoclinic phase oxide transformation can be represent in the following equation (5-2) with using the Gibbs free energy equation, for the two phases $\Delta G_{t\rightarrow m}$.

$$\Delta G_{t\to m} = \Delta U_{se} + \Delta U_s - \Delta G^c \quad (5\text{-}2)$$

where ΔU_{se} is the elastic strain energy associated with the transformation of the particle, ΔU_s is the change of energy associated with the formation of interfaces when the phase transformation occurs, and ΔG^c is the difference in Gibbs free energy between tetragonal and monoclinic phases. In Equation (5-2), ΔG^c depends on the temperature and composition, ΔU_{se} depends on the modulus of the size or shape of the particles and the surrounding stress, and the ΔU_s depends on the surface characteristics. When the water contacts the tetragonal zirconium oxide grain at high temperature, the change of surface energy ΔU_s could be lower in presence of vapor pressure and water. In addition, during the oxidation process in high temperature water, the water molecules can be combined in the tetragonal zirconium oxide lattice, and it results in the expansion of lattice parameters and accelerating the transformation [75]. The vacancies of oxygen are filled by hydroxyl ions, which moves through the grain boundary, and it is the beginning of the tetragonal to monoclinic transformation enhanced by water. Accordingly, the zirconium oxide transformation mechanism is highly connected to the hydroxyl concentration in water. The detail discussion of the role of DH on oxidation mechanism of zirconium alloy is treated in section 5.3.

Also, the oxide resistivity can be derived from $\mathrm{Re}(\lim_{w\to 0} Z_t)$ measurement, the low frequency, multiplied by a scale factor [76]:

$$\rho_{ox}^{EIS} = S\frac{\mathrm{Re}(\lim_{w\to 0} Z_t)}{\delta_{ox}} \quad (5\text{-}3)$$

with δ_{ox} is the oxide thickness (cm), S is the sample surface (cm^2), and $\mathrm{Re}(\lim_{w\to 0} Z_t)$ is the real impedance in Ω in low frequency range (average value 300 μHz to 3 mHz. The resistivity of oxide ρ_{ox}^{EIS} is independent of oxide thickness and oxidation time, and it is illustrated in Fig. 5-6. Nonetheless, the oxide resistivity at high DH concentration is lower than normal DH concentration in all time scale. It indicates that the properties of oxide change are related to the water chemistry changes and the charged species transport in the oxide.

Previous study shows that the resistivity of Zircaloy-4 as has twice higher than it of of Zr-2.5Nb, and it means a higher resistance to charged species transport through the oxide grown on Zircaloy-4 as compared to Zr- 2.5Nb as shown in Fig. 5-7 [76]. The resistivity analysis results show that in pre-transition state, as the resistivity of oxide increases, the corrosion resistance is enhanced, and

the oxide growth rates decreases. The oxide transport properties are altered by the DH level, which results in a change of oxide resistivity.

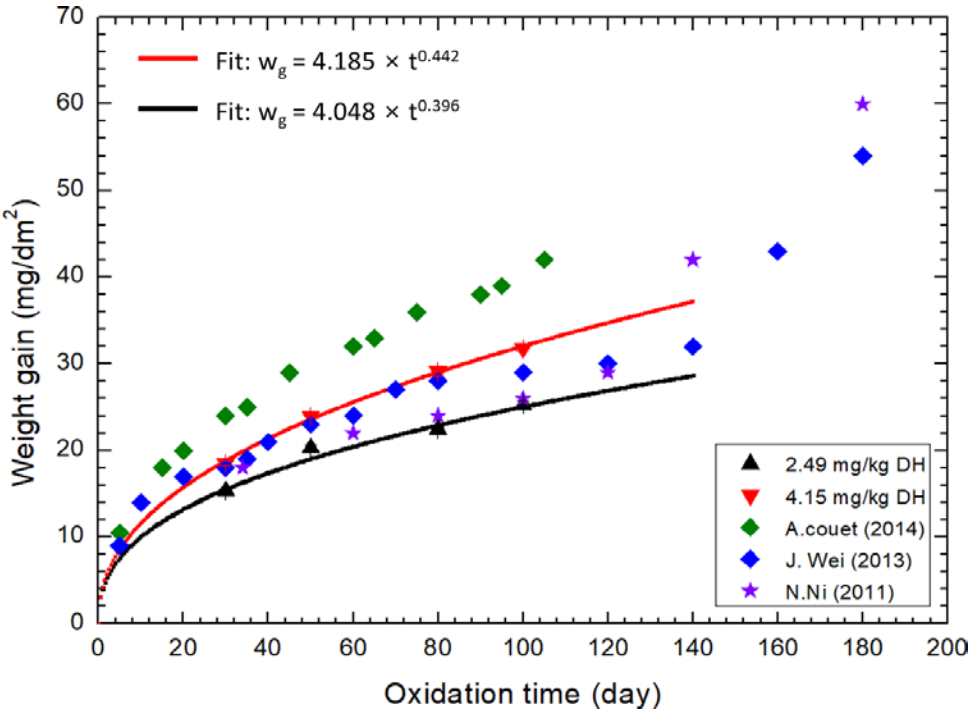

Figure 5-1 The thickness of zirconium oxide with different DH conditions [68,77,78]

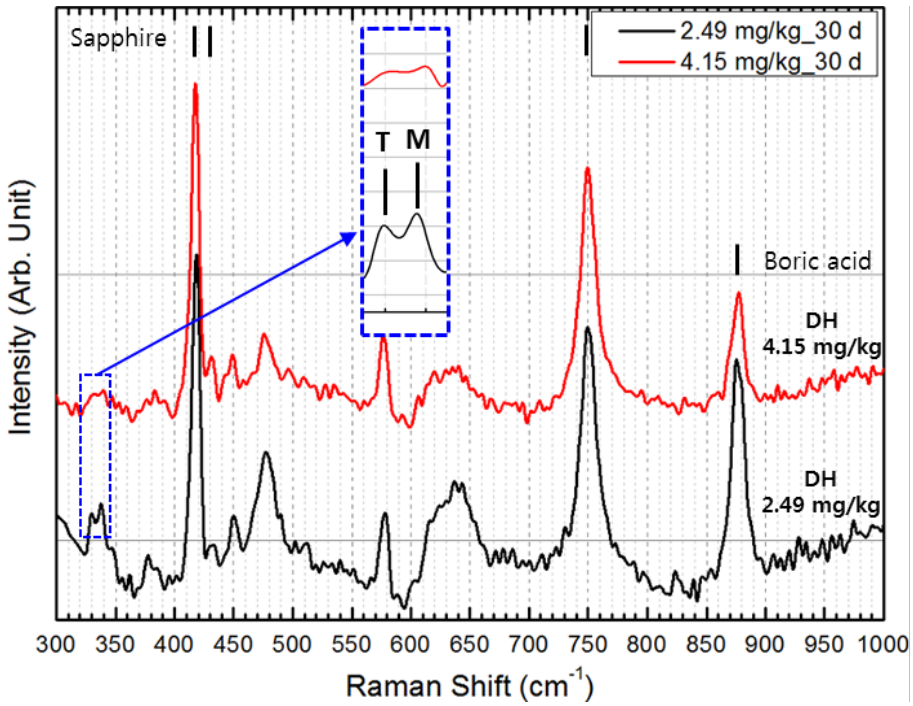

Figure 5-2 Comparison of Raman spectra with different DH conditions [61]

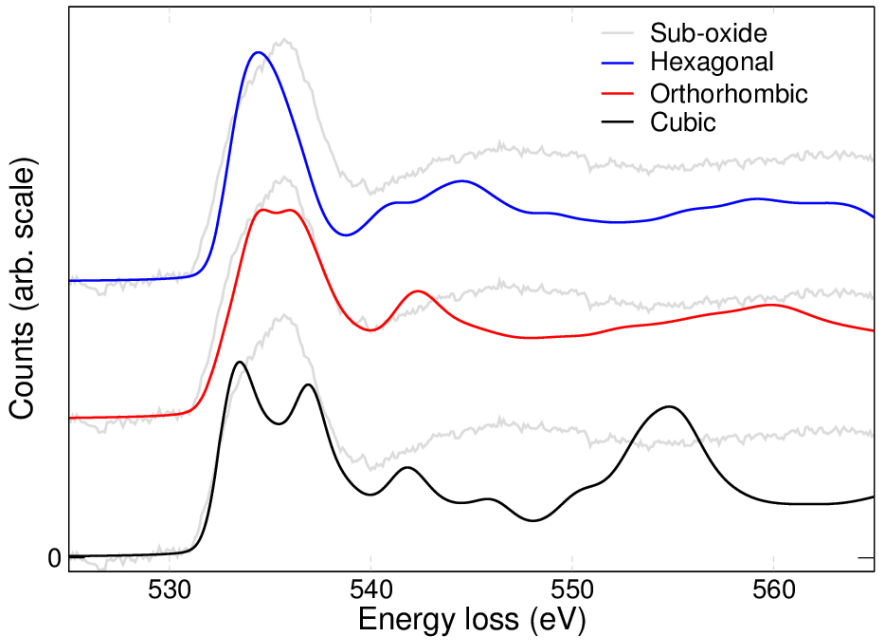

Figure 5-3 Simulated oxygen K-edges from 3 candidate structures along with observed data of the sub-oxide region [70].

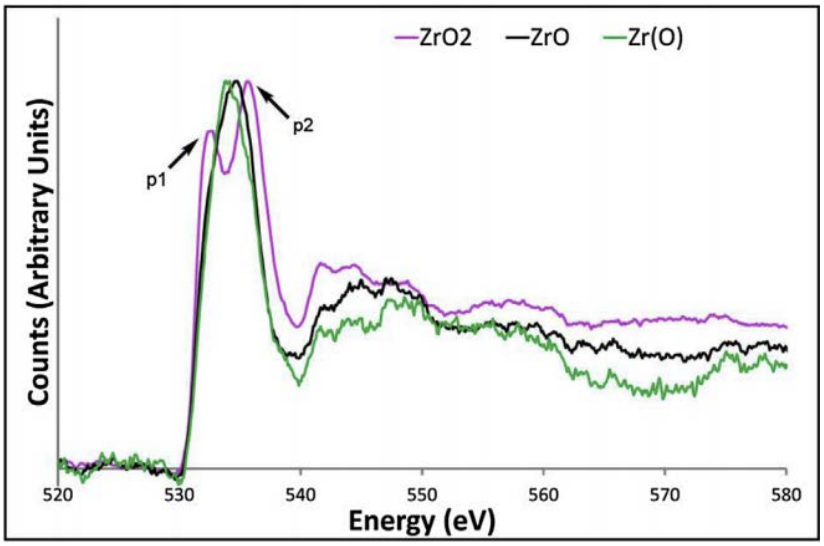

Figure 5-4 Spectra of Oxygen K edges for the zirconium oxide (ZrO_2), oxygen saturated metal (Zr(O)) and the suboxide (ZrO) phases [71].

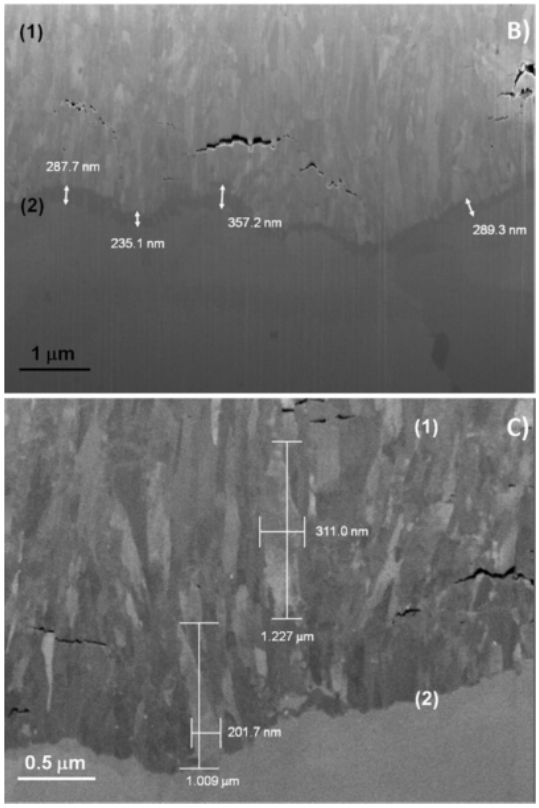

Figure 5-5 In-Lens SEM images. labelled by (1) means the monoclinic phase dominant region, and labeled by (2) means the tetragonal phase dominant region.

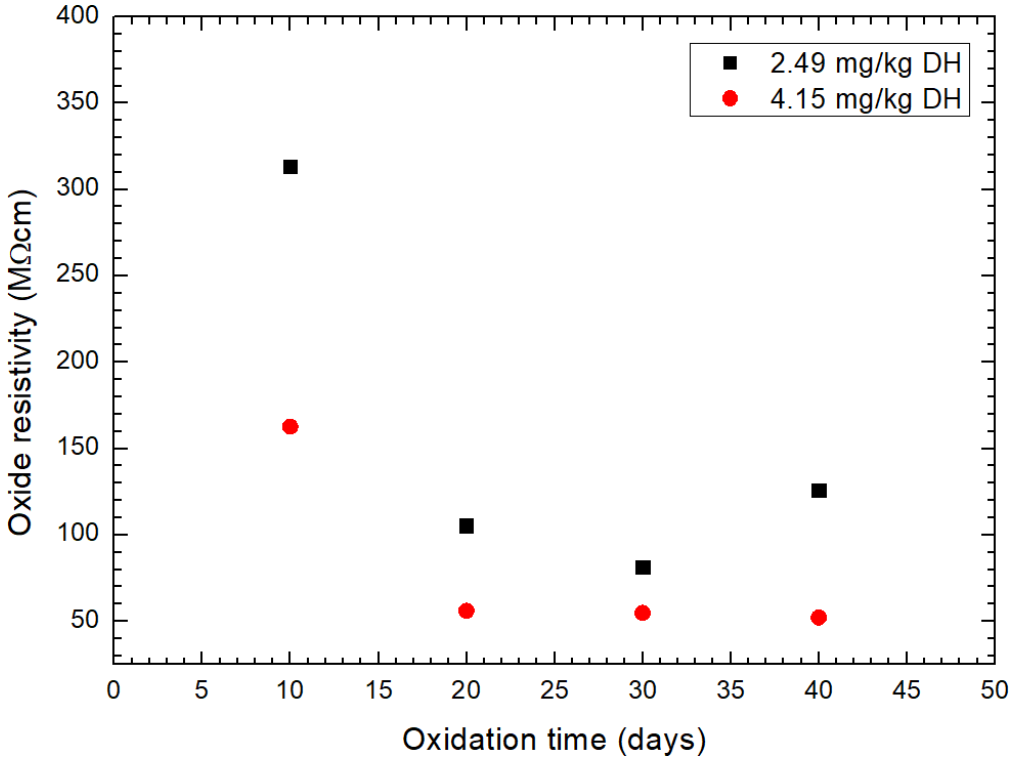

Figure 5-6 Calculated oxide resistivity with various oxidation time and oxidation conditions

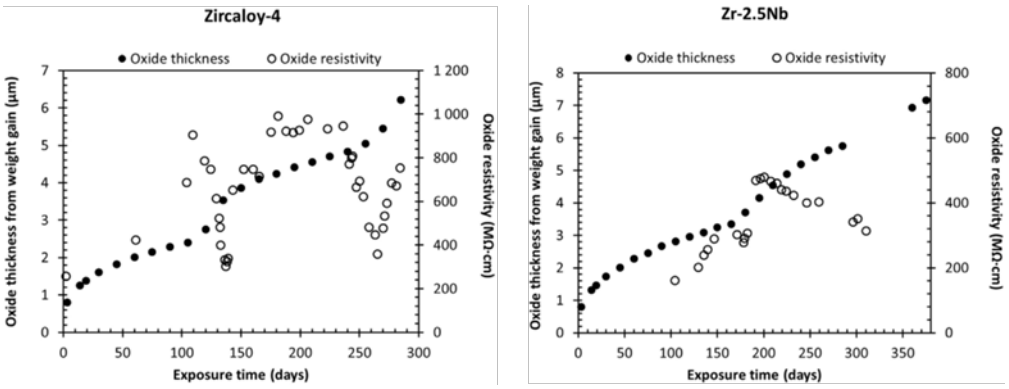

Figure 5-7 The resistivity of oxide film on Zircaloy-4 and Zr-2.5 Nb alloys [76]

Table 5-1 The values of peak position and separation in the O K-edge XAS spectra (Unit: eV)

	e_g	**t_{2g} (sub)**	**t_{2g} (bulk)**	**ΔE (sub)**	**ΔE (bulk)**	**ΔSeparation**
30 d	531.9	536.2	536.9	4.3	5.0	-0.7
50 d	532.0	536.3	536.9	4.3	4.9	-0.6
80 d	532.1	535.9	536.4	3.8	4.3	-0.5
100 d	532.0	535.7	536.4	3.7	4.4	-0.7

5.2 Atomistic structure of interfacial layer between zirconium oxide and high temperature water

The previous research showed that the vacancies are left from the dissolved Y from the oxide surface, forming the penetration paths for water molecules, and it helps the water species to migrate to the oxide much deeper [48]. The fitting results shows that 43.5 and 66.2 % surface metal depletion on YSZ (111) at room temperature and 340 ℃, respectively. It can be explained because of the Y dissolution due to its exposure to water. Also, a density function theory results revealed that the water molecules can be directly interacting with the dissolved metal ions under the oxygen layer, and it leads the water dissociation at the surface to water species [20]. Therefore, sufficient vacancy sites could open space on the top oxygen layer, which could allow the metal ions to be exposed to water, or the metal ions could be exposed to water at the end of YSZ (111) surface.

The presence of the oxygen vacancies is highly related to the hydrophobicity of the oxide surface. The YSZ (111) unit cell has the O – Zr – O structure, and it shows the densest hexagonal packing with the least oxygen vacancies at the surface layer [48]. The bulk water position is found at 6.601 ± 0.027 Å at room temperature, and 7.046 ± 0.038 Å at 340 ℃ temperature. These results reveal that at high temperature, the hydrophobic structure becomes strong, due to the increase of diffusion rate as well as decrease of oxygen vacancy at the YSZ (111) surface layer. Also, the occupancy of the 1st adsorbed layer is much higher and the it of the 2nd layer is lower at high temperature case. It is reasonable that the dissolved metal ion is adsorbed at high temperature case. Also, the water species are adsorbed much stronger at room temperature, and it means the hydrophilic characteristic is revealed at room temperature case.

From XRR analysis, the hydration structures of YSZ (111) surface was investigated, and the electron density profile reveals that the chemically adsorbed water species fill the metal depleted sites and oxygen vacancies near the oxide surface. There are 2 additional layers just above the termination oxygen layer, and the first layer is consisted of the metal species and the second one is consisted of water species. From these results, the very early stage of hydration of zirconium oxide at high temperature can be investigated, and the characteristic of oxide/water interface can be revealed.

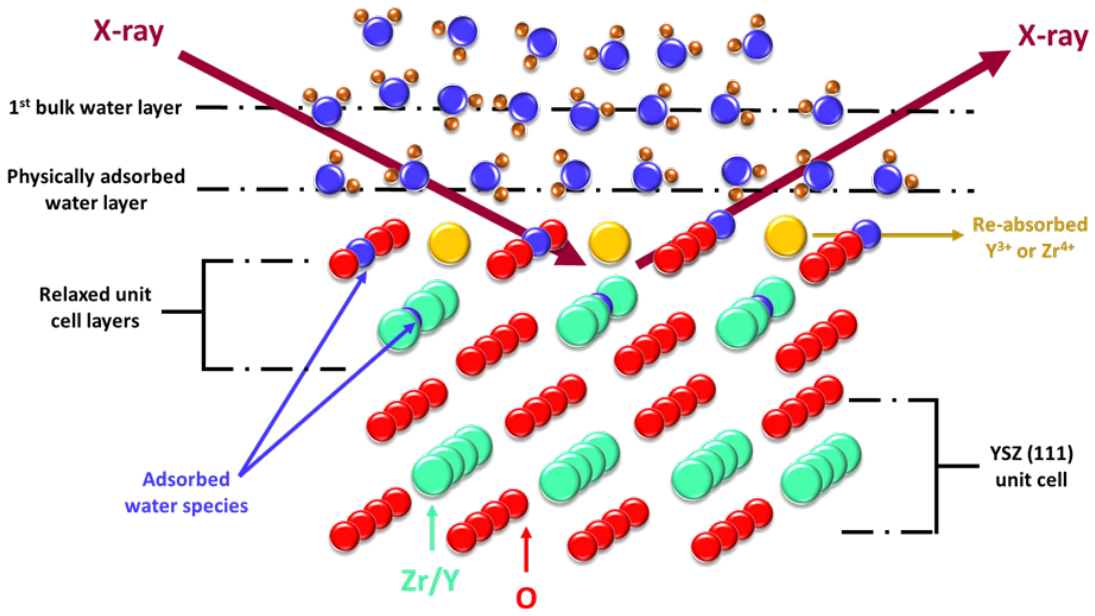

Figure 5-8 Schematic of YSZ (111) and water interface structure

5.3 Role of DH on corrosion characteristic of zirconium alloy in high temperature water

Previous research showed that the phase transformation of zirconium oxide influences on the corrosion characteristic of zirconium alloy, and the phase transformation is controlled by the water chemistry of the system [3,79]. The DH level in high temperature water influences on the water chemistry of the system, especially the hydrolysis of water itself [5]. The concentration of DH peroxide, one of by-products of hydrolysis, is reduced in high DH concentration compared to normal DH concentration [80]. At high DH concentration, the oxygen production and the water decomposition could be suppressed, and it decreases the hydroxyl ion and hydrogen peroxide concentration, through the chain reactions [80]. Previous studies showed that the crystallization temperature of tetragonal phase decreases due to the hydrogen peroxide [81,82]. Moreover, there are 3 types of hydrated zirconium ion (Zr^{4+}) polycations, and α-type of zirconium ion polycation can be act as a tetragonal oxide phase precursor, and H_2O_2 becomes for the stabilizer of α-type Zr^{4+} polycation, as shown in Fig. 5-9 [82]. In high DH concentration, the high DH makes the decrease of H_2O_2, and it has resulted in the un-stabilization of tetragonal zirconium oxide. Figure 5-10, the schematics of water species concentration and the corrosion characteristic of zirconium alloy is presented.

As discussed above, the tetragonal oxide phase to monoclinic oxide phase transformation is enhanced, and this can be revealed by in-situ Raman spectroscopy, as shown in Fig. 5-2. The tetragonal phase can be stabilized by a small size grain, therefore it remains stable throughout the corrosion process in high temperature hydrogenated water [4]. But, the different corrosion rates observed in different DH conditions could be related to the phase stability of the zirconium oxide, and the high DH concentration results in the fast oxide growth rate at high temperature water environment.

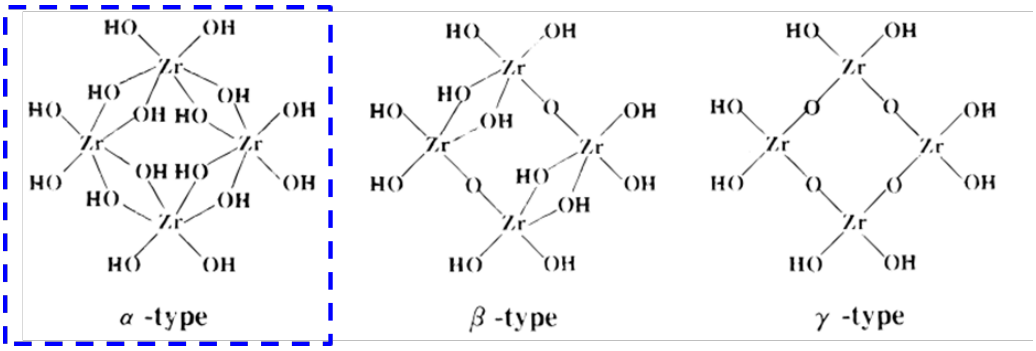

Figure 5-9 Possible model structures for hydrated Zr4+ polycations [82]

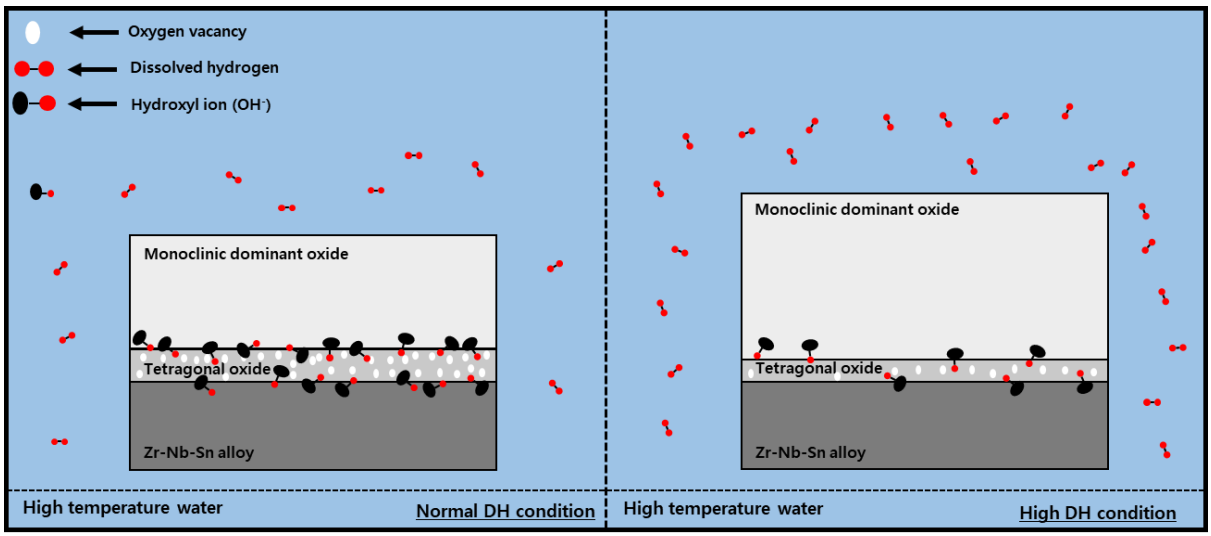

Figure 5-10 The schematic image of water species concentration and the oxide thickness of zirconium alloy at different DH condition at high temperature water environment

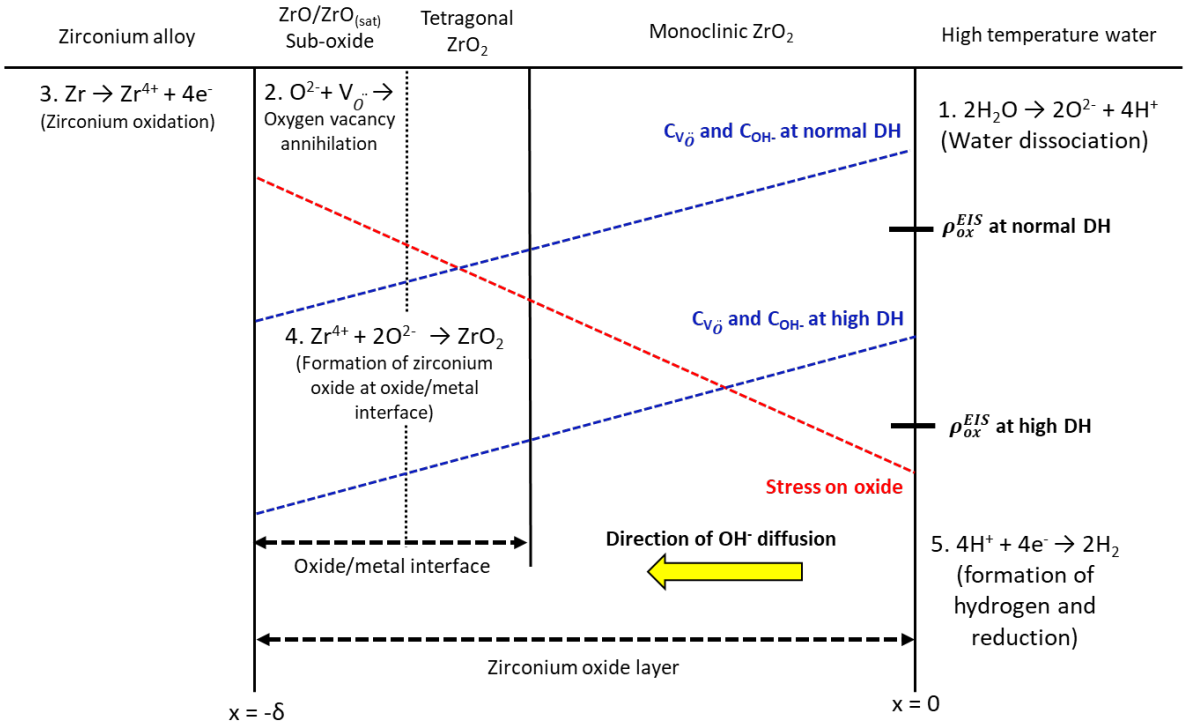

Figure 5-11 A model for corrosion of zirconium alloy in high temperature water condition

6. Conclusion

In this thesis, the effects of the DH concentration on the corrosion characteristic and distribution of oxide phase of a Zr–Nb–Sn alloy have been studied in simulated primary water environment. The corrosion rate of Zr–Nb–Sn alloy is lower in the normal DH concentration (2.49 mg/kg) than high DH concentration (2.49 mg/kg) of primary water chemistry of pressurized water reactors. The instability of the tetragonal oxide phase is revealed from Raman spectra at high DH concentration. Accordingly, the tetragonal phase to monoclinic oxide phase transformation is enhanced in high DH concentration. Also, the in-situ EIS results indicate that the resistivity of oxide film on Zr-Nb-Sn alloy can be changed due to the DH level.

The synchrotron X-ray reflectivity performed on the YSZ (111)/water interface to investigate the hydration mechanism at the interface. It was founded that the high temperature water can influence on the structure of top layer oxide, and the adsorbed layers are consisted of metal species and the physiosorbed water species. This indicates that the hydrophobic and hydrophilic characteristic of the zirconium oxide surface is related to the oxygen vacancy, and it seems that the hydrophobic structure becomes strong, due to the increase of diffusion rate as well as decrease of oxygen vacancy at the YSZ (111) surface layer at high temperature. Also, significant metal depletion for zirconium oxide surface, which is correlated to the relaxation of surface layer, which results in a huge lattice constant reduction at top of the unit cell layer.

At the O/M interface, the phase transformation of zirconium oxide occurs, and it can be revealed by electronic structure and hybridization effect. To improve the corrosion resistance of zirconium alloys, it is important to delay the phase transformation and reduce the internal stress produced by transformation. From the high level of DH, the water decomposition happens, and the tetragonal phase oxide becomes unstable. Therefore, it is observed that the corrosion resistance of Zr-Nb-Sn alloy is lower due to instability of tetragonal phase oxide.

Followings are the conclusions of this thesis;

1. At high DH case, the concentration of hydroxyl ion decreases, and it leads the annihilation of oxygen vacancy at O/M interface.

2. Due to the reduced number of oxygen vacancies, the tetragonal to monoclinic zirconium oxide phase transformation accelerated, therefore the resistivity of oxide decreases.

3. The water species are much easier diffused into the O/M interface at high DH condition, then the oxide grows faster at the O/M interface at high DH condition during pre-transition state of zirconium oxidation.

The proper amount of DH level is highly required for enhancing the corrosion resistance of nickel-based alloy, and zirconium fuel cladding materials in high temperature water condition. The DH level for operation nuclear power plant should be considered with comprehensive understanding of zirconium fuel cladding materials and structure materials, and it is inappropriate to decide the upper limitation of DH range without the further work.

Reference

[1] http://www.nuclear-power.net

[2] J.E. Maslar, W.S. Hurst, W.J. Bowers, J.H. Hendricks, In situ Raman spectroscopic investigation of zirconium-niobium alloy corrosion under hydrothermal conditions, J. Nucl. Mater. 298 (2001) 239–247.

[3] B. Cox, Some thoughts on the mechanisms of in-reactor corrosion of zirconium alloys, J. Nucl. Mater. 336 (2005) 331–368.

[4] N. Ni, D. Hudson, J. Wei, P. Wang, S. Lozano-Perez, G.D.W. Smith, J.M. Sykes, S.S. Yardley, K.L. Moore, S. Lyon, R. Cottis, M. Preuss, C.R.M. Grovenor, How the crystallography and nanoscale chemistry of the metal/oxide interface develops during the aqueous oxidation of zirconium cladding alloys, Acta Mater. 60 (2012) 7132–7149.

[5] J. Chevalier, L. Gremillard, A. V. Virkar, D.R. Clarke, The tetragonal-monoclinic transformation in zirconia: Lessons learned and future trends, J. Am. Ceram. Soc. 92 (2009) 1901–1920.

[6] S. Deville, G. Guenin, J. Chevalier, Martensitic transformation in zirconiaPart II. Martensite growth, Acta Mater. 52 (2004) 5709–5721.

[7] Y. Ding, D.O. Northwood, TEM study of the oxide-metal interface formed during corrosion of Zr-2.5wt.%Nb pressure tubing, Mater. Charact. 30 (1993) 13–22.

[8] H. Anada, K. Takeda, Microstructure of Oxides on Zircaloy-4, 1.0Nb Zircaloy-4, and Zircaloy-2 Formed in 10.3-MPa Steam at 673 K, Zircon. Nucl. Ind. 11th Int. Symp. ASTM STP 1295. 1295 (1996) 35–54.

[9] T. Kim, K.J. Choi, S.C. Yoo, J.H. Kim, Effects of dissolved hydrogen on the crack-initiation and oxidation behavior of nickel-based alloys in high-temperature water, Corros. Sci. 106 (2016) 260–270.

[10] P.L. Andresen, J. Hickling, a Ahluwalia, J. Wilson, Effects of Hydrogen on Stress Corrosion Crack Growth Rate of Nickel Alloys in High-Temperature Water, Corrosion. 64 (2008) 707–

720.

[11] Y. Qiu, T. Shoji, Z. Lu, Effect of dissolved hydrogen on the electrochemical behaviour of Alloy 600 in simulated PWR primary water at 290 °C, Corros. Sci. 53 (2011) 1983–1989.

[12] T. Nakagawa, N. Totsuka, T. Terachi, N. Nakajima, Influence of Dissolved Hydrogen on Oxide Film and PWSCC of Alloy 600 in PWR Primary Water, J. Nucl. Sci. Technol. 40 (2003) 39–43.

[13] F. Meng, Z. Lu, T. Shoji, J. Wang, E. Han, W. Ke, Stress corrosion cracking of uni-directionally cold worked 316NG stainless steel in simulated PWR primary water with various dissolved hydrogen concentrations, Corros. Sci. 53 (2011) 2558–2565.

[14] A. Loucif, J.P. Petit, Y. Wouters, Semiconducting behavior and bandgap energies of oxide films grown on alloy 600 under PWR simulated primary water conditions with different dissolved hydrogen contents, J. Nucl. Mater. 443 (2013) 222–229.

[15] P. Platt, E. Polatidis, P. Frankel, M. Klaus, M. Gass, R. Howells, M. Preuss, A study into stress relaxation in oxides formed on zirconium alloys, J. Nucl. Mater. 456 (2015) 415–425.

[16] E. Polatidis, P. Frankel, J. Wei, M. Klaus, R.J. Comstock, A. Ambard, S. Lyon, R. A. Cottis, M. Preuss, Residual stresses and tetragonal phase fraction characterisation of corrosion tested Zircaloy-4 using energy dispersive synchrotron X-ray diffraction, J. Nucl. Mater. 432 (2013) 102–112.

[17] W. Qin, C. Nam, H.L. Li, J. A. Szpunar, Tetragonal phase stability in ZrO_2 film formed on zirconium alloys and its effects on corrosion resistance, Acta Mater. 55 (2007) 1695–1701.

[18] R. Konings, T. Allen, R. Stoller, S. Yamanaka, Comprehensive Nuclear Materials, Elsevier, Amsterdam. (2012)

[19] J.-Y. Park, B.-K. Choi, Y.H. Jeong, Y.-H. Jung, Corrosion behavior of Zr alloys with a high Nb content, J. Nucl. Mater. 340 (2005) 237–246.

[20] J. Huang, M. Yao, C. Gao, X. Liang, J. Peng, J. Zhang, B. Zhou, The influence of second phase particles on the crack formation in oxide films formed on zirconium alloys, Corros. Sci. 99 (2015) 172–177.

[21] J.-Y. Park, B.-K. Choi, S.J. Yoo, Y.H. Jeong, Corrosion behavior and oxide properties of Zr–1.1wt%Nb–0.05wt%Cu alloy, J. Nucl. Mater. 359 (2006) 59–68.

[22] D. Pêcheur, F. Lefebvre, A.T. Motta, C. Lemaignan, J.F. Wadier, Precipitate evolution in the Zircaloy-4 oxide layer, J. Nucl. Mater. 189 (1992) 318–332.

[23] H. Okamoto, O-Zr (Oxygen-Zirconium), J. Phase Equilibria Diffus. 28 (2007) 498.

[24] V. Y. Gertsman, Y. P. Lin, a. P. Zhily, Special grain boundaries in zirconia corrosion films, Philos. Mag. A. 79 (1999) 1567–1590.

[25] D. Wang, Y. Guo, K. Liang, K. Tao, Crystal structure of zirconia by Rietveld refinement, Sci. China Ser. A Math. 42 (1999) 80–86.

[26] J. Lin, H. Li, C. Nam, J. A. Szpunar, Analysis on volume fraction and crystal orientation relationship of monoclinic and tetragonal oxide grown on Zr-2.5Nb alloy, J. Nucl. Mater. 334 (2004) 200–206.

[27] N. Pétigny, P. Barberis, C. Lemaignan, C. Valot, M. Lallemant, In situ XRD analysis of the oxide layers formed by oxidation at 743 K on Zircaloy 4 and Zr–1NbO, J. Nucl. Mater. 280 (2000) 318–330.

[28] G. Sundell, M. Thuvander, H.-O. Andrén, Barrier oxide chemistry and hydrogen pick-up mechanisms in zirconium alloys, Corros. Sci. 102 (2016) 490–502.

[29] M. Guerain, C. Duriez, J.L. Grosseau-Poussard, M. Mermoux, Review of stress fields in Zirconium alloys corrosion scales, Corros. Sci. 95 (2015) 11–21.

[30] J.K. Dawson, G. Long, W.E. Seddon, J.F. White, The kinetics and mechanism of the oxidation of zircaloy-2 at 350–500 °C, J. Nucl. Mater. 25 (1968) 179–200.

[31] A.T. Motta, A. Couet, R.J. Comstock, Corrosion of Zirconium Alloys Used for Nuclear Fuel Cladding, Annu. Rev. Mater. Res. 45 (2015) 311–343.

[32] B. Griggs, H.P. Maffei, D.W. Shannon, Multiple Rate Transitions in the Aqueous Corrosion of Zircaloy, J. Electrochem. Soc. 109 (1962) 665.

[33] A.J.G. Maroto, R. Bordoni, M. Villegas, A.M. Olmedo, M. a. Blesa, A. Iglesias, P. Koenig, Growth and characterization of oxide layers on zirconium alloys, J. Nucl. Mater. 229 (1996)

79–92.

[34] P. Barberis, T. Merle-Méjean, P. Quintard, On Raman spectroscopy of zirconium oxide films, J. Nucl. Mater. 246 (1997) 232–243.

[35] P. Barberis, Zirconia powders and Zircaloy oxide films: tetragonal phase evolution during 400°C autoclave tests, J. Nucl. Mater. 226 (1995) 34–43.

[36] P. Millett, PWR Primary Water Chemistry Guidelines Volume 2, Revision 4, EPRI Report. (1999)

[37] K. Dozaki, D. Akutagawa, N. Nagata, H. Takiguchi, K. Norring, Effects of Dissolved Hydrogen Content in PWR Primary Water on PWSCC Initiation Property, E-Journal Adv. Maint. 2 (2010) 65–76.

[38] J. Xu, T. Shoji, C. Jang, The effects of dissolved hydrogen on the corrosion behavior of Alloy 182 in simulated primary water, Corros. Sci. (2015).

[39] L.I.L. Lima, M.M. A. M. Schvartzman, C. A. Figueiredo, A. Q. Bracarense, Stress corrosion cracking behavior of alloy 182 weld in pressurized water reactor primary water environment at 325 ℃, Corrosion. 67 (2011) 0850041–0850049.

[40] L.J. Oblonsky, T.M. Devine, A surface enhanced Raman spectroscopic study of the passive films formed in borate buffer on iron, nickel, chromium and stainless steel, Corros. Sci. 37 (1995) 17–41.

[41] J. Gui, T.M. Devine, In situ vibrational spectra of the passive film on iron in buffered borate solution, Corros. Sci. 32 (1991) 1105–1124.

[42] J. Gui, Obtaining Surface-Enhanced Raman Spectra from the Passive Film on Iron, J. Electrochem. Soc. 138 (1991) 1376.

[43] A. Kikas, J. Aarik, V. Kisand, K. Kooser, T. Käämbre, H. Mändar, T. Uustare, R. Rammula, V. Sammelselg, I. Martinson, Effect of phase composition on X-ray absorption spectra of ZrO 2 thin films, J. Electron Spectros. Relat. Phenomena. 156158 (2007) 303–306.

[44] H. Hulme, F. Baxter, R.P. Babu, M.A. Denecke, M. Gass, A. Steuwer, K. Norén, S. Carlson, M. Preuss, An X-ray absorption near-edge structure (XANES) study of the Sn L3 edge in

zirconium alloy oxide films formed during autoclave corrosion, Corros. Sci. 105 (2016) 202–208.

[45] H. Akhiani, A. Hunt, X. Cui, A. Moewes, J. Szpunar, The electronic structure of zirconium in hydrided and oxidized states, J. Alloys Compd. 622 (2015) 463–470.

[46] P. Fenter, N.C. Sturchio, Mineral–water interfacial structures revealed by synchrotron X-ray scattering, Prog. Surf. Sci. 77 (2004) 171–258.

[47] P. a. P. Fenter, X-ray Reflectivity as a Probe of Mineral-Fluid Interfaces: A User Guide, Rev. Mineral. Geochemistry. 49 (2002) 149–221.

[48] B. Hou, S. Kim, T. Kim, C. Park, C.B. Bahn, J. Kim, S. Hong, S.Y. Lee, J.H. Kim, Orientation-Dependent Hydration Structures at Yttria-Stabilized Cubic Zirconia Surfaces, J. Phys. Chem. C. 120 (2016) 29089–29097.

[49] B. Hou, S. Kim, T. Kim, J. Kim, S. Hong, C.B. Bahn, C. Park, J.H. Kim, The Hydration Structure at Yttria-Stabilized Cubic Zirconia (110)-Water Interface with Sub-Ångström Resolution, Sci. Rep. 6 (2016) 27916.

[50] T. Kim, J. Kim, K.J. Choi, S.C. Yoo, S. Kim, J.H. Kim, Phase Transformation of Oxide Film in Zirconium Alloy in High Temperature Hydrogenated Water, Corros. Sci. 99 (2015) 134–144.

[51] C. Miyake, A. Nakatani, T. Isobe, Electron spin resonance study of oxide films on Zircaloy claddings — part (I), J. Nucl. Mater. 217 (1994) 172–177.

[52] H. Hong, S. Kim, K. Lee, Effects of alloying elements on the tensile properties and oxidation behavior of modified Zircaloy-4 in 360 °C water, J. Nucl. Mater. 238 (1996) 211–217.

[53] M. Bojinov, V. Karastoyanov, P. Kinnunen, T. Saario, Influence of water chemistry on the corrosion mechanism of a zirconium-niobium alloy in simulated light water reactor coolant conditions, Corros. Sci. 52 (2010) 54–67.

[54] J. Kim, S.H. Kim, K.J. Choi, C.B. Bahn, I.S. Hwang, J.H. Kim, In-situ investigation of thermal aging effect on oxide formation in Ni-base alloy/low alloy steel dissimilar metal weld interfaces, Corros. Sci. 86 (2014) 295–303.

[55] J. Kim, K.J. Choi, C.B. Bahn, J.H. Kim, In situ Raman spectroscopic analysis of surface oxide films on Ni-base alloy/low alloy steel dissimilar metal weld interfaces in high-temperature water, J. Nucl. Mater. 449 (2014) 181–187..

[56] A. Garner, A. Gholinia, P. Frankel, M. Gass, I. MacLaren, M. Preuss, The microstructure and microtexture of zirconium oxide films stiudied by transmission electron backscatter diffraction and automated crystal orientation mapping with transmission electron microscopy, Acta Mater. 80 (2014) 159–171.

[57] R.J. Nicholls, N. Ni, S. Lozano-Perez, A. London, D.W. McComb, P.D. Nellist, C.R.M. Grovenor, C.J. Pickard, J.R. Yates, Crystal Structure of the ZrO Phase at Zirconium/Zirconium Oxide Interfaces, Adv. Eng. Mater. 17 (2015) 211–215.

[58] J.H. Kim, I.S. Hwang, Development of an in situ Raman spectroscopic system for surface oxide films on metals and alloys in high temperature water, Nucl. Eng. Des. 235 (2005) 1773.

[59] M. Kadleíková, J. Breza, M. Veselý, Raman spectra of synthetic sapphire, Microelectronics J. 32 (2001) 955–958.

[60] C.M. Phillippi, K.S. Mazdiyasni, Infrared and Raman Spectra of Zirconia Polymorphs, J. Am. Ceram. Soc. 54 (1971) 254–258.

[61] T. Kim, K.J. Choi, S.C. Yoo, Y. Lee, J.H. Kim, Influence of dissolved hydrogen on the early stage corrosion behavior of zirconium alloys in simulated light water reactor coolant conditions, Corros. Sci. 131 (2017) 235–244.

[62] B.-K. Kim, H. Hamaguchi, Mode Assignments of the Raman Spectrum of Monoclinic Zirconia by Isotopic Exchange Technique, Phys. Status Solidi. 203 (1997) 557–563.

[63] L. Kurpaska, J. Favergeon, L. Lahoche, M. El-Marssi, J.-L. Grosseau Poussard, G. Moulin, J.-M. Roelandt, Raman spectroscopy analysis of air grown oxide scale developed on pure zirconium substrate, J. Nucl. Mater. 466 (2015) 460–467.

[64] A. Froideval, C. Degueldre, C.U. Segre, M. a. Pouchon, D. Grolimund, Niobium speciation at the metal/oxide interface of corroded niobium-doped Zircaloys: A X-ray absorption near-edge structure study, Corros. Sci. 50 (2008) 1313–1320.

[65] D.J. Spengler, A.T. Motta, R. Bajaj, J.R. Seidensticker, Z. Cai, Characterization of Zircaloy-4 corrosion films using microbeam synchrotron radiation, J. Nucl. Mater. 464 (2015) 107–118.

[66] Y. Lei, Y. Ito, N.D. Browning, T.J. Mazanec, Segregation Effects at Grain Boundaries in Fluorite-Structured Ceramics, J. Am. Ceram. Soc. 63 (2002) 2359–2363.

[67] P. Bevington, D. Robinson, Data reduction and error analysis for the physical sciences, New York McGraw-Hill. (1992)

[68] J. Wei, P. Frankel, E. Polatidis, M. Blat, A. Ambard, R.J. Comstock, L. Hallstadius, D. Hudson, G.D.W. Smith, C.R.M. Grovenor, M. Klaus, R.A. Cottis, S. Lyon, M. Preuss, The effect of Sn on autoclave corrosion performance and corrosion mechanisms in Zr-Sn-Nb alloys, Acta Mater. 61 (2013) 4200–4214.

[69] J. Lin, H. Li, J.A. Szpunar, R. Bordoni, A.M. Olmedo, M. Villegas, A.J.G. Maroto, Analysis of zirconium oxide formed during oxidation at 623 K on Zr-2.5Nb and Zircaloy-4, Mater. Sci. Eng. A. 381 (2004) 104–112.

[70] R.J. Nicholls, N. Ni, S. Lozano-Perez, A. London, D.W. McComb, P.D. Nellist, C.R.M. Grovenor, C.J. Pickard, J.R. Yates, Crystal structure of the ZrO phase at zirconium/zirconium oxide interfaces, Adv. Eng. Mater. 17 (2015) 211–215.

[71] K.J. Annand, I. Maclaren, M. Gass, Utilising DualEELS to probe the nanoscale mechanisms of the corrosion of Zircaloy-4 in 350°C pressurised water, J. Nucl. Mater. 465 (2015) 390–399.

[72] A. Yilmazbayhan, E. Breval, A.T. Motta, R.J. Comstock, Transmission electron microscopy examination of oxide layers formed on Zr alloys, J. Nucl. Mater. 349 (2006) 265–281.

[73] L. Kurpaska, I. Jozwik, J. Jagielski, Study of sub-oxide phases at the metal-oxide interface in oxidized pure zirconium and Zr-1.0% Nb alloy by using SEM/FIB/EBSD and EDS techniques, J. Nucl. Mater. 476 (2016) 56–62.

[74] J. Hu, A. Garner, N. Ni, A. Gholinia, R.J. Nicholls, S. Lozano-Perez, P. Frankel, M. Preuss, C.R.M. Grovenor, Identifying suboxide grains at the metal-oxide interface of a corroded Zr-1.0%Nb alloy using (S)TEM, transmission-EBSD and EELS, Micron. 69 (2015) 35–42.

[75] H.G. Kim, J.Y. Park, B.K. Choi, Y.H. Jeong, Evaluation of pre-transition oxide on Zr-0.4 Nb

alloy by using the HVEM, J. Nucl. Mater. 374 (2008) 204–210.

[76] A. Couet, A.T. Motta, A. Ambard, D. Livigni, In-situ electrochemical impedance spectroscopy measurements of zirconium alloy oxide conductivity: Relationship to hydrogen pickup, Corros. Sci. 119 (2017) 1–13.

[77] A. Couet, A.T. Motta, R.J. Comstock, Hydrogen pickup measurements in zirconium alloys: Relation to oxidation kinetics, J. Nucl. Mater. 451 (2014) 1–13.

[78] N. Ni, S. Lozano-Perez, J.M. Sykes, G.D.W. Smith, C.R.M. Grovenor, Focussed ion beam sectioning for the 3D characterisation of cracking in oxide scales formed on commercial ZIRLO™ alloys during corrosion in high temperature pressurised water, Corros. Sci. 53 (2011) 4073–4083.

[79] Y.S. Kim, Y.H. Jeong, S.B. Son, A study on the effects of dissolved hydrogen on zirconium alloys corrosion, J. Nucl. Mater. 444 (2014) 349–355.

[80] C.C. Lin, Radiochemistry in Nuclear Power Reactors, National Acadmy Press, Washington D.C. (1996)

[81] K. Kukli, K. Forsgren, J. Aarik, T. Uustare, A. Aidla, A. Niskanen, M. Ritala, M. Leskelä, A. Hårsta, Atomic layer deposition of zirconium oxide from zirconium tetraiodide, water and hydrogen peroxide, J. Cryst. Growth. 231 (2001) 262–272.

[82] J.A. Navio, G. Colón, P.J. Sánchez-Soto, M. Macias, Effects of H_2O_2 and SO_4^{2-} Species on the Crystalline Structure and Surface Properties of ZrO2 Processed by Alkaline Precipitation, Chem. Mater. 9 (1997) 1256–1261.

Acknowledgement

2009년 학부생으로 UNIST에 입학을 한 지 어느덧 9년이라는 시간이 지났습니다. 그 해 겨울방학, 원자력 공학이라는 학문에 첫 발을 디디게 해 주신 지도 교수님, 김지현 교수님께 가장 먼저 감사의 말씀을 전합니다. 여러가지로 부족한 부분이 많은 저에게 연구의 방향을 조언해 주셨을 뿐만 아니라, 아낌없는 지원 덕분에 무사히 학위과정을 마칠 수 있었던 것 같습니다. 또한, 학술적인 부분과 더불어 공학자라는 삶에 대한 여러 조언들도 염두하고 살아갈 수 있도록 하겠습니다.

방인철 교수님, 항상 원자력 공학자란 무엇인가라는 질문을 갖게 해 주셨고, 그간 주셨던 교수님의 조언들이 미래의 제 연구의 바탕이 되도록 노력하겠습니다. 반치범 교수님, 미국 ANL에 계실 때부터 많은 도움 주시고, 여러 재료들의 부식 시험 결과에 대한 아낌없는 조언 덕분에 좋은 연구 성과들을 얻어낼 수 있었던 것 같습니다. 김현길 박사님, 대학원 초기부터 시작한 연구 결과에 대해 심도 있는 디스커션과 경험해 주신 것들을 바탕으로 지금까지 연구를 수행해 왔던 것 같습니다. 권순용 교수님, 이번 학위 논문 심사에서 주신 조언들을 잊지 않고 연구에 정진하는 삶을 살 수 있도록 하겠습니다.

그리고 아르곤 연구소와 포항 가속기 연구소에서 많은 도움을 주신 박창용 박사님, Dr. Hou, 김남동 박사님, 이수용 박사님께도 감사드립니다. 처음에 가지고 있던 새로운 실험 장비에 대한 두려움을 도전정신과 더 넓은 시야로 바꿔 주신 것 같습니다.

지난 9년간 UNIMAT에서 함께 연구실 생활을 한 선배님, 동기들과 후배들에게도 고마운 마음을 전합니다. 김종진 박사님과 신상훈 박사님, 연구의 방향과 문제 해결 방법에 대한 여러 조언은 항상 잊지 않겠습니다. 최경준 박사님, 함께 실험실에서 이런 저런 일들을 겪으며 어려운 일과 힘든 실험들을 잘 이겨내도록 해 주셔서 감사합니다. 상일이도 묵묵하게 항상 자신의 할 일을 하는 것을 보면서 나에게 깨달음을 준 점 고맙게 생각한다.

다음으로 승현, 여기에는 다 적지 못할 정도로 함께 여러 실험들과 일들을 함께

해온 것 같네. 그 동안 여러 도움을 많이 받은 만큼 나중에는 그만큼 도와줄 수 있도록 더 노력할게. 광범이도 학부생 때부터 지금까지 좋은 일들 안 좋은 일들도 함께 겪으며 여기까지 왔는데 조금 더 힘내서 박사과정 잘 마무리했으면 좋겠다. 승창, 항상 성실한 모습으로 연구실에서 중간 다리 역할을 수행하는 모습을 보면서 본받을 점이 많다고 생각했어. 그 동안 노력한 만큼 나중엔 좋은 결실 있을 거라 믿어. 정현이도 지금 하고 있는 액체 금속과 관련 재료에 대한 연구를 잘 진행해 나가면 미래에는 좋은 결과를 얻게 될 거라 생각해. 인영, 준혁, 태용이도 지금부터 맡은 일들 잘 해결하다 보면 원하는 연구와 목표를 이룰 수 있을 거야. 윤주와 기동형도 막내(?) 비슷하게 있으면서 여러 일들도 맡아서 하시며 고생하는 모습을 보면 감사한 생각이 듭니다. 특히 윤주는 학부생 때부터 지르코늄 부식 실험들도 많이 도와주고 지금 하는 실험들도 여러 어려움들을 극복하고 진행하는 모습 보면 든든하게 보여. 마지막으로 내년에 입학해 고생할 막내 정환이도 남은 학부생 생활 잘 마무리하고 대학원에서도 열심히 하는 모습 보여주면 좋겠다.

연구실에 여러 일들 있을 때마다 외적으로도 도움을 주었던 열수력 연구실 인국이, 경모, 석빈, 성보, 영신이, 학부생 때 취업한 정민이, 노심 연구실 현석이도 하는 일 다 잘 되길 바란다. 또 고등학교 때부터 지금까지 힘든 모습 보일 때마다 다독여준 성윤, 성현, 원태, 종윤, 동욱이에게도 진심으로 고맙다는 말을 전하고 싶어. 가끔 서울에 가서 술 마시며 이야기 나누는 것들이 큰 힘이 되었던 것 같다. 또 09 첫 룸메이트로 만나 지금까지 여러 일들을 함께 해온 종원, 상걸이에게도 감사의 인사를 전하고 싶어.

마지막으로 부모님께도 감사의 인사를 전합니다. 지금의 제가 있는 것은 모두 부모님 덕분입니다. 사랑합니다. 형이 울산에서 부모님 잘 챙겨드리지 못하는 부분을 집에서 여러모로 챙겨준 동생 승호에게도 감사의 마음을 전합니다. 자주 찾아 뵙지는 못하지만 좋은 일이 생기면 항상 진심으로 축하해주신, 외할아버지 외할머니, 이모들, 삼촌 그리고 큰아버지 큰어머니께도 감사의 인사를 전하며 감사의 글을 마칩니다.